The Effect of Alkali-Silica Reaction on Aggregate Interlock in Reinforced Concrete and the Use of Digital Image Correlation to Monitor the Long-Term Behaviour of Concrete Structures

By

FRANCIS THÉRIAULT

Under the supervision of

Dr. Martin Noël

Co-supervisor

Dr. Leandro Sanchez

A thesis submitted to the University of Ottawa in partial fulfillment of the requirements for the degree of

Master of Applied Science in Civil Engineering

uOttawa

Faculté de génie
Faculty of Engineering

Department of Civil Engineering
University of Ottawa

May 2020

Acknowledgments

First, I would like to acknowledge the financial support of the Fonds de recherche du Québec - Nature et technologies, Mitacs, and the Faculty of Engineering of the University of Ottawa.

Then, I would like to thank my supervisor professor Martin Noël and professor Leandro Sanchez for welcoming me into their research group and for giving me this great project. Thanks to your lessons, I was able to acquire expertise on the structural behavior and durability of reinforced concrete structures. Thank you for making me discover a new passion as well. I am very grateful for all the support you have given me with this challenging and stimulating project, and with the writing of this manuscript. Thank you also for having created for me an opportunity to work on a research and development project with the team of Pierre-Luc Fecteau from GHD.

I would then like to thank professors Daniel Cardoso and Martin Noël for giving me the opportunity to carry out a complementary research project at the Pontifical Catholic University of Rio de Janeiro, in Brazil. This experience properly introduced me to the laboratory work associated with the testing of reinforced concrete specimens and gave me the necessary tools to carry out my shear push-off tests in Ottawa afterwards. My stay in Rio de Janeiro also allowed me to meet extraordinary people. I want to thank Felipe Tourinho who warmly welcomed me in his home for the duration of my stay, but also the whole research team of Professor Cardoso, including Thomás Lima and Danielle Duque, and the laboratory technicians who helped me.

To carry out my laboratory work in Ottawa, I could count on the help of Professor Muslim Majeed and Gamal Elnabelsya, but also on a surprisingly large number of students: Santiago Cordova, Joao Silva, Shanmuga Priya, Noah Jalbert, Jordy Alex Ntiringaniza, Kim Alain Kazenga, Batool Khozema, Nicholas Chan, Cassandra Trottier, Lamiaa Ismail, Diego De Souza, Mayra Tagliaferri de Grazia, and Mohamed Youssef Benmchich. Thank you all sincerely.

I also need to thank Luc Cloutier for trusting me with three teaching assistantship contracts during my master's studies. I loved these experiences.

Last but not least, I would like to thank my friends, my familly, especially my parents (Richard Thériault and Sylvie Leroux), and Camille Larose for always being there for me.

Abstract

Alkali-silica reaction (ASR) is a chemical reaction between the alkali hydroxides from the concrete pore solution and some siliceous mineral phases present in the aggregates used to make concrete. ASR generates a secondary product, the so-called ASR-gel, that swells upon moisture uptake, leading to induced expansion, microcracking, and reduction in the mechanical properties of the affected material. ASR is likely the most harmful damage mechanism affecting the serviceability and long-term performance of concrete infrastructure worldwide, yet its structural implications in concrete structures remain unclear. Even though shear resistance of reinforced concrete has been studied extensively by the research community due to the brittleness and danger associated with concrete shear failures, knowledge on the impact of ASR on reinforced concrete shear resistance is very limited. To fill this lack of knowledge, the effect of ASR on the aggregate interlock shear transfer mechanism in reinforced concrete was investigated. Lightly reinforced shear push-off specimens with low to moderate expansion levels were tested while recording crack kinematics. The experimental testing program allowed to decouple the deleterious effect of ASR microcracks within the reactive coarse aggregate particles and the beneficial effect of the so-called *chemical prestressing*. The aggregate interlock shear strength was significantly impacted, even in the case of a low expansion level for which the microcracks have theoretically not reached the cement paste yet, and surprisingly, it was not affected by prestressing. The experimental results were compared to predictions from three existing simplified aggregate interlock models which tended to overestimate the measured shear strengths.

Digital image correlation (DIC) is an innovative optical measurement technique that could provide several advantages for long-term structural inspections such as remote full-field measurements. A method was proposed to correct 2D-DIC measurement errors associated with the inevitable camera movement between photographs taken during different inspections. Using the aforementioned push-off specimens, it was applied to the monitoring of shear crack kinematics and ASR expansion. The method significantly improved measurements produced from images acquired with a non-expensive hand-positioned camera equipped with a lens of normal focal length and a free to use DIC software. For ASR expansion monitoring, the measurement errors could not be reduced below a selected tolerance limit of ±0.02 mm (±0.01% strain), although increasing the measurement gauge length could potentially provide satisfactory results. On the other hand, over 99 and 96% of the measurements were within the selected tolerance limit of ±0.1 mm for the corrected crack width and slip measurements, respectively. These promising results validate the potential of the proposed method to overcome errors associated with camera movement between photographs and as such, it represents a step towards the use of the DIC technique for periodic structural inspections.

Keywords: reinforced concrete shear behaviour; aggregate interlock; alkali-silica reaction; digital image correlation; structural health monitoring

Résumé

La réaction alcali-silice (RAS) est une réaction chimique interne dans le béton qui, à long terme, conduit à son gonflement et à sa microfissuration, et ainsi, à une diminution des propriétés mécaniques du matériau. Il s'agit d'un mécanisme de dégradation bien connu affectant la durabilité des infrastructures en béton dans le monde entier, mais son impact sur la résistance des structures en béton demeure difficile à quantifier. Même si la résistance en cisaillement du béton armé a été largement étudiée par le passé en raison de la soudaineté et du danger associés aux ruptures de cisaillement du béton, l'impact de la RAS sur la résistance au cisaillement du béton armé demeure très peu connu. Pour combler ce manque de connaissances, l'effet de la RAS sur un important mécanisme de transfert de cisaillement dans le béton armé, dénommé *aggregate interlock,* a été étudié. Des essais de cisaillement simples (Z-Type push-off test) ont été conduits avec des spécimens de béton légèrement armés, pour des niveaux de gonflement faibles à modérés, alors que des mesures du glissement et de la largeur de la fissure de cisaillement ont été prises. Le programme d'essais expérimentaux a permis de découpler deux effets simultanés de la RAS: la diminution de la rugosité de la craque due aux microfissures dans les granulats grossiers et l'augmentation de la compression normale au plan de cisaillement due à la précontrainte chimique. Le transfert des contraintes de cisaillement par *aggregate interlock* a diminué beaucoup plus qu'anticipé, en particulier dans le cas d'une expansion faible, considérant que les microfissures dans les granulats sont théoriquement encore très petites. Il a aussi été surprenant de constater que la précontrainte n'a pas eu d'impact sur la résistance en cisaillement des spécimens. Les contraintes de cisaillement obtenues étaient plus petites que les valeurs prédites par trois modèles simplifiés provenant de la littérature.

La corrélation d'images numériques est une technique de mesure optique innovante qui pourrait offrir plusieurs avantages pour l'inspection à long terme des structures tels que des mesures à distance et la possibilité d'accéder à des champs de valeurs sur l'ensemble d'une surface observée. Une méthode a été proposée pour corriger les erreurs de mesure bidimensionnelle associées au mouvement inévitable de la caméra entre des photos prises lors de différentes inspections. À l'aide des spécimens de béton armés mentionnés précédemment, la méthode il a été appliquée pour corriger des mesures de fissures de cisaillement et celles de gonflement due à la RAS. La méthode a considérablement amélioré les mesures produites à partir d'images acquises avec une caméra positionnée à la main, peu coûteuse et équipée d'un objectif de distance focale normale ainsi qu'un logiciel d’analyse gratuit. Pour la mesure du gonflement due à la RAS, les erreurs de mesure d’expansion n’ont pas été réduites en dessous d'une limite de tolérance de ± 0.01%, bien qu’une augmentation de la longueur de jauge aurait potentiellement pu fournir des résultats satisfaisants. D'un autre côté, pour les mesures de largeur et de glissement de fissure de cisaillement, plus de 99 et 96% des mesures corrigées ont respecté la limite de tolérance sélectionnée de ± 0.1 mm, respectivement. Ces résultats prometteurs valident le potentiel de la méthode proposée pour corriger les erreurs associées au mouvement de la caméra entre différentes photos d’inspection et représentent un pas vers l'incorporation de la technique de corrélation d’images numériques dans les inspections structurales périodiques.

Mots-clés: comportement du béton armé en cisaillement; *aggregate interlock*; réaction alcali-silice; corrélation d'images numériques; inspections structurales

Table of Contents

List of Figures

List of tables

1. INTRODUCTION

1.1 Background

Reinforced concrete structures such as bridges, tunnels, industrial facilities, buildings, and foundations represent much of the world's infrastructure. Most of these structures are designed to last several decades, depending on their nature, their environment, and the needs of the population. However, concrete degradation over time reduces their durability, shortens their service life, or can even lead to premature structural failures.

1.1.1 Alkali-silica reaction (ASR) degradation mechanism

ASR is a physicochemical process that takes place between the alkali hydroxides from the concrete pore solution (Na^+, K^+, and OH^-) and some siliceous mineral phases present in the coarse and fine aggregates used to make concrete. ASR generates a "secondary" product (i.e. ASR-gel), that swells upon moisture uptake, leading to important microcracking and overall deterioration (i.e. mechanical properties reductions) of the affected material. ASR has been reported to significantly reduce the service life of reinforced concrete structures worldwide (FHWA, 2013; Sanchez et al., 2016; Thomas et al., 2011).

Several parameters may increase the rate of ASR expansion in concrete, such as the reactivity of aggregates used in the mix (i.e. amount and type of siliceous phases), the alkali loading of the concrete, the presence of internal moisture, and temperature. By reducing those, it is possible to mitigate the chemical reaction rate. This can be achieved mainly during the mix-design of concrete. Nowadays, CSA codes A23.1-14A and A23.2-25A require that the potential alkali reactivity of aggregates and concrete mixtures be tested prior to using them in the field. However, the structures that were designed before the appearance of this requirement are potentially at risk. For example, Robert-Bourassa Charest overpass, located in Quebec City, Canada, was a highway viaduct structure built in 1966 with the use of an alkali-silica reactive limestone coarse aggregate. This bridge had to be demolished in 2010/2011 due to advanced deterioration primarily caused by ASR (Figure 1.1, Sanchez et al., 2015).

Figure 1.1: ASR map cracking on the reinforced concrete Y-shaped piers and massive concrete foundations of the Robert-Bourassa/Charest viaduct, Quebec, Canada (Sanchez et al., 2015)

The chemical reaction and the physical process associated with ASR have been studied extensively, but the implications on the serviceability and/or ultimate limit states of affected structures remain unclear. This may be attributed to the complexity and variability of influencing parameters in existing structures such as confinement and loading conditions. Also, most of the experiments on ASR were performed at the material's scale. Hence, there is a need for experiments on larger damaged reinforced concrete specimens in combination with microscopic analyses and tests of affected concrete cores to enable proper assessments of aging infrastructure (Noël et al., 2017).

The shear resistance of ASR-affected concrete members, in particular, is not well understood. The formation of cracks within coarse aggregates can potentially reduce the shear stresses resisted by aggregate interlock across a cracked concrete surface. On the other hand, the compressive stresses induced by the so-called *chemical prestressing* effect have a tendency to increase shear strength. Thus, the net effect of ASR damage on the total shear resistance of concrete members with different geometries, reinforcement, and boundary conditions is not clear and requires further study.

1.1.2 Shear resistance of reinforced concrete

In the last century, shear behaviour of reinforced and prestressed concrete has been of high interest for the research community. It is a complex topic since several different shear transfer mechanisms contribute to the overall shear response of reinforced concrete structures. Recently, some researchers have attempted to quantify the contributions of each shear transfer mechanism to shear strength of reinforced concrete (Campana et al., 2013; Cavagnis et al., 2018b; Huber et al., 2016; Zarate Garnica, 2018). While there remains a lack of consensus regarding the interaction and relative importance of each individual mechanism, it is generally agreed that aggregate interlock plays an important role in the shear resistance of cracked concrete.

Significant differences among the shear equations used in various design codes around the world have motivated researchers to conduct experimental testing with the aim of elucidating the true shear response of reinforced concrete. The importance of developing a deeper understanding of shear is due to the potential sudden and brittle shear failures that concrete members experience once the applied loads exceed their shear capacity. A famous example of such failure is the tragic collapse of De la Concorde Overpass located in Laval, Quebec, in 2006, which occurred without any clear warning such as a large deflection (Figure 1.2). Important shear cracks had been noticed on the concrete slabs supporting the central portion of the bridge, but their initiation and growth had not been measured over time, which combined with an estimation of internal stresses, could have saved people's lives.

Figure 1.2: Collapsed De la Concorde Overpass in 2006 (Journal de Montréal, 2016)

Design code shear equations that were used for structures built before the 21st century have since changed, as our understanding of the shear strength of reinforced concrete has improved. For example, a decrease in the shear capacity of deeper reinforced concrete structural elements has been experienced in laboratory tests (Ghannoum, 1998; Sherwood, 2008), and thus, the so-called *size effect* is now considered in shear design provisions of ACI 318-19 (Kuchma et al., 2019) and Canadian standards (CSA A23.3-19). Structures that were designed before recent discoveries on the shear behaviour of reinforced concrete are potentially at risk. However, mechanistic shear resistance models that consider crack kinematics (e.g. Calvi, 2014) could be combined with in situ measurements of crack width, slip, and orientation to estimate the reserve shear capacity of overloaded reinforced concrete elements and determine if they are still fit for purpose.

1.1.3 Long-term structural health monitoring of concrete infrastructure

In North America, the concrete structures constructed during the last century's infrastructure booms are deteriorating with age and approaching the end of their service lives; hence, many important assets require field monitoring. The inspections of aging concrete structures have commonly been performed visually on a routine basis, often without incorporating non-destructive evaluation techniques to produce quantitative measurements of the evolution of defects. Visual inspections of highway bridges were found to be inaccurate and unreliable, showing too much variability, especially when deterioration is assessed by different inspectors (Phares et al., 2004). Of course, there are added costs associated with the use of measuring instruments, but also, there are several practical challenges, limitations, and risks associated. For example, in Canada, permanently attaching sensors (e.g., strain gauges, extensometers, displacement transducers, etc.) to a structure exposes them to harsh environments and weather conditions, leading to long-term stability issues. Nevertheless, the tragic event of De la Concorde Overpass in Laval (QC) highlights the need to avoid the sole use of qualitative and subjective assessments for reinforced concrete structures. As mentioned earlier, with quantitative measurements of the critical diagonal shear crack on the thick cantilever slab, it would have been possible to estimate the residual shear resistance with more accuracy and deem the structure unsafe. Currently, in Canada, bridge inspections are done by inspectors every one or two years (Transport Canada, 2013). They mainly inspect the defects visually or rely on basic measuring instruments. For example, to monitor crack width changes, they may use a ruler, a plastic tell-tale, or a displacement transducer, but those instruments do not allow the measurement of a crack over its entire length (Figure 1.3).

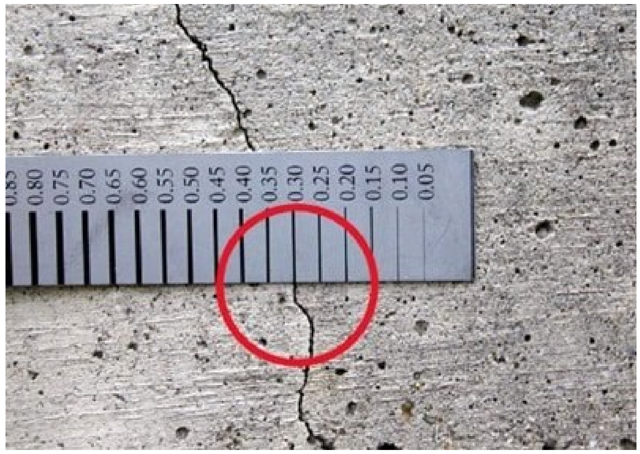

Figure 1.3: Crack width measurement with a steel ruler (Hamakareem, 2019)

After an initial condition survey, an instrument such as the “DEMEC-type” strain gauge may be used to measure the length change between embedded reference pins (Figure 1.44). Unfortunately, such methods can only provide measurements in limited locations and directions, depending on where pins have been installed, and require a priori knowledge of critical crack locations. Moreover, some locations such as the underside of a bridge deck may be hard to access by inspectors.

Figure 1.4: Expansion measurements using a DEMEC strain gauge (Thomas et al., 2013)

Digital image correlation (DIC), an optical method to measure displacements and strains of materials, is an emerging technology in the field of structural health monitoring (SHM) that could improve the quality and reliability of inspections while lowering their costs with time savings. The DIC technique consists of taking digital photos (or a video) of an area of interest on a given element before and after (or throughout) its deformation, and subsequently post-process the photos using computer software to track changes between the images. With the simple use of a digital camera, 2D measurements can be obtained, but if two digital cameras are used, 3D movement can be measured (Pan et al. 2009). The distributed full-field deformation measurements enable detailed investigations of strains and displacements in desired locations and directions on the inspected surface. This represents the main advantage of the DIC technique over measurement devices that can only produce unidirectional and discrete measurements. Indeed, there is no need for priori knowledge of the exact location where a defect such as a concrete crack will appear, as long as it takes place within the zone covered by the photos. For example, the onset of concrete cracking can be detected, and the crack growth can subsequently be followed over time. Also, large structure surfaces can be inspected a lot more conveniently than with technologies producing a limited number of discrete measurements. The DIC technique is also very practical and easily implemented, as it allows for measurements to be taken rapidly and remotely from the inspected element, without any contact, wiring, or road traffic interruptions (Atkins, 2017; Gamache & Santini-Bell, 2009). For long-term structural monitoring, traditional sensors (e.g., strain gauges, linear displacement transducers, etc.) need to stay connected to the structure, so they are exposed to outdoor harsh environments. The DIC technique, on the other hand, presents no such risk. Also, challenges related to sensor system installation (e.g., on the underside of a bridge over water) are not a concern either. The digital images can be taken with a low-cost camera, easily carried to the field by inspectors, and a free or low-cost DIC software application may be used for post-processing the images. Hence, the data treatment is relatively easy. The technology is also versatile. For example, it has been proven to provide accurate measurements when drones are used to photograph hardly accessible locations on a structure (Reagan et al., 2018).

One challenge associated with the use of DIC to supplement visual inspections is that the camera should be stationary to track deformations between subsequent photographs. It would be difficult and highly impractical for an inspector to reproduce the exact positioning of the camera at each visit. Ideally, a hand-held camera could be used by the inspector without excessive care in the camera positioning. A simple solution is needed that can reduce the time required by the inspector while simultaneously reducing errors and providing reliable quantitative measurements.

1.2 Research motivation

1.2.1 The unclear impact of ASR on aggregate interlock

In Canada, concrete structures are exposed to aggressive environments and thus, many of them suffer from durability problems and fail to fulfill their design service life requirements (Cusson & Isgor, 2004). The shear failure of the De la Concorde Overpass 36 years after its construction was not only due to unsatisfactory design, but also to a decrease in load capacity over time caused by degradation mechanisms, mainly freezing and thawing (Mitchell et al., 2011). ASR is another long-term damage mechanism affecting the durability of aging concrete infrastructure, and its effect on the shear behaviour of reinforced concrete is an important yet unclarified topic (Gowripalan & Cao, 2018; Noël et al., 2017). While the ASR microcracks in the aggregates may reduce the aggregate interlock stress transfer across a shear crack by reducing its roughness, on the other hand, if the concrete expansion is restrained perpendicular to a shear crack (e.g. due to internal reinforcement), the resulting compressive stress induced on the shear plane enhances the friction. The simultaneous occurrence of those two influencing phenomena makes it challenging to evaluate how aggregate interlock is affected by different ASR expansion levels (Noël et al., 2017). Therefore, this research aims to decouple the contributions of the chemical prestressing (i.e. the increase in normal stresses across the cracked surface) from that of the internal damage caused by ASR.

1.2.2 DIC measurement errors caused by camera movement between structural inspections

The benefits of incorporating the DIC technique in current inspection practices are very appealing. The DIC technology has been relied upon extensively in laboratory-controlled environments, where the accuracy and precision of the measurements are high (Acciaioli et al., 2018). However, for SHM, DIC measurement errors are increased, and the sources of error may vary, especially in the case of certain long-term monitoring applications. Nevertheless, upon ensuring acceptable measurement accuracy, its transfer from laboratory environments towards the industry would be advantageous. For example, it would be possible to follow the long-term evolution of degradation and overloading signs over large structure surfaces, combining photos to form a grid of images representing a “map” of the structure. Thus, researchers have been developing methods for limiting the possible measurement errors (Abolhasannejad et al., 2018; Hoult et al., 2016; Pan et al., 2016).

For certain applications, the DIC technique has yet to be tried or improved. For example, when following the evolution of a defect, the removal and repositioning of the camera between inspections leads to unavoidable measurement errors. Even if precautions were taken by an inspection team to position a camera in the same location and with the same orientation before each photograph, which would be time-consuming, it would not be reasonable to neglect measurement errors related to camera positioning. A second aim of this research is to reduce the errors that result from camera movements as a potential first step towards developing an improved quantitative visual inspection protocol.

1.3 Study scope and objectives

This thesis project has two components. First, the impact of ASR on the aggregate interlock, an important shear transfer mechanism in reinforced concrete, was investigated. Shear push-off tests were conducted with ASR-damaged and undamaged pre-cracked specimens. The effect of ASR on the aggregate interlock was evaluated for different expansion levels. The influence of ASR-induced cracks within coarse aggregates and reinforcement confinement on the shear transfer mechanism are normally simultaneous, but the test program attempted to decouple the two phenomena for low and moderate levels of expansion, i.e., 0.00, 0.04, 0.07 and 0.12%. The obtained shear stress-slip relationships were compared to those predicted by three existing aggregate interlock models with the aim of proposing modifications to account for low to moderate ASR expansion levels.

In the second part of the thesis, an innovative approach was proposed to correct 2D-DIC measurement errors due to camera movement between captures. It involves the use of the apparent displacements a four reference points in the plane of the inspected surface and the field of view of the camera, and simple geometric equations to correct the apparent measurements. The correction method can be used for measuring absolute or relative displacements. In the case of relative displacements (e.g. strains and crack widths), in-plane translations of the template between photographs are not critical, and it is anticipated that the same method could be used with any reference points within the image frame and in the plane of the inspected surface as long as their relative distances are large enough and known. Using the aforementioned shear push-off specimens and a hand-held digital camera of standard quality equipped with a regular lens, the method was applied for correcting ASR expansion and shear crack measurements, i.e., relative displacements. The results were compared with the measurements from a conventional method (i.e. DEMEC points) and a second DIC camera with a fixed location and long focal length, which allowed for the achievable accuracy using the proposed approach to be determined.

1.4 Thesis outline

The thesis consists of 5 chapters. Chapter 1 introduced the research needs, objectives and scope of the work. Chapter 2 presents background information on the key components of the project, namely: the aggregate interlock shear mechanism in reinforced concrete, the impact of ASR on the shear behaviour of reinforced concrete, and the use of the 2D-DIC measurement technique for the long-term monitoring of concrete structures. Chapter 3 presents the methodology, results, and analysis associated with the shear push-off tests which were conducted to evaluate the impact of ASR on aggregate interlock. Chapter 4 presents the proposed method to correct DIC measurement errors due to camera movement between inspection captures, the experiments conducted to validate it for the correction of ASR expansion and shear crack measurements, and the achieved accuracy. Chapter 5 presents the conclusions of this research project and the author's recommendations associated with it.

2. LITERATURE REVIEW

2.1 Aggregate interlock shear transfer mechanism

2.1.1 Mechanisms of shear transfer in a reinforced concrete member

When a reinforced concrete member is subjected to shear forces, several different load carrying mechanisms act together to resist those forces (ASCE-ACI Committee 445 on Shear and Torsion, 1998; Fédération Internationale du Béton (fib), 2010). For example, in a slender reinforced concrete beam with a diagonal shear crack, as illustrated in Figure 2.1: the transverse shear reinforcement is subjected to tensile stresses (V_{sw}); the longitudinal bars can transfer forces perpendicular to their length by dowel action (V_{da}); some tensile stresses are transferred across the critical crack close to its tip (V_{cr}), in the fracture process zone (FPZ); the uncracked concrete compression zone carries shear (V_{cz}); and the aggregates protruding from the two faces of the crack are interlocking with the cement matrix of the opposite surface, preventing crack slippage (V_{ag}). The term *aggregate interlock* is often used to describe the latter shear transfer mechanism, which is the focus of this section.

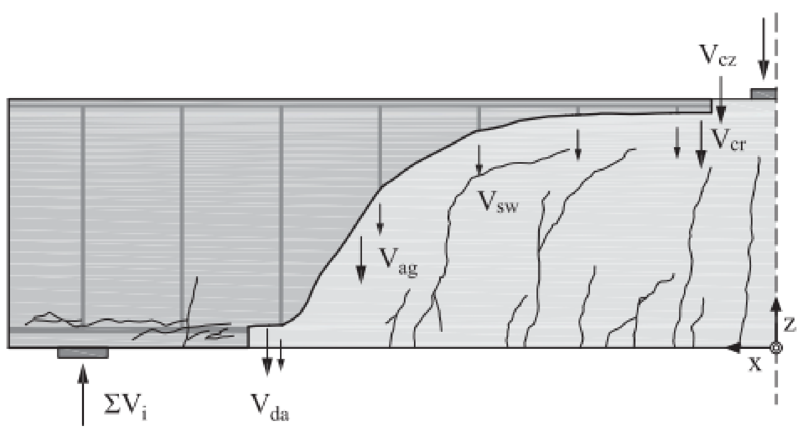

Figure 2.1: Vertical force component of the acting shear transfer mechanisms in a reinforced concrete beam (Huber et al., 2016)

Even though extensive experimental and theoretical work has been done to understand the shear behaviour of reinforced concrete members, there is no consensus on the relative importance and interaction of the acting shear transfer mechanisms, nor on the main influencing parameters. It should be noted, however, that the number of influencing parameters is large (e.g. member depth, cross-section type, concrete type, quantity of reinforcement, crack shape, etc.). Thus, researchers such as Campana et al. (2013), Huber et al. (2016), and Zarate Garnica (2018) have investigated the critical diagonal crack kinematics in beams tested in shear from its initiation up to failure of the specimen. They measured crack opening, sliding, and orientation angle, and combined those measurements with constitutive laws from the literature to estimate the relative contributions of the different shear transfer mechanisms at various stages of crack propagation. It was demonstrated that aggregate interlock, the shear transfer mechanism of interest in the present research work, normally has an important contribution to reinforced concrete shear resistance. Several other experimental research studies such as those presented in Walraven & Reinhardt (1981) and Sherwood et al. (2007) have led to the same conclusion. Moreover, in the critical shear crack theory (Muttoni & Fernández Ruiz, 2008), the modified compression field theory (Vecchio & Collins, 1986) and its simplified analysis method (Bentz et al., 2006), the shear failure of a reinforced concrete member is defined by a critical crack width, suggesting that the aggregate interlock contributes significantly to shear capacity.

2.1.2 Shear push-off tests

Aggregate interlock behaviour is typically tested using shear push-off specimens (Fenwick & Paulay, 1968; Taylor, 1970; Wight, 2016). The size and geometry of those specimens can vary. Figure 2.2 illustrates the configurations adopted by Walraven & Reinhardt (1981) and many others, i.e., *Z-type* push-off specimens. These are characterised by a vertical *shear plane* at their center, crossing their entire depth, and usually reinforced transversely.

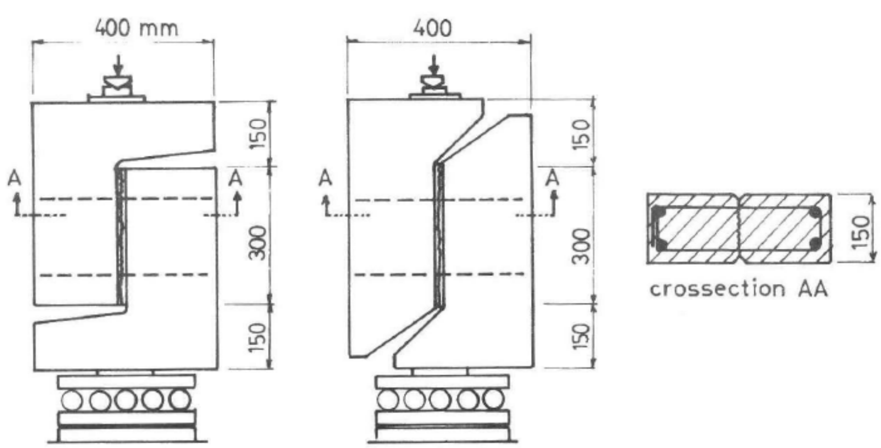

Figure 2.2: Shear push-off specimen geometries (Walraven, 1980)

The geometry of the push-off specimens and loading arrangement are intended to avoid bending stresses and obtain a pure shear failure. Thus, they are useful for analyzing the aggregate interlock phenomenon, develop models, or validate existing ones. To ensure that the crack doesn't propagate too far out of the intended shear plane, linear vertical notches are usually made on the front and back sides of the shear plane during casting. The vertical load is usually applied continuously, at a certain shear displacement rate (Hofbeck et al., 1969; Soetens & Matthys, 2017; Walraven & Reinhardt, 1981), but the aggregate interlock has also been studied under repeated loads (Walraven & Reinhardt, 1981).

Walraven and Reinhardt (1981) reported experimental values of shear stress (τ), normal stress (σ) and crack width (w) for different crack slip (Δ) increments (Figure 2.3), and modeled equations relating those variables (subsection 2.1.5.1). They assumed that the shear and normal stresses were constant over the shear plane area.

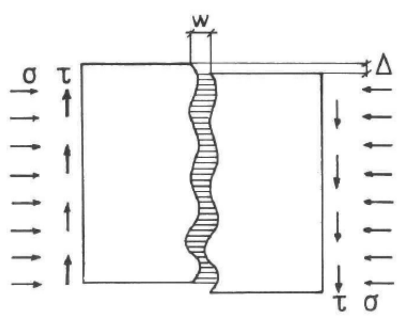

Figure 2.3: Stresses and displacements in a crack (Walraven, 1980)

In order to measure the tensile strain in the bars crossing the shear plane and obtain the normal stress (σ), the authors included a series of specimens with external reinforcement (Figure 2.4). For embedded bars, the authors estimated the force in the reinforcing steel bars based on bond characteristics.

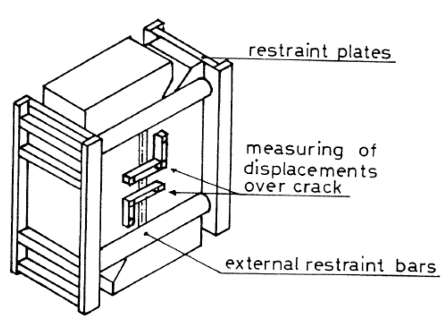

Figure 2.4: Arrangement of external reinforcement (Walraven & Reinhardt, 1981)

2.1.2.1 Pre-cracked push-off specimens

Before testing push-off specimens, it is common to initiate a vertical crack along the shear plane since aggregate interlock is only engaged after a crack has formed. In order to do so, the specimen is typically positioned horizontally on one of its larger faces, and a line load is applied along the two notches to split the concrete along the shear plane (Echegaray-Oviedo & Navarro-Gregori, 2012). The opening of the crack may be controlled through application of transverse compression forces. For instance, Walraven and Reinhardt (1981) tested push-offs with initial crack widths of 0.1, 0.2 and 0.3 mm. They discovered that an increase in the initial crack width enhances the shear displacement for a given shear stress and the crack opening for a given normal stress. Some researchers maintained a constant crack width throughout the loading test (Paulay & Loeber, 1974; Reinhardt & Walraven, 1982), but most previous tests were conducted without doing so (e.g. Hofbeck et al., 1969; Mattock & Hawkins, 1972; Walraven & Reinhardt, 1981).

Interesting comparisons between the behaviour of pre-cracked and uncracked specimens were made by Hofbeck et al. (1969), Mattock & Hawkins (1972) and Hsu et al. (1987). In the case of uncracked push-off specimens, parallel inclined tension cracks form across the shear plane, delimiting compression struts (Figure 2.5). As the load increases, the ends of the compression struts initially rotate, putting the stirrups under tension, similar to a truss-like action (Hsu et al., 1987). Then, crushing of the compression struts cracks the shear plane and a relative slippage of the interface occurs, putting the bars under combined shearing and stretching. In pre-cracked specimens, crack slippage occurs without formation of compression struts and diagonal tension cracks. Thus, the initial *cohesion-like* shear motion resistance is highly lower, reducing the required load to initiate crack slippage, and the required shear to cause a certain crack slip (Wight, 2016).

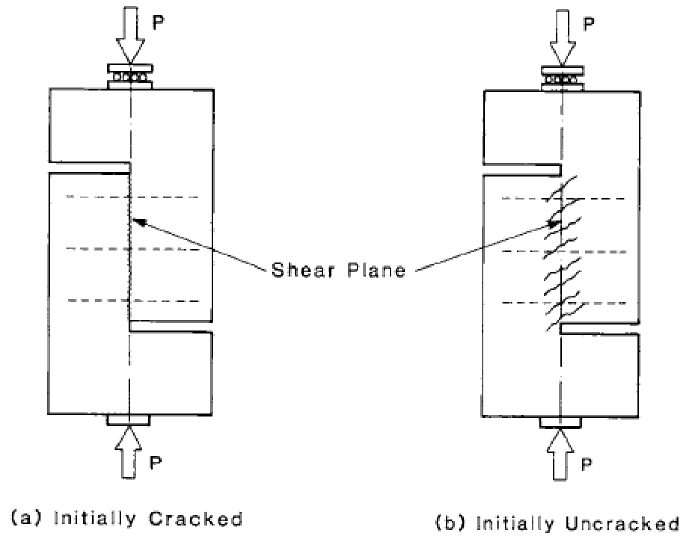

Figure 2.5: Cracks for initially cracked and uncracked push-offs (Hsu et al., 1987)

This behaviour increases the shear strength of uncracked push-offs compared to pre-cracked specimens. Interestingly, according to the results of Hofbeck et al., (1969), this difference is constant for varying reinforcement densities up to a certain value, after which the ultimate shear strength is merely affected by pre-cracking, suggesting the peak load is reached after cracking (Figure 2.6). In both pre-cracked and uncracked specimens, the interface is rough and thus, the crack needs to dilate in order to slip, generating tensile stress in the reinforcement and compressive stress on the two cracked concrete faces.

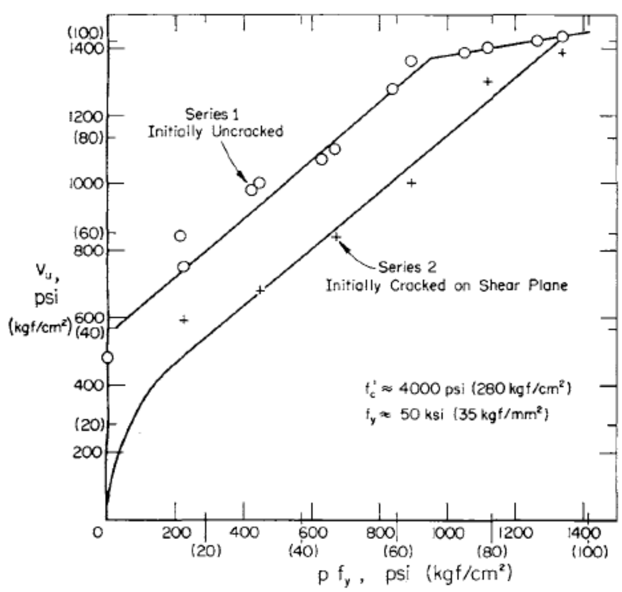

Figure 2.6: Variation of ultimate shear strength with pfy for pre-cracked and uncracked specimens (Hofbeck et al., 1969)

2.1.3 Concrete mix parameters affecting aggregate interlock

Past push-off experiments such as those of Walraven & Reinhardt (1981) compared the aggregate interlock behaviour of different concrete mixes. It was demonstrated that an increase in compressive strength influences the aggregate interlock in two ways: it increases the interlock by reducing the deformability of the cement paste, but on the other hand, it reduces the roughness of shear cracks, which has an opposite effect. Crack roughness contributes to aggregate interlock because it enhances the amount of contact areas perpendicular to shear displacement and it forces crack dilation during slippage. With the presence of restraint such as transverse reinforcement, crack opening induces compression on the interface. Crack roughness is reduced by an increase in strength since the cement paste bonds better to the aggregates and thus, the shear crack goes through a greater number of aggregate particles (Ali & White, 1999; Walraven & Reinhardt, 1981). Indeed, cracks in concrete propagate following the lowest fracture energy path (Lee & Lopez, 2014), leading them towards weaker zones, which is why they normally remain in the cement paste and go around the aggregate particles, in the interfacial transition zone (ITZ) (Scrivener et al., 2004). However, if the tensile strength ratio between the aggregates and ITZ is not high enough, the cracks split more aggregate particles and are then smoother (Figure 2.7). This has been observed in high strength concrete mixtures or when lightweight or recycled aggregates were used (Walraven & Reinhardt, 1981; Xiao et al., 2012).

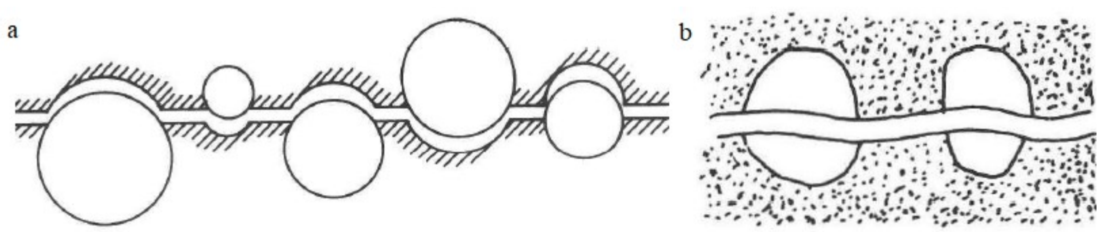

Figure 2.7: Generally observed crack path in normal strength concrete (a) and lightweight or high-strength concretes (b) (Walraven, 1980)

It can be added that if aggregates are not split by a crack, their proportion in the mix and properties such as shape, texture, stiffness, and PSD will affect the crack roughness. It has been demonstrated that the minor roughness of a crack (i.e., that from the sand particles) has no significant impact on shear friction (Walraven & Reinhardt, 1981). On the other hand, larger aggregates moderately improve aggregate interlock by imposing a larger crack dilation to permit relative slippage (Deng et al., 2017; Gambarova & Karakoc, 1983; Li et al., 1989; Sherwood, 2008).

Finally, it is worth mentioning that even though crack propagation in concrete is inherently random because of the heterogeneity of the material, Walraven & Reinhardt (1981) obtained a low variability in the results of a series of duplicate push-off specimens, demonstrating that the accidental overall structure of the crack plane had no significant impact on the shear behaviour compared to concrete mix variables. Moreover, in their theoretical aggregate interlock model, the authors considered a flat crack plane, assuming the overall crack undulations to be negligible compared to those from aggregate protrusions (Figure 2.7a).

2.1.4 The contribution of the reinforcement to push-off shear strength

Bars crossing the shear plane of a push-off specimen play a dual role since their elongation across the crack provides compression forces on the interface and the crack slippage induces bending and shear forces in the reinforcement (Walraven & Reinhardt, 1981). Since the present research project focuses on aggregate interlock, an understanding of the influence of reinforcement on the shear behaviour of push-off specimens is necessary.

2.1.4.1 Aggregate interlock enhancement due to normal stresses

As mentioned in the previous subsection, aggregate interlock requires concrete cracks to dilate for the two faces to slip relative to each other. If there is reinforcement crossing the shear crack, it will resist the opening of the crack and generate a normal force according to its stiffness. The tensile forces in the bars are equilibrated by the pressure generated across the crack. Similar to the friction experienced between any solid material surfaces, with an increase in the normal compressive stress, the aggregate interlock shear friction increases. Thus, an increase in the shear plane reinforcement ratio increases the ultimate shear resistance (Figure 2.6) and the shear stress for a given crack slip. It can be noted that the size of the bars and the spacing between them have a negligible effect on the shear behaviour of push-off specimens (Hofbeck et al., 1969; Walraven & Reinhardt, 1981).

2.1.4.2 Dowel action

Additionally, embedded stirrups also prevent slippage of the crack by dowel action (Figure 2.8), one of the reinforced concrete shear transfer mechanisms mentioned in subsection 2.1.1 (Ali & White, 1999; Huber et al., 2016; Walraven & Reinhardt, 1981). Dowel action from the stirrups can have a significant contribution to shear resistance of cracked push-off specimens. With uncracked push-off specimens, Hofbeck et al. (1969) didn't experience an impact from dowel action on ultimate shear strength, and they attributed that to an absence of slippage prior to the peak load.

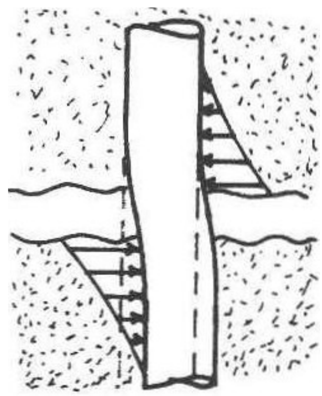

Figure 2.8: Dowel action from a bar crossing a shear crack (Walraven, 1980)

In order to eliminate dowel action, and study the aggregate interlock behaviour on its own, Hofbeck et al. (1969) and Walraven & Reinhardt (1981) secured soft sleeves around the legs of the stirrups where they cross the shear plane, to interrupt their contact with the concrete. The presence of those sleeves kept the stirrups from undergoing the usual shearing action at the crack when there is slippage. The rubber sleeves used by Hofbeck et al. (1969) reportedly eliminated any dowel action between the stirrup legs and the surrounding concrete for slip values of less than about 3 mm. The sleeves of Walraven & Reinhardt (1981) consisted of layers of tape, 0.3 mm thick, at the crack location and over a length of 4 cm (i.e., 2 cm on each side of the crack). The authors obtained a similar behaviour to that of the specimens with external reinforcement, which were designed such that the dowel action in the bars was negligible. However, they noted that the removal of bond over the wrapped part of the internal bars slightly reduced the restraint stiffness normal to the crack plane, which had to be considered in the results' analysis. Similarly, Li et al., (1989) passed the reinforcing bars crossing the shear plane through sheaths of larger diameter.

2.1.4.3 Additional local effects from embedded deformed bars

During their push-off tests, Walraven & Reinhardt (1981) measured the crack opening path, i.e., crack opening vs. slippage. They noticed that this relationship was more sensitive to changes in restraint stiffness, concrete strength, and aggregate properties in the case of externally reinforced push-offs compared to internally reinforced specimens. The authors attributed this difference to a local reduction of the crack width around embedded deformed bars caused by their bond with the concrete. This local effect causes a high shear stiffness leading to stress concentrations and microcracking around the bars (Figure 2.99a). According to the authors, this effect is much less pronounced in the case of undeformed bars due to reduced bond stresses. If the stress concentration resulting from the reduction of the crack opening in the direct vicinity of the embedded bars is high enough, similar to the behaviour of uncracked push-off specimens discussed in subsection 2.1.2.1, compression struts delimited by diagonal cracks may form. This behaviour should be avoided to study the aggregate interlock mechanism on its own. The use of sleeves around deformed bars successfully prevented local reductions of crack width and the associated microcracking.

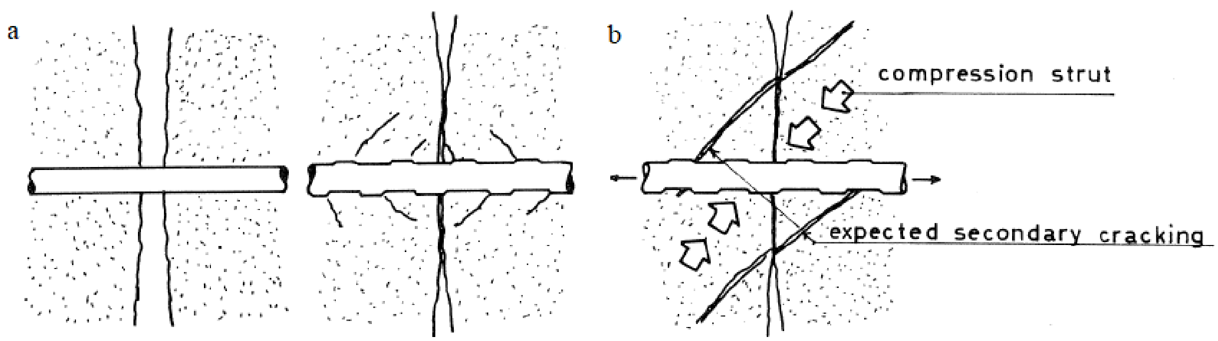

Figure 2.9: Cracks for smooth and deformed bars (a) and possible additional cracking from high stress concentration around deformed bars (b) (Walraven & Reinhardt, 1981)

2.1.5 Aggregate interlock models

Historically, attention was only given to relative shear displacements (slip), ignoring the effect of crack opening. Aggregate interlock models were mainly empirical, based on experimental testing and influenced by test setup specifics (e.g. Mattock & Hawkins (1972)). During the 1980's, shear crack dilatancy first started to be considered in analytical models. Researchers have been producing theoretical (Li et al., 1989; Walraven & Reinhardt, 1981) and semi-empirical models (Gambarova & Karakoc, 1983), providing a more physical representation of the shear transfer mechanism. More recently, Calvi et al. (2015) recently developed a rational crack behaviour model called the Pure Mechanics Crack Model (PMCM) to estimate the stress transfer across cracks. From the PMCM, the authors developed the "Assessment of Cracked Reinforced Concrete" (ACRC), an analytical model allowing its user to predict the residual capacity of a cracked reinforced concrete element by simply imputing crack width, slip and orientation measurements.

Researchers' efforts to improve cracked concrete shear transfer models show that they are important for the analysis of the residual shear strength of overloaded reinforced concrete members.

2.1.5.1 Walraven and Reinhardt (1981)

As mentioned earlier, Walraven & Reinhardt (1981) analyzed the phenomenon of aggregate interlock by means of pre-cracked monotonically loaded push-off tests. With information from the literature and their results, they derived a theoretical model describing the shear transfer mechanism. The model considers concrete as a material with 2 phases: the aggregate particles and the cement matrix, which includes aggregates smaller than 0.25 mm. The aggregates are assumed to be perfectly spherical and have a much higher strength and stiffness than the surrounding cement matrix. Thus, the crack goes through the cement matrix and around all aggregates, intersecting the aggregate at all depths possible with the same probability. The resulting micro-roughness is believed to contribute significantly more to aggregate interlock than the undulations of the crack plane (i.e., the macro-roughness), so the overall interface is assumed to be flat. The cement paste is a visco-elastic material, but its plastic deformations caused by pore-volume reduction are more important than its elastic response. Thus, the model assumes a rigid-plastic behaviour for the cement matrix. With applied shear loads, the cement paste deforms and contact areas form between the spherical aggregate particles protruding from one face and the cement matrix from the opposite face (Figure 2.10). The shear and normal stresses transferred through those local contact areas depend on the projected contact areas in the tangential (A_x) and normal directions (A_y), the deformability of the cement paste σ_{pu} and the friction coefficient μ, as follows:

$$\sigma = \sigma_{pu}(A_x - \mu A_y) \tag{2-1}$$

$$\tau = \sigma_{pu}(A_y + \mu A_x) \tag{2-2}$$

Based on a statistical analysis of the crack structure, the contact parameters A_x and A_y are calculated with the crack width w, the shear displacement Δ, the maximum particle size D_{max} (used in a Fuller curve distribution) and the volumetric proportion of the aggregates in the concrete.

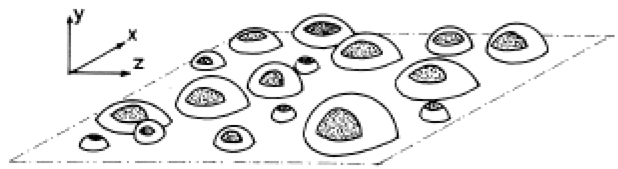

Figure 2.10: Contact areas during shear displacement (Walraven & Reinhardt, 1981)

The other parameters, σ_{pu} and μ, were adjusted so that the model would fit the experimental results. It was found that a coefficient of friction of μ = 0.4 and a matrix yield stress related to compressive strength as per the following equation would yield the best fitting:

$$\sigma_{pu} = 6.39f_{cc}^{0.56} \text{ (MPa)} \quad (2\text{-}3)$$

As mentioned in subsection 2.1.2, with externally reinforced push-off specimens, the authors were able to measure the strain in the reinforcement and deduce the normal stress across the crack. From their results, they plotted the following three relationships: the crack width w vs. the slip Δ; the average shear stress τ vs. the slip Δ; and the average normal stress σ vs. the crack width w. The relations were non-linear, but the authors deduced the following linear relations between shear stress, normal stress, crack slip and crack width:

$$\tau = -0.04f'_c + \{1.8w^{-0.80} + (0.292w^{-0.707} - 0.25) \cdot f'_c\}\Delta \qquad (\tau > 0) \quad (2\text{-}4)$$

$$\sigma = -0.06f'_c + \{1.35w^{-0.63} + (0.242w^{-0.552} - 0.19) \cdot f'_c\}\Delta \qquad (\sigma > 0) \quad (2\text{-}5)$$

Where τ and σ are in MPa, w and Δ are in mm, and f'_c is the cylinder compressive strength in MPa.

In the fib Model Code 2010 (Fédération Internationale du Béton (fib), 2013), the possible aggregate splitting discussed in subsection 2.1.3 is accounted for by multiplying a reduction factor C_f to equations 2-4 and 2-5. For concrete types in which cracking doesn't split the aggregates, such as low strength concretes, C_f is taken as 1.0. The minimum value for C_f is 0.35, corresponding to a very high proportion of aggregate particles split by cracking.

2.1.5.2 Gambarova and Karakoç (1983)

In this research, the theoretical results for a crack with constant width from Bazant & Gambarova (1980), which are based on a simplified micromechanics model, were compared with past test results obtained with constant normal stress. The authors found intersection points between shear stress-displacement curves at constant crack opening and those at constant confinement. For each intersection point, they plotted the four parameters of interest, τ, σ, Δ, and w, in the plane (σ, Δ), and developed the following relationship between normal stress and crack displacements for constant crack opening:

$$\sigma = -a_1 a_2 \frac{\Delta\tau}{(w^2\Delta^2)^q} \tag{2-6}$$

Where $a_1 a_2$ = 0.62 and q = 0.25.

The new formulation is in good agreement with the test results from Walraven & Reinhardt (1981). A new equation was also proposed for the shear stress. It better accounts for the effects of aggregate size and uses an improved formulation of the tangent shear modulus upon cracking. The micromechanics model shares two of the assumptions from the theoretical model developed by Walraven & Reinhardt (1981): the aggregate particles are assumed as perfect spheres and their size distribution matches a Fuller grading curve. The authors note that according to past test results at constant crack opening, the shear stress is closely dependant on the ratio r = Δ/w. Their micromechanics model was derived accordingly:

$$\tau = \tau_0 \left(1 - \sqrt{\frac{2w}{D_{max}}}\right) \frac{c_1 r + c_2 r^4}{1 + c_2 r^4} \tag{2-7}$$

With

$$c_1 = \frac{10}{f'_c}$$

$$c_2 = 2.44(1 - 16.33 f'_c)$$

Where D_{max} is the maximum aggregate size in mm and τ_0 represents the shear strength of the crack in the limit case of zero crack opening in MPa.

After producing the new equations for shear and confinement stresses, the authors subsequently checked them with test results. Upon using 0.25-0.30f'_c for τ_0, the values obtained with equation 2-7 showed good agreement with the experimental results from Paulay & Loeber (1974) and Walraven & Reinhardt (1981). On a side note, Soetens & Matthys (2017) compared the three aggregate interlock shear transfer models presented in this subsection with their test results, and they took τ_0 as $0.195f'_c$ because the compressive strength f'_c of the concrete they tested was high, varying from 57.8 to 72.1 MPa.

2.1.5.3 Li et al. (1989)

Li et al. (1989) conducted a series of experiments with pre-cracked reinforced concrete push-off specimens. In most of the tests the crack width was kept constant, but in order to develop a shear transfer model applicable to any kind of loading path, some tests were also conducted with different stress paths, including cyclic loading. Similar to the two models presented before, in the formulation of their physical model, the authors first proposed an approach to idealize the crack surface asperity. However, instead of simply representing aggregate interlock as the contact between perfectly spherical aggregates protruding from a face and the opposite surface, they further measured the crack surfaces of cracked concrete blocks using a digitizer, which allowed them to model the geometry of cracks. They proposed that the crack surface is divided into "contact units" of different inclinations and assumed that the directional distribution of the contact units is represented by a stochastic contact density function which is independent of the size of aggregates and the concrete compressive strength. This contact density function is central to the development of the physical model since the transferred shear and normal stresses are directly influenced by the inclination of the contact units (Figure 2.11).

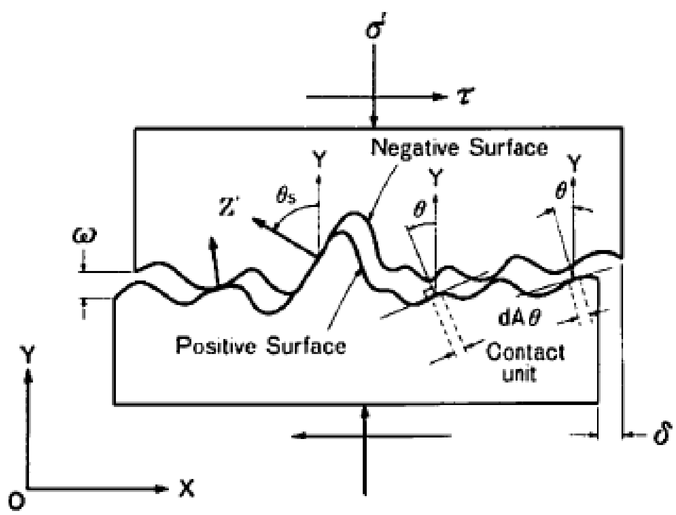

Figure 2.11: Stress transfer through local contacts with different orientations at the crack interface (Li et al., 1989)

As seen in Figure 2.11, the sliding crack surfaces first touch each other at locations where the contact areas have steep angles. Then, with further shear displacement, localized plastic deformation occurs in those contact areas and the flatter contact units come into contact as well. This is supported by the obtained τ-σ curves shown in Figure 2.12 because they show a reduction in the rate of shear stress compared to the rate of normal stress as the load is increased (i.e. the slope of the τ-σ curves reduces). Indeed, the steeper the orientation of the contact units, the more shear they transfer relative to the normal stress. Even though there is localized plastic deformation, the authors proposed that the initial orientation of the contact units remains constant during loading.

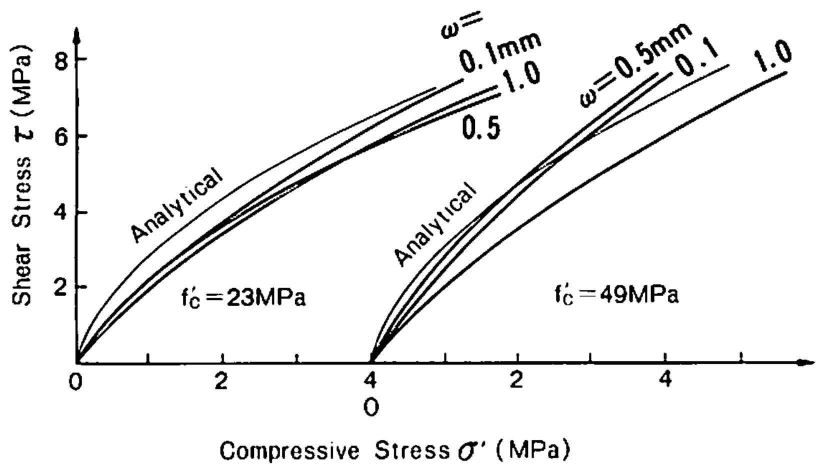

Figure 2.12: Relation between shear and normal compressive stresses (Li et al., 1989)

The physical model developed by Li & Maekawa (1989) agreed with the experimental results obtained by the authors, including for cyclic loading cases. For the case of monotonic loading, the authors also proposed a simplified path-independent stress transfer model. Similar to Walraven & Reinhardt (1981), a rigid-plastic deformation behaviour as shown in Figure 2.13 was assumed for the contact plane since the crack kinematics are usually much larger than the elastic deformational component during monotonic loading.

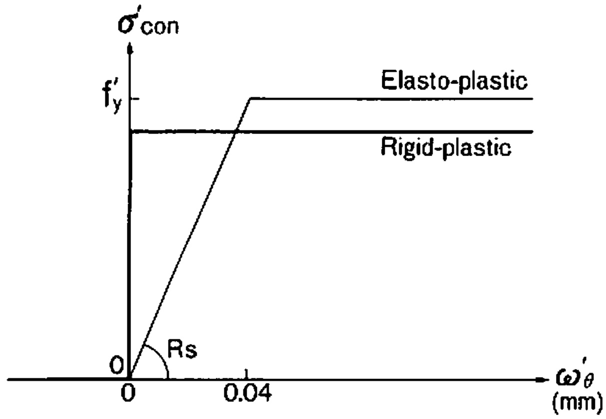

Figure 2.13: Simplified rigid-plastic model (Li et al., 1989)

The simplified equations for shear and normal stresses were calculated by analytical integration of the contact compressive force with respect to the angle of inclination of the contact units (Equations 2-8 and 2-9):

$$\tau = 3.83 f_c'^{1/3} \frac{r}{1+r^2} \tag{2-8}$$

$$\sigma = 3.83 f_c'^{1/3} \left[\frac{\pi}{2} - \cot^{-1} r - \frac{r}{1+r^2}\right] \tag{2-9}$$

Similarly to the Gambarova & Karakoc (1983) model, the above equations relate the stresses to the crack slip-to-width ratio, r. In this case, however, the stresses are independent of the ratio of the crack width to maximum aggregate size. It should be noted that since the effect of maximum aggregate size is ignored, the simplified model loses its accuracy if the crack opens too much (i.e., more than ~ 1 mm).

2.1.6 Summary

The aggregate interlock shear transfer mechanism is an important contributor to the shear resistance of reinforced concrete members. Push-off specimens are well suited for testing the aggregate interlock behaviour. However, to target the aggregate interlock shear transfer, the dowel action contribution from the reinforcement should be removed. Crack roughness contributes to aggregate interlock by forcing crack dilation (i.e., normal stress) and increasing the amount of contact areas perpendicular to shear displacement. A reduction in the deformability of the cement paste increases aggregate interlock, but then again, an increase in compressive strength also lowers crack roughness since the crack propagates through more aggregate particles. Indeed, in high strength concrete where the link between aggregates and the cement paste is stronger than the tensile strength of the aggregate particles, the shear crack intersects more aggregates and thus, is smoother. Large aggregates contribute to aggregate interlock by increasing crack dilation. Transverse reinforcement prevents the opening of shear cracks and induces compressive stress on the interface, increasing aggregate interlock friction. Researchers have produced aggregate interlock models to quantify shear and normal stresses across cracks based on crack slip and width measurements.

2.2 The impact of ASR on the aggregate interlock in reinforced concrete

2.2.1 Overview

As illustrated in Figure 2.14, ASR distinguishes itself from other deterioration mechanisms in concrete since microcracks initiate within the aggregates. In the early stages of ASR (i.e., low expansion levels), the formation of microcracks occurs mainly within the reactive aggregates, and the cement paste is barely affected. Eventually, the microcracks reach the cement paste and later form a network of cracks that link together.

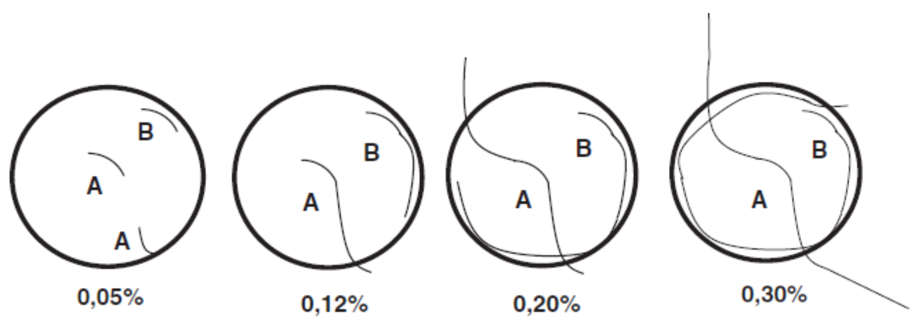

Figure 2.14: Qualitative ASR damage model for expansion varying from 0.05 to 0.30% (Sanchez et al., 2015)

Some years ago, Giaccio et al. (2008) believed that the decrease in mechanical properties due to ASR could not be directly associated with a level of expansion, arguing that the behaviour of affected concrete depended on the component materials and mechanisms involved in the reaction. However, Sanchez (2014) later obtained conclusive results in an extensive experimental research study with ASR-affected specimens including many concrete types (i.e., using coarse and fine reactive aggregates of several natures, different strengths, etc.). A correlation between the level of expansion and the reduction in compressive strength, tensile strength and elastic modulus can be seen in Figure 2.15. The development of ASR will normally induce a rapid and significant decrease in tensile strength and modulus of elasticity of an affected concrete but will have a significant effect on its compressive strength only at high expansion levels. Indeed, in the early stages of ASR development, since the cracks are still mainly within the aggregates and the cement paste (especially the ITZ) is still relatively sound, the compressive strength is not significantly reduced. In fact, the compressive failure mode is a ductile failure mechanism which rather results from the progressive formation of a network of cracks in the cement paste. Thus, when ASR cracks reach the ITZ, they become "fast tracks" to initiate a compressive fracture. (Sanchez et al., 2017)

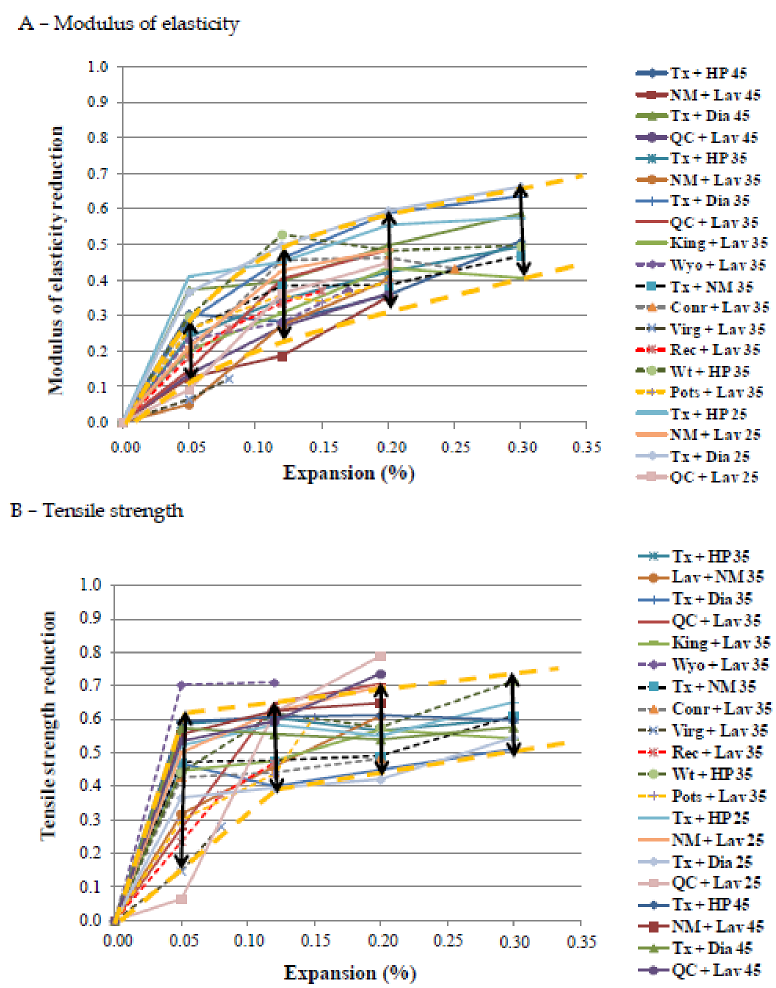

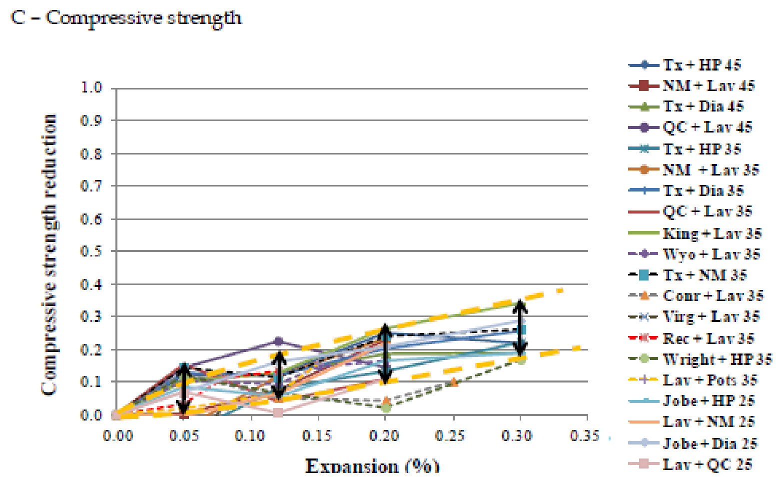

Figure 2.15: Mechanical properties losses (i.e. compared to a sound concrete presenting the same maturity) as a function of concrete expansion: A) Modulus of elasticity; B) Tensile strength and; C) Compressive strength (Sanchez et al., 2017)

To provide an order of magnitude and a comparison between the losses associated with each mechanical properties, at very high expansion levels (0.30 %), reductions up to 80%, 67% and 35% were obtained for the tensile strength, elastic modulus, and compressive strength, respectively. A more detailed presentation of the reductions in those three mechanical properties as a function of ASR development can be found in (Sanchez et al., 2017).

The more pronounced deleterious effect from ASR-induced cracks on the tensile strength than the compressive strength of affected concrete can be attributed to the fracture mechanics associated with each type of failure. Indeed, cracks which are perpendicular to an applied tensile stress result in planes of weakness in the material since they directly reduce the effective area of material under tension, thereby causing stress concentrations and provoking an early and brittle fracture mechanism once a critical crack length is reached. On the other hand, although ASR-induced cracks in the cement paste (especially those in the ITZ) offer a starting point for compression failure planes as mentioned earlier, they do not reduce the effective area under compression. The cracks that are perpendicular to the compressive stress simply get closed and then the stress is transferred across them. Parameters which can influence the loss of mechanical properties include the compressive strength and the reactive aggregates' characteristics (tensile strength, size, shape, texture, toughness, hardness, porosity, amount of closed cracks originating from aggregate processing operations, and capacity to generate sufficient amounts of ASR gel to induce extensive internal cracking) which impact the cracking patterns. (Sanchez et al., 2017)

2.2.2 Structural implications and long-term considerations

Although the consequences of ASR on the mechanical properties of concrete have been extensively investigated with mechanical testing of affected concrete specimens and cores retrieved from affected structures, the structural implications of ASR on real structures remain unclear (Gowripalan & Cao, 2018; Noël et al., 2017). Nevertheless, multi-scale testing, including experiments with large damaged reinforced concrete specimens, could help understand the influence of important parameters affecting the response of real structures (e.g. internal and external confinement, boundary and loading conditions, reinforcement ratio, element geometry, size effects, etc.) (Noël et al., 2017).

Even though ASR reduces the mechanical properties of plain concrete, most reported test results from ASR-damaged reinforced concrete specimens have not shown significant reductions in load capacity due to expansion confinement from internal reinforcement (Gowripalan & Cao, 2018; Noël et al., 2017). For example, while the ASR-damaged cylinders of Inoue et al. (1989) showed reductions as high as 64% in compression, 59% in tension and 48% in elastic modulus, due to chemical prestressing, the flexural capacity of their affected singly reinforced concrete beams was only reduced by less than 10% compared to sound specimens. Moreover, the reactive beams showed higher flexural cracking strengths than the normal specimens. Conversely, reductions in flexural capacity of up to 26% were obtained by Swamy & Al-Asali (1989) with affected singly reinforced small-scale beams.

There are two important things to consider about reactive specimens tested in the laboratory, which distinguish them from real-life structures. First, ASR-induced expansion being accelerated with favorable temperature and humidity conditions, it only takes months or a few years at most before the specimens are tested, but it takes around 15 to 25 years for concrete structures to be significantly distressed by ASR (Gowripalan & Cao, 2018; Noël et al., 2017). Thus, there is less time for the laboratory reinforced specimens' materials (i.e. steel and concrete) to creep and relax, and theoretically, the chemical prestressing should remain higher than for field structures. Second, laboratory specimens are usually loaded only after undergoing expansion, whereas real-life structures are rather loaded and likely already cracked in some locations prior to being significantly deteriorated by ASR (Noël et al., 2017). Nevertheless, although loading tests on rapidly expanded specimens are not entirely representative of the reality, it is generally believed that they can provide useful information for the assessment of real structures. Moreover, the in-situ load tests which have conventionally been used to assess the residual load capacity of ASR-affected structures (e.g., bridges) require more time, labour and money, are insecure, and may affect the integrity of the inspected structures (Gowripalan & Cao, 2018).

Considering the limitations of past experimental research described above, the long-term behaviour of ASR-damaged structures is not well understood. It is known that confinement stresses in affected concrete influence creep deformations (Kobayashi et al., 1988), that creep affects ASR deformations (Kawabata et al., 2017), and that the fatigue life of deteriorated reinforced concrete members subjected to repeated loading may be increased (Ahmed et al., 1998; Fujii et al., 1986) or reduced (Ahmed et al., 1999; Boenig et al., 2009), but the number of studies is limited.

2.2.3 The effect of ASR on the shear capacity of slender reinforced concrete members

The current knowledge of the impact of ASR on shear resistance of reinforced concrete is limited. Again, this is a complex topic in part because of the presence of many parameters varying in different structures. Also, the simultaneous contribution of various transfer mechanisms to shear resistance in reinforced concrete members (section 2.1.1) and multiple phenomena affecting those mechanisms before and after shear cracking add to the complexity. Although the reduction of concrete mechanical properties and cracking due to ASR may suggest that the shear resistance of affected reinforced concrete elements should be reduced, both increases and decreases have been obtained for reported test results from reinforced concrete slabs and beams (Gowripalan & Cao, 2018; IStructE, 1992; Noël et al., 2017).

<u>Slabs</u>

A wide number of shear tests were conducted on ASR-damaged reinforced concrete slabs without shear reinforcement, but the results are conflicting: Bilodeau et al. (2016) observed an increase in capacity of the order of 10%; Clark & Ng (1989) observed no significant effect on punching shear resistance, but obtained reductions of up to 30% for specimens with high expansion level (0.6%) due to concrete delamination parallel to the longitudinal reinforcement planes; Hansen (2019) experienced no significant decrease; and Den Uijl & Kaptijn (2002) obtained strength reductions of up to 25%.

The tests of Hansen (2019) and Den Uijl & Kaptijn (2002) both consisted of beams cut from ASR-affected bridge slabs without stirrups. The 2D-restrained slabs showed horizontal cracking due to the expansion confinement provided by the longitudinal reinforcement. In both studies, the concrete tensile strength was measured using cores extracted from the slab vertically and longitudinally. The strength reduction due to ASR was much more significant in the vertical unrestrained direction due to the horizontal microcracking. As a result of this and the ASR chemical prestressing effect, the critical shear cracks in the loading tests were flatter and longer, and a shear tension failure was obtained instead of a flexural shear crack. In the asymmetric four-point bending beam tests conducted by Hansen (2019) for example, smaller and shorter vertical flexural cracks were observed in damaged specimens due to expansion confinement effects. The undamaged beams failed from an existing flexural or flexural-shear crack, giving the critical shear crack a more vertical inclination, whereas in deteriorated specimens, a flat and inclined crack was formed as seen in Figure 2.16.

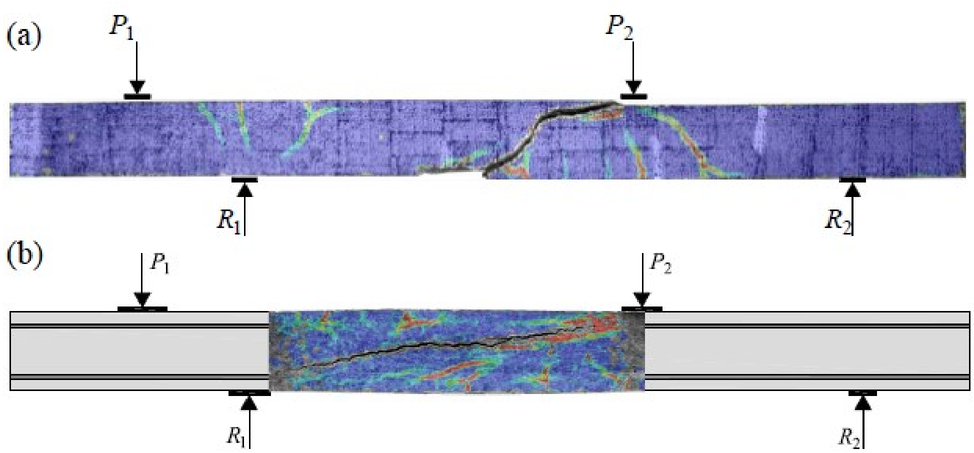

Figure 2.16: Crack pattern at failure for a continuous beam without ASR damage (a) or with ASR damage (b) (Hansen, 2019)

Hansen's (2019) test results suggest that the ASR-induced prestressing effect can compensate to some extent for the significant loss in material properties. On the other hand, Den Uijl & Kaptijn (2002) obtained a mean shear capacity that was 75% of the theoretical value that would have been expected for sound members. The specimens from the two similar research studies varied in terms of level of expansion, longitudinal reinforcement ratio, geometry, etc., and the influence of such parameters on the shear resistance of ASR-affected members is not well understood.

Beams and bridge girders

According to IStructE (1992), beams affected by ASR with a transverse reinforcement ratio of at least 0.2% do not show a significant decrease in shear capacity, and may even gain strength due to the prestressing effect caused by restrained expansion (subsection 2.2.3.1). Increases in shear strength and reduced deflections were obtained by some researchers (e.g. Abe et al., 1989; Ahmed et al., 1998; Smaoui, 2003). Inoue et al. (1989) tested damaged and undamaged reinforced concrete beams and, although the companion ASR-damaged cylinders showed a reduction in mechanical properties, the flexural cracking resistance of the damaged beams was greater. The authors observed that all the beams with a 1.74% longitudinal reinforcement ratio resulted in a shear failure for the healthy undamaged concrete and flexural failure for the damaged concrete, while beams with reinforcement ratios of 0.77 and 1.20% exhibited a bending failure mode for both types of concrete. This demonstrates the beneficial effect of the presence of longitudinal reinforcement on the shear capacity of reinforced concrete flexural members affected by ASR. Even in cases of large ASR degradation, no reduction in shear strength was experienced by Bach et al. (1993) with beams and by Deschenes et al. (2009) with large-scale bent cap beam specimens.

On the other hand, for beams without stirrups, both increases and decreases (up to 20%) in shear resistance have been obtained (IStructE, 1992). Also, in order to evaluate the influence of restrained expansion on both the load-carrying capacity and the deflection of beams, Noël et al. (2017) modeled ASR-damaged beams with the Vector2 software, and they obtained very little contributions from chemical prestressing.

It should be noted that the number of tests investigating the long-term structural behaviour of beams damaged by ASR is limited. Boenig et al., (2009) obtained a shear capacity reduction of approximately 14% for 15 years old affected bridge girders. It can be added that those girders showed the highest reduction in shear strength at their ends. Not only are those locations subjected to high shear stresses, deck joints are often located above them, so water infiltration is more important (Boenig et al., 2009).

2.2.3.1 The effects of expansion confinement and ASR microcracks on the aggregate interlock

As discussed in section 2.1, the aggregate interlock shear transfer across a crack with a certain slip and width is governed by the normal stress across the crack, the roughness of the crack, and the deformability of the cement paste. This subsection will demonstrate that: 1) the presence of reinforcement in concrete can confine ASR expansion and thus, increase the normal stress across shear cracks; and 2) the current knowledge about the effect of ASR micro-cracks on the roughness of shear cracks and aggregate interlock is limited.

ASR expansion confinement

Understanding the effects of confinement on ASR expansion and damage in reinforced concrete structures represents an initial step towards linking material to structural behaviour. The induced expansive pressure within the reacting aggregate particles and adjacent cement paste may be counteracted by various restraints, either internal (i.e., reinforcement) or external (e.g. applied loading and boundary conditions). Anisotropic confinement reduces ASR expansion in certain directions and increases it in other directions (IStructE, 1992; Multon & Toutlemonde, 2006), which is why maximum expansions take place where the restraint stresses are the lowest, and why the cracking occurs preferentially at these locations (Swamy, 1990). Due to conflicting observations by some researchers (Gautam et al. 2017; Giorla et al. 2012; Multon & Toutlemonde, 2006), it remains unclear whether expansion that is restrained in one direction becomes transferred in other unrestrained directions, or if the overall volumetric expansion is reduced. An expansion transfer has several repercussions such as reducing the induced compressive stress in the concrete in the restrained directions and increasing the material's anisotropy. Therefore, this topic and the effect of restraint in general deserves more research. It can also be noted that the same way compressive stress reduces expansion, tensile stress increases expansion (IStructE, 1992).

Reinforced and prestressed structural concrete elements, such as columns and beams, respond differently than unreinforced and stress-free elements to ASR. In reinforced concrete elements, expansion puts the internal bars under tensile stresses (IStructE, 1992) and causes bond stresses at the interface between the reinforcement and the concrete (Noël et al., 2017). The former phenomenon is called *chemical prestressing* since compressive stresses parallel to the reinforcement/confinement direction are induced in the concrete. Expansion confinement by the reinforcement can play a critical role in keeping the integrity of the core concrete. The effect of chemical prestressing on aggregate interlock is beneficial since the internal pressure in concrete closes the existing cracks (Gowripalan & Cao, 2018; Noël et al., 2017). However, over time, relaxation of the steel may reduce the induced compression, or the concrete may deform with creep

(Inoue et al., 1989). On the other hand, Swamy & Al-Asali (1989) reported largely irreversible concrete and steel strains in affected small-scale beams.

ASR expansion is not uniform over a reinforced concrete member's cross-section since it is significantly reduced in the vicinity of the bars and inside the reinforcement cage. An example can be seen on Figure 2.17, where the expansion perpendicular to the shear plane of a push-off specimen was modeled by Gorga (2018). The expansion is lower near the bars crossing the shear plane and in the core compared to the exterior of the cage. Thus, a significant expansion differential was measured in affected singly reinforced beams (Inoue et al., 1989; Swamy & Al-Asali, 1989) and large slabs with high reinforcement concentration in the bottom tensile zone (Allard et al., 2018). Allard et al. (2018) also noted that the expansion gradient over the depth of their slabs increased with further expansion. Varying expansion due to higher confinement in the bottom tensile zone has resulted in upward deflections in unloaded beams equivalent to chemical prestressing (Chana & Thompson, 1992; Swamy & Al-Asali, 1989).

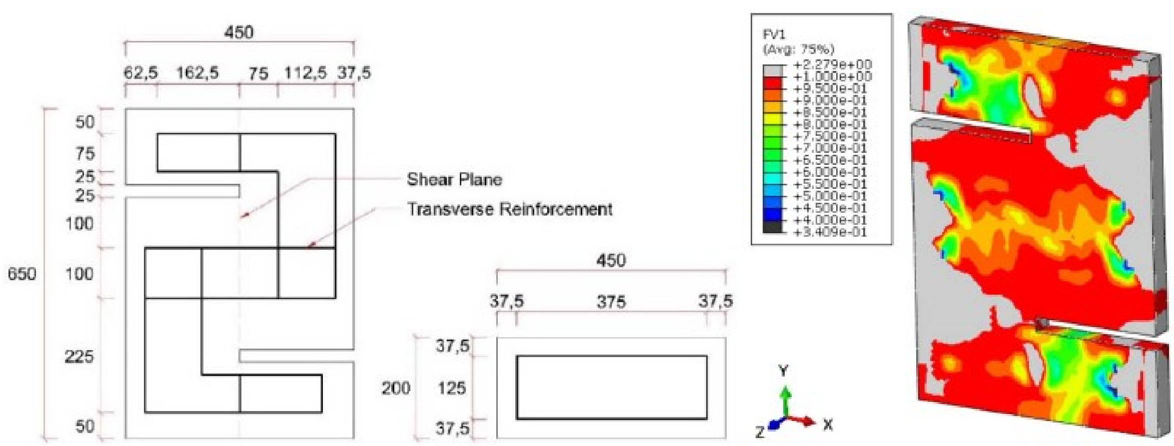

Figure 2.17: Variable expansion in the X-direction over the shear plane surface (Gorga, 2018)

Preferential orientation of expansion cracks is an observable sign of confinement, as cracks tend to orient themselves perpendicular to unconfined directions. For example, longitudinal cracking has been observed in several experiments with affected reinforced concrete beams and slabs (Chana & Thompson, 1992; Den Uijl & Kaptijn, 2002; Hansen, 2019).

IStructE (1992) collated data from previous experiments with ASR-affected reinforced concrete members to study the effect of steel reinforcement ratio and expansion rate on the induced concrete compressive stress and level of expansion. An increase in reinforcement ratio reduces ASR expansion and induces a higher compressive stress in the concrete (Figure 2.18a), and a higher expansion rate increases the induced compressive stress (Figure 2.18b). Therefore, since the expansion is slower in real structures compared to specimens accelerated in a laboratory, the compressive stress induced by chemical prestressing is likely reduced. According to IStructE (1992), neglecting rapid laboratory tests, the maximum concrete compressive stress due to internal confinement tends to remain below 4 MPa. The authors note that practically, this implies that if a concrete is sufficiently reactive, internal steel bars can possibly yield when the reinforcement ratios are less than 1.6% or 0.9% for mild (f_y = 250 MPa) and high yield steel (f_y = 450 MPa) respectively. Berra et al. (2010) found that concrete stresses due to externally restrained AAR expansion could reach up to approximately 5 MPa (Berra et al., 2010).

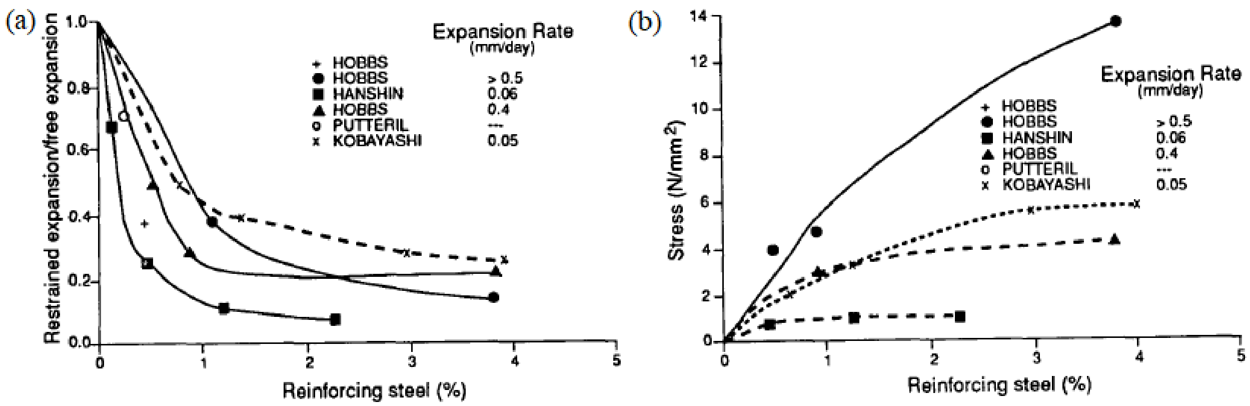

Figure 2.18: Restrained expansion (a) and induced chemical prestressing (b) for different reinforcement ratios (IStructE, 1992)

Researchers have also measured the tensile strains induced in the steel reinforcement by chemical prestressing and derived the tensile stresses from the steel properties (i.e., elastic modulus or yield stress). Hayes et al (2018) and Wald et al (2017) have respectively measured ASR-induced tensile stresses of 200 and 420 MPa (i.e., yield stress) in the reinforcing steel of large 2D-restrained concrete elements, while Hansen (2019) obtained mean stresses varying from 198.7 to 273.8 MPa for affected bridge slabs. On the other hand, Allard et al. (2018) measured an average strain of only 0.035% near the mid-span of the bottom longitudinal steel reinforcement of a highly expanded one-way slab, which corresponded to a stress as low as 72 MPa. However, this longitudinal reinforcement consisted of dense layer of ten closely spaced 25 M bars, resulting in significantly reduced concrete expansion at the height of the steel. In contrast, Swamy & Al-Asali (1989) measured strains up to 0.234% in the bottom tensile 8 M steel bars of affected beams, which corresponded to 80% of the 560 MPa proof stress, but these specimens were significantly more expanded at the height of the steel. Interestingly, these two studies showed that the concrete surface expansion at the height of the reinforcement is only slightly above the measured strain in the steel. If a reinforced concrete element is very lightly reinforced and highly reactive, the internal steel reinforcement may even rupture (Miyagawa, 2013). The transverse reinforcement (i.e., stirrups) is typically more prone to yielding or rupture because its density and size are likely inferior to those of the longitudinal bars, resulting in less confinement (Deschenes et al., 2009).

Anisotropic expansion due to confinement results in anisotropy of the concrete mechanical properties. Den Uijl & Kaptijn (2002) and Hansen (2019) both extracted cores vertically and horizontally from 2D-restrained slabs without vertical reinforcement. They obtained a more significant reduction in mechanical properties in the vertical direction due to the vertical expansion and horizontal cracking (Figure 2.19). Thus, the direction of coring for inspection in ASR-affected structures should be carefully selected since the orientation of cracking directly influences microscopic/macroscopic analyses (Barbosa et al., 2018; Martin et al., 2012; Noël et al., 2017).

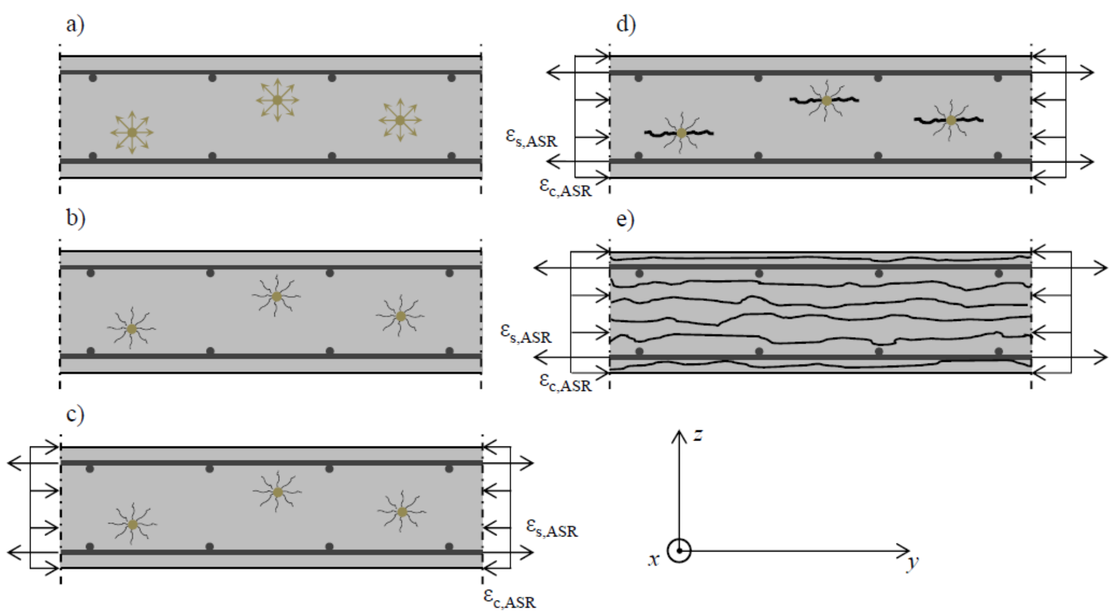

Figure 2.19: ASR cracking in a 2D-restained slab without stirrups (Hansen, 2019)

<u>ASR microcracks</u>

As explained in subsection 2.1.3, the weakest link in concrete is generally the contact area between the cement paste and the aggregates, the ITZ, which is why cracks usually go through the paste outlining the aggregate particles. Such crack propagation results in rough shear cracks, thereby increasing the aggregate interlock stress transfer. If a crack intersects several of the aggregate particles, as previously observed with low-strength aggregates or high-strength concretes, the roughness of the crack is reduced, the crack opening path is steeper (i.e., large shear displacement compared to crack opening) and the aggregate interlock shear resistance is reduced. A similar effect may be observed in the case of concrete affected by ASR because of the presence of opened cracks within the aggregates, which may offer the easiest path for the shear crack. To the knowledge of the author, the literature presents no conclusive results on the effect of ASR precisely on aggregate interlock. However, in order to fill this knowledge gap, a group of researchers from Laval University and McGill University recently conducted push-off tests with specimens presenting different ASR-induced expansion levels (Sanchez et al., 2016). Specimens with and without stirrups crossing their shear plane were tested. The reinforced specimens had either two or four stirrups, corresponding to reinforcement ratios of 1.12% and 2.24% respectively. The following three ASR damage/expansion levels were selected:

1) low expansion level (i.e. 0.05%), where the cracks are mainly still located within the aggregates;
2) moderate expansion level (i.e. 0.12%), where the cracks start reaching the cement paste;
3) high expansion level (i.e. 0.20%), where the cracks are present in the cement paste;

The results of the push-off tests have yet to be published, but the results of direct shear tests conducted on concrete cylinders with different expansion levels can be found in Sanchez et al. (2016) and De Souza et al. (2019). In these papers, a setup developed by Barr & Hasso (1986) was used to test the specimens under pure shear without moment. As seen from Figure 2.20, the specimens are notched at the center of their height, positioned horizontally between two plates, and then loaded perpendicularly to their main axis with reversed supports such that a brittle shear failure occurs at the notch. The specimen's geometry and the shear and bending moment diagrams can be seen on Figure 2.21. Sanchez et al. noted that the vertical crack went through reactive coarse aggregates, but around them when only the sand particles were reactive (Figure 2.22). This is consistent with the crack patterns observed by Sanchez (2014) for reactive sand and for reactive coarse aggregates (Figure 2.23). According to Sanchez et al. (2016) and De Souza et al. (2019), it is possible to follow the progress of ASR damage with the cylindrical test setup since the decrease in shear strength can be correlated with expansion level (Figure 2.24). It should be noted that in this compact shear test, after the crack forms, there is no aggregate interlocking, as the two halves are completely separated.

Figure 2.20: Cylindrical setup for testing the shear strength of concrete (Sanchez et al., 2016)

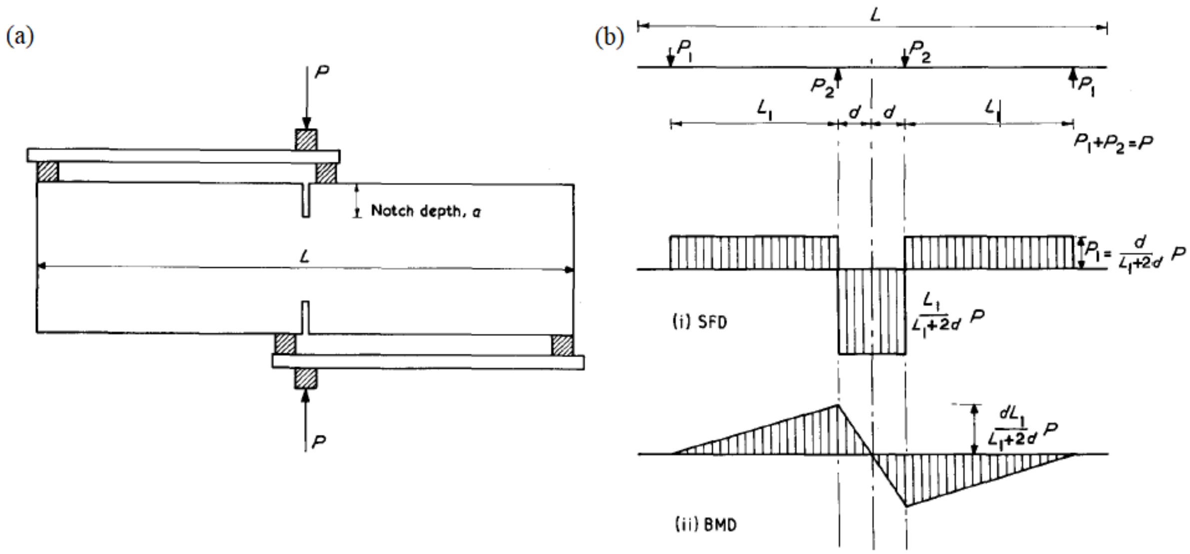

Figure 2.21: Compact shear test specimen. Test specimen geometry (a) and shear force and bending moment diagrams (b) (Barr & Hasso, 1986)

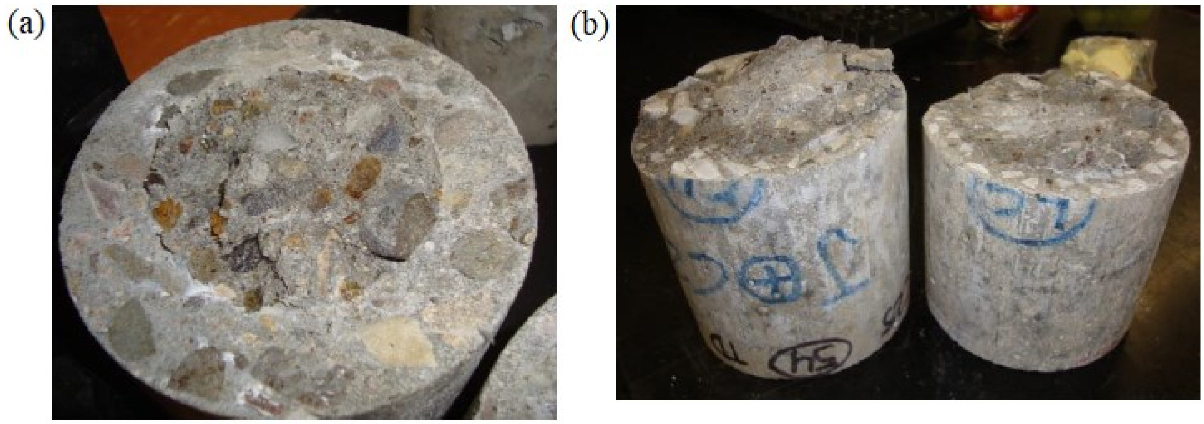

Figure 2.22: Failure planes for ASR coming from a reactive coarse aggregate (a) and a reactive sand (b). (Sanchez et al., 2016)

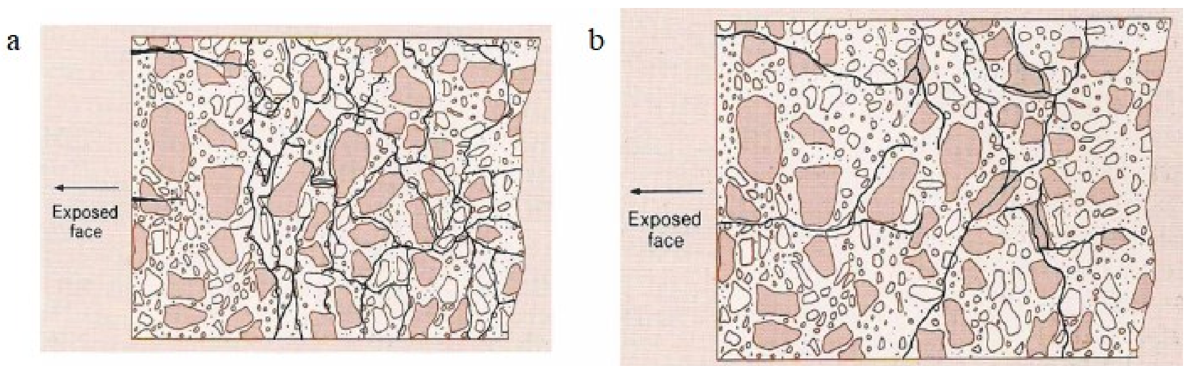

Figure 2.23: Typical ASR crack pattern in concrete caused by (a) reactive sand vs. (b) Reactive coarse aggregate (Sanchez, 2014)

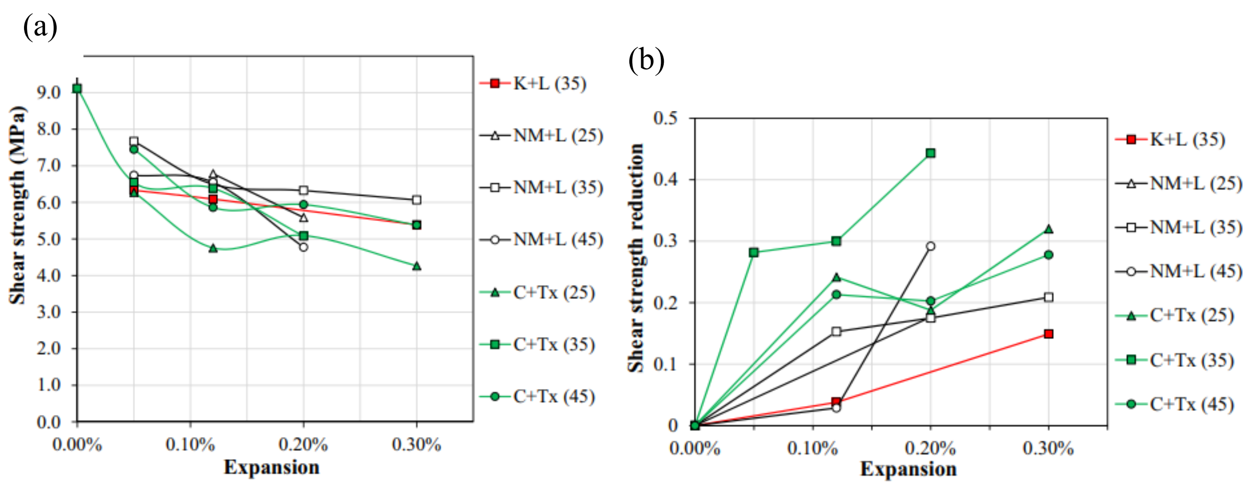

Figure 2.24: Direct shear strength (a) and direct shear strength reduction (b) with increasing ASR expansion (De Souza et al., 2019)

A few researchers have demonstrated that ASR expansion is higher for reactive sand compared to reactive coarse aggregates (Jurcut, 2015). However, it was also shown that coarse aggregate fractions contribute more to aggregate interlock, enhancing the crack roughness and the crack opening during shear displacement. Thus, one could argue that with sufficient cracking within reactive coarse aggregates, the reduction of aggregate interlock may be more significant than for reactive sand. In their parametric analysis using the software VecTor2, upon simulating coarse aggregates splitting by reducing the size of aggregates in reinforced concrete beams from 10 mm to 6.7 and 5 mm, Noël et al. (2017) obtained reductions in shear capacity of 40% and 50% respectively. Furthermore, a change in failure mode from flexure to shear was experienced for some of the modeled beams with stirrups.

2.2.4 Summary

The effects of ASR on concrete are fairly well-known at the material scale; there is a general consensus about the impact of the distress mechanism on the mechanical properties of concrete, but its structural implications are still unclear due to their complexity and a lack of multiscale tests in past research programs. Although it would be reasonable to think that the reduction in mechanical properties of the concrete and the microscopic distress features (i.e., opened cracks within the aggregates) associated with ASR would lead to a corresponding reduction in the shear capacity of affected structures, due to the chemical prestressing effect, affected reinforced concrete members have in many cases shown no significant reduction in shear strength. However, the number of past loading experiments on ASR-damaged reinforced concrete members is limited and the effects of expansion level and confinement on the aggregate interlock mechanism have not been explicitly investigated.

2.3 The use of DIC to monitor concrete structures

The DIC photogrammetry measurement technique has been successfully used to measure full-field surface deformations of loaded concrete members in laboratory-controlled environments, and it is gradually being incorporated in field structural monitoring applications due to its several benefits. In this section, the fundamentals of 2D DIC will first be introduced. Second, past experiments in which the accuracy of the technique has been investigated will demonstrate the capabilities of the technique. Third and finally, the challenges, limitations, and possible sources of 2D DIC measurement errors will be discussed.

2.3.1 The fundamentals of DIC in loading experiments

DIC was developed by Sutton et al. (1983) and has been used in loading experiments by researchers from different fields for measuring the surface displacements, velocities, and accelerations of materials (Pan et al., 2009). Two-dimensional DIC measurements require the use of a digital camera and a computer DIC-software for post-processing the photos or video, while 3D measurements require the use of multiple cameras (Helfrick et al., 2011). Although 2D DIC techniques have been used with curved targets (e.g. Dutton et al., 2011), they are more appropriate for inspecting a flat surface which is perpendicular to the optical axis of the camera (Figure 2.25) (Pan et al., 2009).

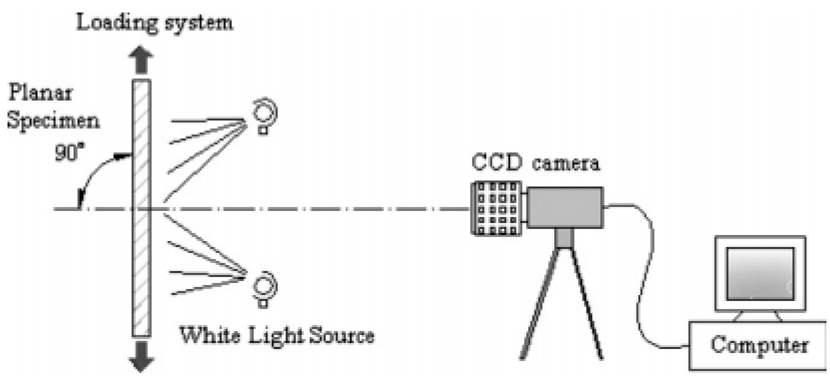

Figure 2.25: Typical test setup for 2D DIC measurements (Pan et al., 2009)

For a loading experiment, an initial photo is taken prior to loading. Then, during the test, the load can be applied continuously, while the photos (or the video) are taken, or the load may be paused at load or displacement increments for taking several pictures. The DIC technique requires that the camera position remains the same for all captures since the displacements are directly extracted from the images (Yoneyama & Ueda, 2011). Thus, to avoid movement, the camera is usually connected to a tripod or a stable frame and it is good practice to use a remote control for the captures (Gamache & Santini-Bell, 2009; Shah & Kishen, 2011). Dutton et al., (2011) even used a rubber pad underneath their camera to reduce vibrations.

DIC measurements are in pixels. By knowing the relationship between the number of pixels and a physical dimension in the plane of the inspected surface, i.e., the scale factor (pixels/mm), the displacements and strains can be determined. A contrast on the surface of the inspected element is necessary to enable the DIC-software to track deformations between subsequent images

(Barranger et al., 2010; Lecompte et al., 2006). Therefore, a random speckle pattern is typically added onto the surface of the specimen for image pixels to present different grey-scale intensities and for the DIC-software to calculate their movement (Figure 2.26). The surface texture deforms together with the specimen and improves the quality of correlation between images. With concrete specimens, the speckle pattern is often done by painting a white primer and spraying black paint dots on it in a random pattern. For good gray level variation, it is recommended to illuminate the inspected surface evenly during the image acquisition. A white light source or natural light can be used (Pan et al., 2009).

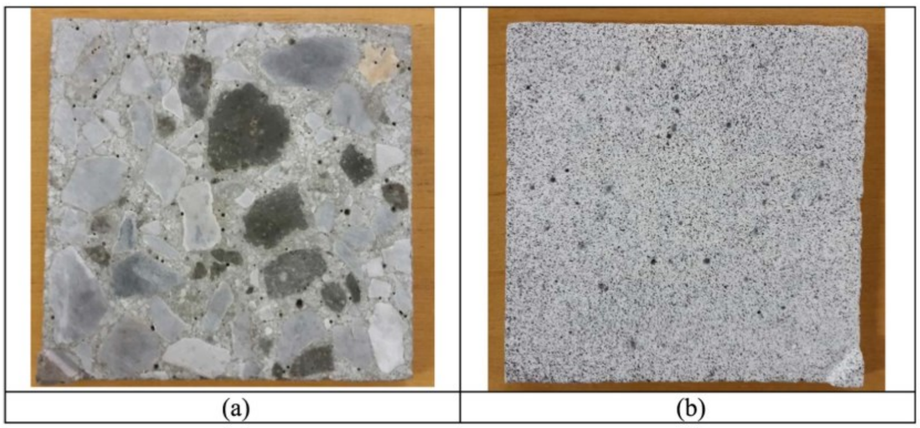

Figure 2.26: Preprocessing of a specimen for DIC: a) before random mapping, and b) after random mapping (Teramoto et al., 2018)

After image acquisition, the DIC program tracks the displacement of subsets (or facets), squares made up of a defined number of pixels which may be created manually by the user or automatically generated (Figure 2.27). Ideally, to be distinguishable from its surroundings, a subset should present a wide variation in gray levels. This is critical for accurate measurements (Dutton et al., 2011). The user defines the size of subsets in pixels and can position them where preferred on the reference undeformed image.

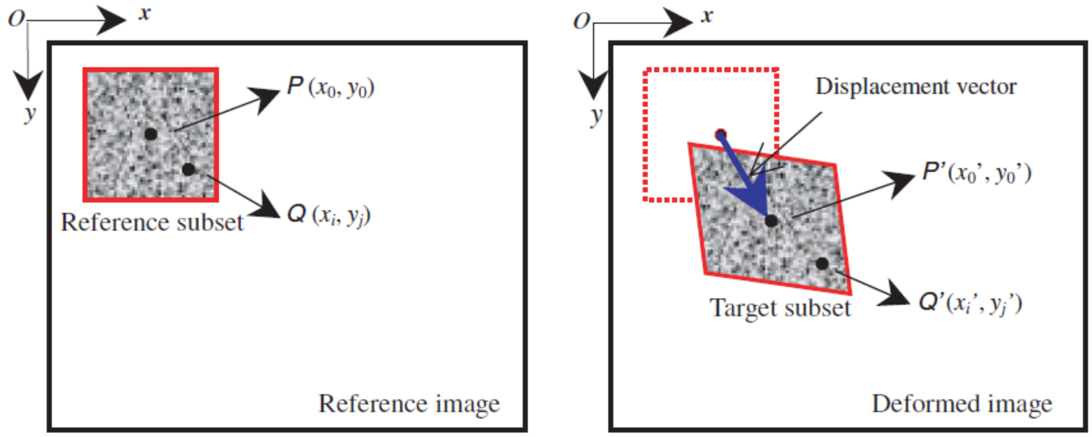

Figure 2.27: Undeformed and deformed subset tracked by a DIC-software (Pan et al., 2009)

2.3.2 Recording shear crack kinematics

Since the DIC technique enables measurements of deformations on a surface of desired size, it is not necessary to know exactly where a crack will form, as long as it appears within the field of view covered by the photos. Thus, the DIC technique has been widely and successfully used in loading tests to detect the onset of cracking and examine fracture mechanics in concrete, making it an adequate tool for understanding the shear failure process (Figure 2.28). For example, researchers such as Cavagnis et al. (2018b), Huber et al. (2016), and Zarate Garnica (2018) have tested reinforced concrete beams in shear while measuring the width, slip, and orientation of the critical diagonal crack, from its initiation up to failure of the specimens. They combined those measurements with constitutive laws in order to evaluate the contributions of the different shear transfer mechanisms at numerous times during crack propagation.

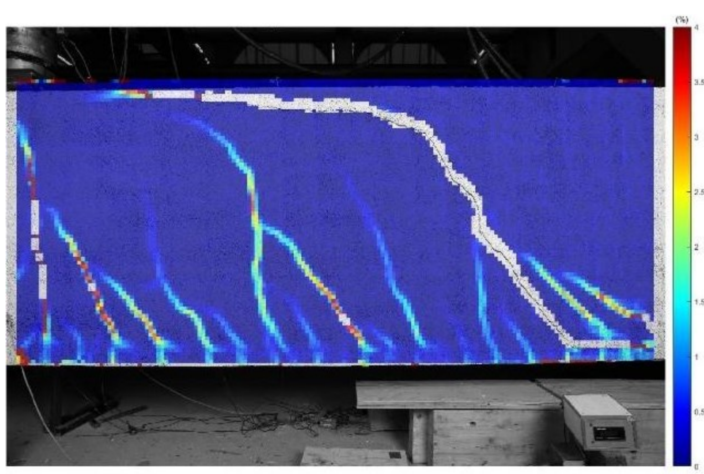

Figure 2.28: Beam shear test using DIC to measure crack width and slip (Zarate Garnica, 2018)

According to Hoult et al. (2016), it would be beneficial to use the DIC technique for the long-term monitoring of shear cracks in real structures since full-field quantitative measurements would lead to an improved estimation of the residual shear capacity of overloaded members. However, they emphasize the importance of ensuring good accuracy in the DIC measurements and conducting validation testing for each SHM application. The authors conducted beam tests with DIC to investigate the effect of curvature on measured crack slip. As seen from the pairs of subsets A-A' and B-B' on Figure 2.29a, an apparent additional crack slip results from the beam curvature. To eliminate it, the authors proposed an approach involving the use of four measurement planes in the DIC analysis (Figure 2.29b). Normally, to measure the distributed opening and sliding of the crack along its length, only a line of subsets is needed on each side of the crack (i.e., 2nd and 3rd lines of subset on Figure 2.29b). By adding a measurement plane on each side of the crack (i.e., 1st and 4th lines of subset on Figure 2.29b), an apparent slip entirely due to curvature can be measured between the 1st and 2nd planes, and between the 3rd and 4th planes. Then, the two apparent slips are averaged and subtracted from the measured slip between the 2nd and 3rd measurement planes to find the true crack slip.

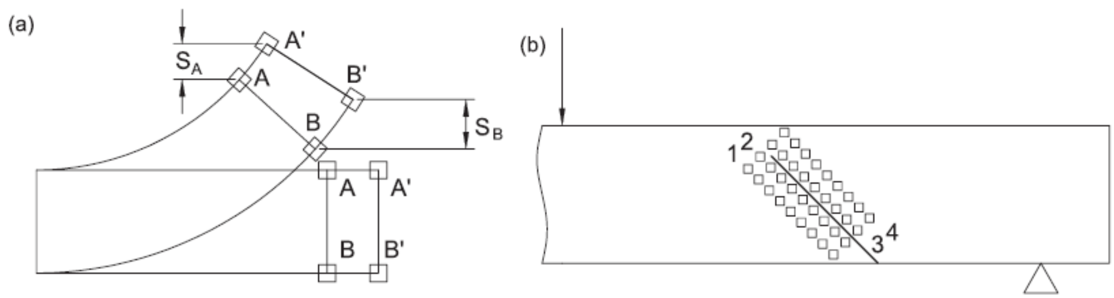

Figure 2.29: Apparent slip due to exaggerated beam curvature (a); The four measurement planes technique (b). (Hoult et al., 2016)

2.3.3 Other structural health monitoring applications

The measurement of bridge deflections certainly represents the SHM application of the DIC technique with the most past case studies (Niezrecki et al., 2018). These structures often require a load rating, which can be determined from a standard load test in which the real-time deflection at mid-span is monitored during a live load crossing. Abolhasannejad et al., (2018) presented a review of many non-contact image-based measurement methods for monitoring bridge real-time deformations and concluded that these methods are usually better than other contact-based and non-contact-based methods. Compared with other conventional equipment such as surveying and global positioning system, the DIC technique allows easier production of entire bridge deflection curves without traffic disruption and with very rare access limitation due to surrounding bridge environment (Gamache & Santini-Bell, 2009; Santini-Bell et al., n.d.). Even the deflection of a very stiff bridge, requiring high displacement measurement accuracy, has been successfully recorded by 2D-DIC during static and dynamic loading tests (Murray et al., 2014). To track bridge deflections, an artificial displacement target with a speckle pattern on it is often mounted to the bridge, or the speckle pattern may be painted to the bridge's surface. However, it is also possible to rely on features extracted from the natural concrete texture of the bridge (Abolhasannejad et al., 2018; Gamache & Santini-Bell, 2009; Wang et al., 2017).

Other SHM applications of the DIC technique which have successfully been tried include the measurement of: curvatures in flexural members (Dutton et al., 2014; Mahal et al., 2015); small-magnitude (<0.1%) homogeneous strain fields (Acciaioli et al., 2018); non-uniform concrete drying shrinkage (Dzaye et al., 2019); plastic shrinkage of fresh concrete (Zhao et al., 2018); micro-cracking around coarse aggregates during drying shrinkage of concrete (Maruyama & Sasano, 2014; Mauroux et al., 2012); ASR-induced expansion and micro-cracking (Teramoto et al., 2018); surface concrete displacements and strains caused by reinforcement corrosion (Jin et al., 2018); concrete spalling (Nonis et al., 2013); and the vibrations or dynamic response of bride hanger cables (Atkins, 2017; Niezrecki et al., 2018).

2.3.4 Challenges and limitations associated with 2D DIC techniques

The DIC technology shows a wide applicability (Niezrecki et al., 2018), but there are a few requirements which may limit its use:

<u>Visibility</u>

DIC techniques are vision-based, and thus, they are not suited for measuring internal strains or evaluating surfaces that are not visually accessible (i.e. no direct line of sight). For example, as explained in subsection 2.2.3.1, a concrete element affected by ASR may undergo an expansion which is not uniform over its cross-section, but the DIC expansion measurements will only be representative of the surface expansion. Nevertheless, for the monitoring of existing structures, this accessibility limitation often also applies to conventional non-destructive measurement techniques.

Flat and smooth inspected surface

As mentioned previously, when using a single camera, the displacements must occur within a plane, otherwise errors will be generated. For improved accuracy, the surface should also be smooth. This limitation may be overcome with 2.5D and 3D DIC systems using algorithms based on stereovision, but those are more costly and less accessible, requiring two or more calibrated cameras to measure 3D displacement fields (Helfrick et al., 2011).

Addition of artificial targets

Certain SHM applications of the 2D DIC technique may require the addition of artificial targets in the plane of the inspected surface, within the field of view of the camera. However, some structure surfaces may be hard or impossible to access. Furthermore, the preparation of a measurement surface or the fabrication, installation and detachment of artificial targets add costs, complexity and time to inspections. Nevertheless, as mentioned by Hoult et al., (2016), instead of adding a contrast, bolt patterns, rust, or color variations may be used. It is also possible to project a pattern onto the measured surface instead of painting it or mounting it (Nonis et al., 2013; Sabato et al., 2017). In all cases, long-term DIC monitoring applications involve challenges associated to changes in moisture content, surface stains, discoloration, efflorescence, or spalling and delamination. Those may prevent the proper tracking of targets due to loss of data points.

Environment stability

In laboratory experiments, the lighting, temperature and camera positioning are easily controlled. In the field, wind, temperature changes, light fluctuations (e.g., due to a passing cloud shadow), rain/snow, and ground motions may prevent the use of DIC techniques or have a significant influence on the measurements. In a case study addressing the practical issues associated with long distance outdoor bridge deflection DIC measurements, Gamache & Santini-Bell (2009) found a significant influence from environmental factors, measuring a maximum mid-span deflection of 12 mm compared to a true value of 3.8 mm. The inspection of underwater structures may present several additional challenges and limitations for the DIC technique, but for brevity, those have not been explored.

2.3.5 Measurement errors and correction techniques

Two-dimensional DIC measurement errors are inevitable and may arise from different sources related to the inspected element, loading, and imaging, or to the DIC-software correlation algorithm. For example, various sources of noise (e.g. shot, thermal, cutoff, and readout noises) are unavoidable during image acquisition (Pan et al., 2009).

Regardless of the total displacement being measured, for a given spatial resolution (i.e., pixels/mm of measured surface), the absolute measurement error is usually the same (Lee et al., 2012; Murray et al., 2014). Thus, for small-scale DIC measurements or long-distance measurements, the relative measurement error will be increased. In both cases, the accuracy of DIC measurements is closely related to the scale factor (i.e., the number of pixels per mm of inspected surface), which needs to be large enough for small pixel displacements to be trackable. When measuring strains with DIC, a larger gauge length (in pixels) increases the accuracy since the subpixel error is divided by a larger denominator. The scale factor and gauge length can be enhanced by selecting a high-resolution camera, a lens with a long focal length, and by positioning the camera as close as possible from the inspected surface while keeping the required elements within the field of view (Hoult et al., 2013).

It is worth noting that the acceptable level of error also depends on the magnitude of the deformations being measured. For example, Mirzazadeh et al. (2016) found that temperature-induced errors as high as 60με/°C resulted in crack width errors of only about 0.2%. On the other hand, according to Hoult et al., (2013), concrete structures under service load may deform by less than 100 με and thus, the authors identified the maximum acceptable strain measurement error as 5 με. When mitigated under the right experimental conditions, DIC displacement measurement errors are usually kept below fractions of a pixel, so the above accuracy may be achieved.

This subsection discusses error sources while mentioning possible mitigation measures. For brevity, the errors related to the image processing correlation algorithm (i.e., an unreliable correlation criterion, a bad type of subpixel interpolation scheme, or a low-order subset shape function (Pan et al., 2009)) are not included.

Off-axis camera positioning

For certain DIC technique applications, such as the measurement of deformation of a large structure, the charge-coupled device (CCD) sensor of a camera can't be positioned parallel to the inspected surface. Such off-axis camera positioning results in 2D DIC measurement errors and thus, a calibration process should be used (Pan et al., 2009).

Errors due to an off-axis optical setup can be reduced by using a telecentric lens and/or positioning the camera far from the inspected surface to produce a similar effect (Pan et al., 2009). Also, to improve inspections of bridge deflection, Pan et al. (2016) recently developed an advanced deflectometer which uses off-axis DIC for measuring real-time vertical deflection in multiple locations over a bridge length.

Out-of-plane movement from inspected element

When using a conventional lens, distance change between the camera and inspected element results in a different image magnification, leading to additional apparent in-plane displacements. According to Hoult et al., (2013), even a very small out-of-plane movement may lead to a significant relative DIC measurement error. While a larger movement induces a greater error, a longer effective distance between the camera and the inspected surface reduces the error. This is described by the following relationship derived by Sutton et al. (2009):

$$\varepsilon_{\mathrm{error}} = \frac{\mathrm{dy}}{\mathrm{y}} \quad (2\text{-}10)$$

Where dy is the distance reduction between the inspected surface and the camera and y is the initial distance (Figure 2.30).

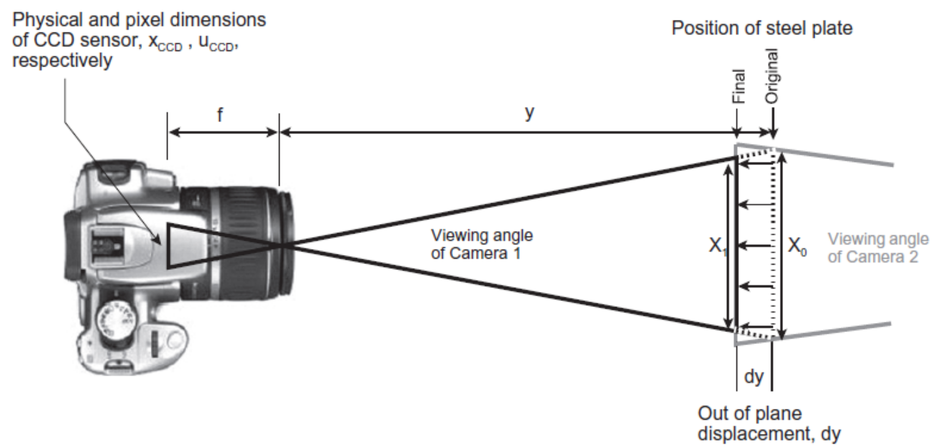

Figure 2.30: Effect of an out-of-plane movement on the image captured by the camera (Hoult et al., 2013)

Of course, increasing the distance y can be achieved by simply moving the camera father away from the inspected surface, but this reduces the strain measurement accuracy. Another possibility would be to use a lens with a longer focal length, *f* (Hoult et al., 2016). From the above figure and using similar triangles, it can be visualized how this would reduce the viewing angle of the camera and allow to position it further away from the inspected surface while keeping the same field of view (X_0). The effective distance y can also be increased with a telecentric lens as the paths of light entering those lenses are nearly parallel, which means that the magnification is maintained independently of the distance y (Hoult et al., 2013). However, telephoto lenses are expensive and offer a limited field of view. Other solutions to correct the effect of out-of-plane movement have been discussed by Hoult et al., (2013), including the placement of a fixed reference object of known dimensions in the plane of the measured surface. Upon correction of induced errors, the authors achieved similar strain resolutions to conventional strain gauges.

Poor surface texture

The accuracy of the DIC results depends closely on the quality of the speckle pattern. As mentioned earlier, a speckle pattern should be random and present a high contrast to ensure subset identification. Figure 2.31 distinguishes good from poor patterns. A proper surface pattern is isotropic and doesn't have a preferred orientation to avoid repeated textures. Also, the size of black dots should be chosen according to the scale factor (pixels/mm). For example, at closer range, the mean speckle size should be smaller. This will result in the highest variations of grey-scale intensity within only a few pixels (Lecompte et al., 2006; Pan et al., 2009).

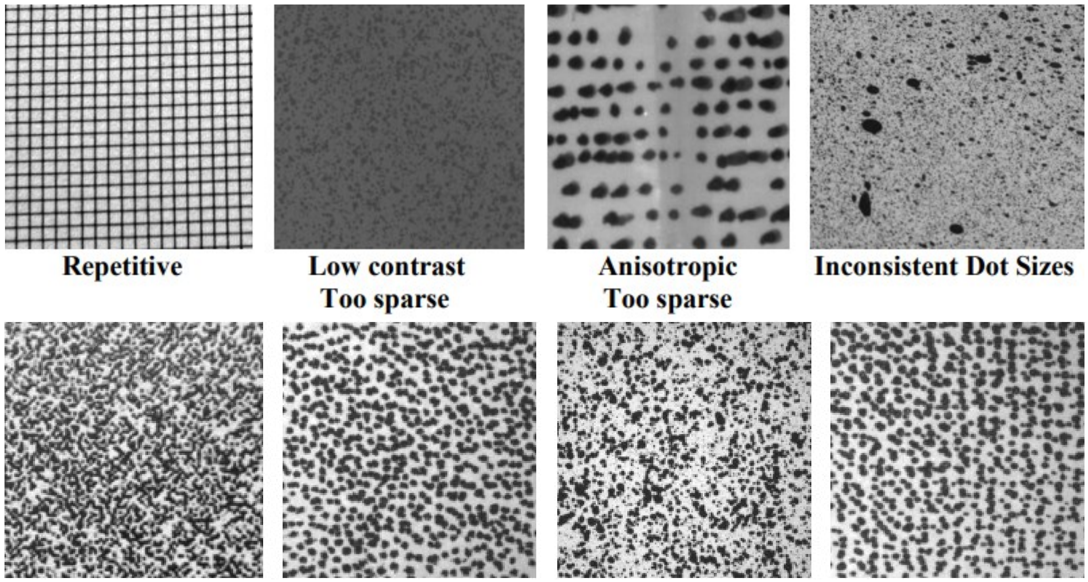

Figure 2.31: Bad patterns (top row) and good patterns (bottom row) (Correlated Solutions, n.d.)

Concrete usually has a uniform grey color and thus, a poor surface texture. Not adding an artificial pattern to a concrete structure prior to monitoring its deformations can drastically increase the probability of a wild vector due to a false subset identification in the DIC analysis. This was demonstrated by Dutton et al., (2011) with compression tests of cylinders with and without a speckle pattern painted on their surface, as they noted a significant contribution from the added texture to the accuracy. In fact, the size variations of the untextured cylinders were not appropriately tracked. It should be noted, however, that they conducted 2D measurements with a curved surface. Nevertheless, a high spatial resolution may help avoid errors caused by the absence of an artificial texture and, as mentioned in subsection 2.3.3, researchers have been able to track absolute displacements (i.e., bridge deflections) with natural concrete texture.

Poor camera quality

As discussed previously, a higher camera resolution increases the accuracy of DIC measurements. When measuring absolute displacements such as a bridge deflection, the jitter characteristics of the camera should also be considered as the random line shifting in video imagery also leads to measurement errors (Luo et al., 2001). To correct those small image movements, several images may be averaged together into a single composite image using MATLAB (Hoult et al., 2013; Murray et al., 2014). Also, a fixed reference object may be used to subtract its apparent movement from the measurements. It can be noted that this method will also correct for apparent movement due to camera drift (i.e., rigid body translations of the entire images) which may be caused for example by CCD self-heating during long recording sessions.

Lens distortion

Radial and tangential distortion from low-cost optical imaging lenses produce additional displacements, but if the influence is significant, various distortion correction techniques may be used, such as those of Yoneyama et al. (2006), Zhang et al. (2006), or Pan et al. (2013). Errors caused by image distortion are relatively small, especially at the center of the images (Pan et al., 2013), and they are considered negligible for crack measurement (Hoult et al., 2016).

Light and temperature fluctuations

Outdoor lighting fluctuations may cause noise in the measurements. It is also recommended to use a correlation criterion insensitive to the offset and linear change of illumination lighting such as the zero normalized cross correlation (ZNCC) criterion (Kohut et al, 2017; Pan et al., 2009). Also, temperature variations result in thermal deformation of the structure and camera system, which may be a problem when image acquisition occurs over long periods of time. According to Gamache & Santini-Bell (2009), turbulent air heating causes small localized distortion within an image. The authors recommend image acquisition at night with artificial light to ensure thermal equilibrium of the structure and eliminate image variability due to sun motion, clouds, and moving shadows.

Camera movement

Wind and ground vibrations can cause movement of the optical assembly. The deflection vs. time curve from Gamache & Santini-Bell (2009) suggests that the dominant source of error in their study was the wind gusts, since the rate and direction of the observed drift changed several times. Their large measurement discrepancy (mid-span deflection of 12 mm compared to a true value of 3.8 m) could be attributed to the high distance and magnification used (effective focal length of 665 mm), as even a small rotation of the camera would result in a high error. For the optical system to be less sensitive to wind effects, they recommended the use of a tripod with rugged short legs and an additional support near the aperture end of long camera lenses. Installation of a windshield equipment on the camera has also been suggested by Lee & Shinozuka (2006).

In order to account for measurement errors occurring when the camera moves or vibrates during the image data acquisition, Abolhasannejad et al., (2018) developed an image motion correction algorithm to combine with DIC measurements. In order to detect and distinguish global motion from local motion in the images captured after the first one, a square sub-image, which includes fixed natural or artificial distinctive features, is used. This region of interest being affected by translation and/or rotation of the image due to camera movement, it can be used for determining and subtracting the global motion, leaving only local and true deformations.

Very similarly, Yoneyama & Ueda (2011) came up with a methodology for correcting DIC measurement errors due to camera movement caused by environmental factors such as wind or ground oscillations during infrastructure inspections. They used an equation of perspective transformation in which the coefficients are determined through the method of least-squares, from the DIC-measured movement of fixed reference points in the vicinity of the inspected element. The equation was subsequently used for determining the true coordinates of other points of interest.

The long-term management of concrete structures generally involves periodic visual inspections, often conducted several years apart. The use of DIC techniques to follow the gradual evolution of deterioration and overloading signs cannot be practically achieved without camera movements between image captures, unless expensive surveying equipment and time-consuming camera placement procedures are used. Changes in camera position and orientation result in perspective distortions in the images, which translate into errors in the subsequent DIC measurements. Nevertheless, images captured from different positions in space may be aligned with image registration methods before the computation of the displacements. For example, to correct for perspective errors in deflection measurements, Uhl, Kohut and their associates have used homography mapping to rectify images captured during several static loading experiments (Dworakowski et al., 2016; Kohut et al., 2017; Kohut et al., 2014; Uhl et al., 2011). They computed a homography matrix for each distorted image using fixed rectangular markers, coplanar with the loaded structure's plane, added in the field of view (Figure 2.32). Note that for a given off-axis camera positioning between subsequent images, the camera perspective change will be lower if the distance between the camera and inspected element is higher.

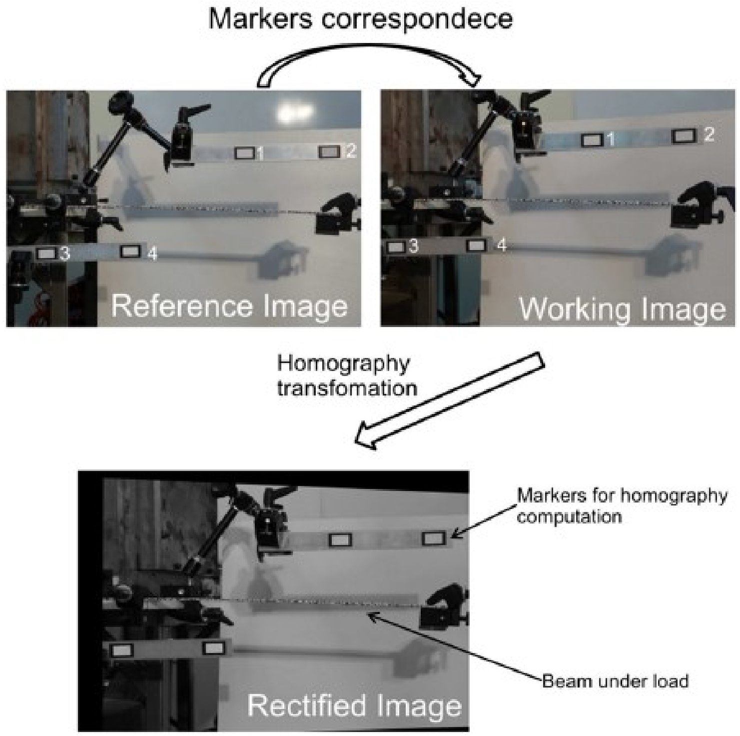

Figure 2.32: Image rectification with homography mapping (Dworakowski et al., 2016)

<u>The creation of subsets</u>

The size of subsets is critical for the accuracy of measured displacements, and for a given speckle pattern, an optimal subset size can be selected (Lecompte et al., 2006; Pan et al., 2008). The size of a subset should be large enough that it can be differentiated from other subsets from its distinctive intensity pattern, but on the other hand, enlarging the subset size normally leads to larger errors in the measured deformations. Thus, Pan et al. (2008) proposed an algorithm capable of detecting the proper subset size for a given speckle pattern.

Lee et al. (2012) demonstrated that for measuring strains, creating several pairs of subsets and averaging their strain readings can increase measurement accuracy. Furthermore, arranging the subset pairs in a circle and averaging the strain using an approach based on the Mohr's circle enabled accurate measurements of shear strains and eliminated errors induced by the principal strain directions not being perfectly aligned with the image's axes. Also, increasing the gauge length (i.e., the distance between subsets) can reduce the relative strain measurement error, but when variations across the strain field need to be considered (e.g., when surface cracks are present), the subset meshes should be sized and positioned accordingly.

2.3.6 Summary

DIC techniques are versatile, enabling full-field displacement measurements of the load response of structures, individual structural members (e.g. bridge or beam deflections), and local areas of concern (e.g., shear crack). They have been widely used in laboratory environments due to their numerous advantages. In recent years, the technology has been transferred to outdoor SHM applications, but image acquisition in exterior environments subjects the measurements to more error sources. Researchers have been proposing solutions to mitigate various types of errors. One area which has not been investigated in depth is the application of DIC techniques to follow the gradual evolution of overloading and degradation signs such as cracks, permanent deflection, settlement, expansions, creep, etc. The environmental conditions and the camera position and orientation relative to the inspected surface inevitably change between periodic inspections, which leads to measurement inaccuracy. To remove perspective distortions due to camera movement, image registration methods have been used.

2.4 Research significance

2.4.1 Impact of ASR on aggregate interlock

It has been demonstrated that aggregate interlock is one of the most important contributors to shear resistance of sound concrete, but its contribution to shear resistance in ASR-damaged members remains unclear. This is due to the simultaneous influences of chemical prestressing which closes the existing cracks and ASR microcracks within reactive aggregates which lower crack roughness.

To the knowledge of the author, the literature presents no results precisely on the effect of ASR on aggregate interlock. In their reinforced concrete push-off specimens, Sanchez et al., (2016) varied the level of expansion and the reinforcement ratio, but did not decouple the beneficial effect of chemical prestressing and the deleterious effect of ASR microcracks. The experiments of the present project aim to study the two phenomena independently and quantify their distinct impact on aggregate interlock for low to moderate levels of ASR expansion.

2.4.2 DIC for long-term structural health monitoring

Evaluations of aging concrete infrastructure generally rely on the judgment of inspectors, but as highlighted by the tragic event of De La Concorde overpass, qualitative assessment of deteriorating structures can be dangerous. There is a need to incorporate the use of reliable quantitative measurement techniques in inspections to better follow the evolution of overloading and degradation signs and defects. With the continuous improvements in the quality of digital cameras and DIC software, the DIC technique represents one viable solution with several advantages over more traditional techniques, including full-field non-contact strain and displacement measurements. However, some sources of DIC measurement errors exist, especially in the case of exterior long-term monitoring, where the environmental conditions represent a big factor, and camera positioning inevitably changes between inspections unless sophisticated and expensive equipment are used, which is time-consuming. Thus, as part of this project, an attempt is made to correct the 2D-DIC measurement errors that occur due to camera movement between image captures, which represents one of the main challenges associated with the use of DIC for long-term SHM. A simple and easy-to-use approach for correcting those errors is proposed, and it is applied to the monitoring of shear crack kinematics and ASR expansion. The proposed method would enable an inspector with a handheld digital camera to supplement their visual observations with quantitative measurements of crack widths and other deformations with relative ease.

3. EFFECT OF ASR ON AGGREGATE INTERLOCK

3.1 Overview

As discussed in section 2.2, ASR causes the formation of a silica gel which expands with moisture uptake, causing internal pressure and microcracking in concrete. The expansion and damage are reduced by confinement. For example, internal reinforcing steel restrains expansion, resulting in self-equilibrating stresses in the concrete and steel. Thus, the impact of ASR on aggregate interlock is two-fold: while the microcracks in aggregates may offer an easy path for shear cracks to propagate and reduce their roughness, the chemical prestressing enhances the normal stress across the interface. In this project, a test program with sound and expanded pre-cracked reinforced concrete push-off specimens was developed with the aim of decoupling those two simultaneous phenomena and clarifying their respective influence on the aggregate interlock for low to moderate expansion levels and low levels of confinement.

3.2 Methodology

3.2.1 Shear push-off specimens

The test program was comprised of eight pre-cracked shear push-off specimens with dimensions of 670 mm x 400 mm x 120 mm (Figure 3.1). Four different expansion levels were considered: 0.00%, 0.04% (low), 0.07% and 0.12% (moderate). For each expansion level, two specimens were fabricated: one with internal reinforcement and the other with external reinforcement. The four internally reinforced specimens were used to evaluate the simultaneous effect of the two coupled ASR-induced phenomena on aggregate interlock, while the four externally reinforced specimens were designed to isolate the effect of chemical prestressing (i.e. without internal damage in the aggregates). Except for the case of zero expansion, the internally reinforced specimens were the ones that developed ASR during several months. The other five specimens were tested at 28 days without prior ASR development. Thus, two types of concrete mixture were used in this project: one to develop ASR and the other to control it (subsection 3.2.2). To simulate the effect of chemical prestressing, the specimens with external reinforcement were subjected to mechanical prestressing just before pre-cracking and testing them. The details of all the specimens are summarized in Table 3.1 and Figure 3.1.

Table 3.1: Pre-cracked shear push-off specimens test program

ID	ρ	Reinforcement across the shear plane	Concrete mix type	ε_{ASR}	Mechanical prestressing strain
00I	0.487%	Internal	Non-reactive	0.00%	0.00%
04I			Reactive	0.04%	
07I			Reactive	0.07%	
012I			Reactive	0.12%	
00E		External	Non-reactive	0.00%	0.005%*
04E					0.04%
07E					0.07%
012E					0.12%

*00E is the control specimen for the zero-expansion case but was slightly prestressed with a tensile strain of 0.005% to ensure that the prestressing apparatus stayed in place and did not fall during the test.

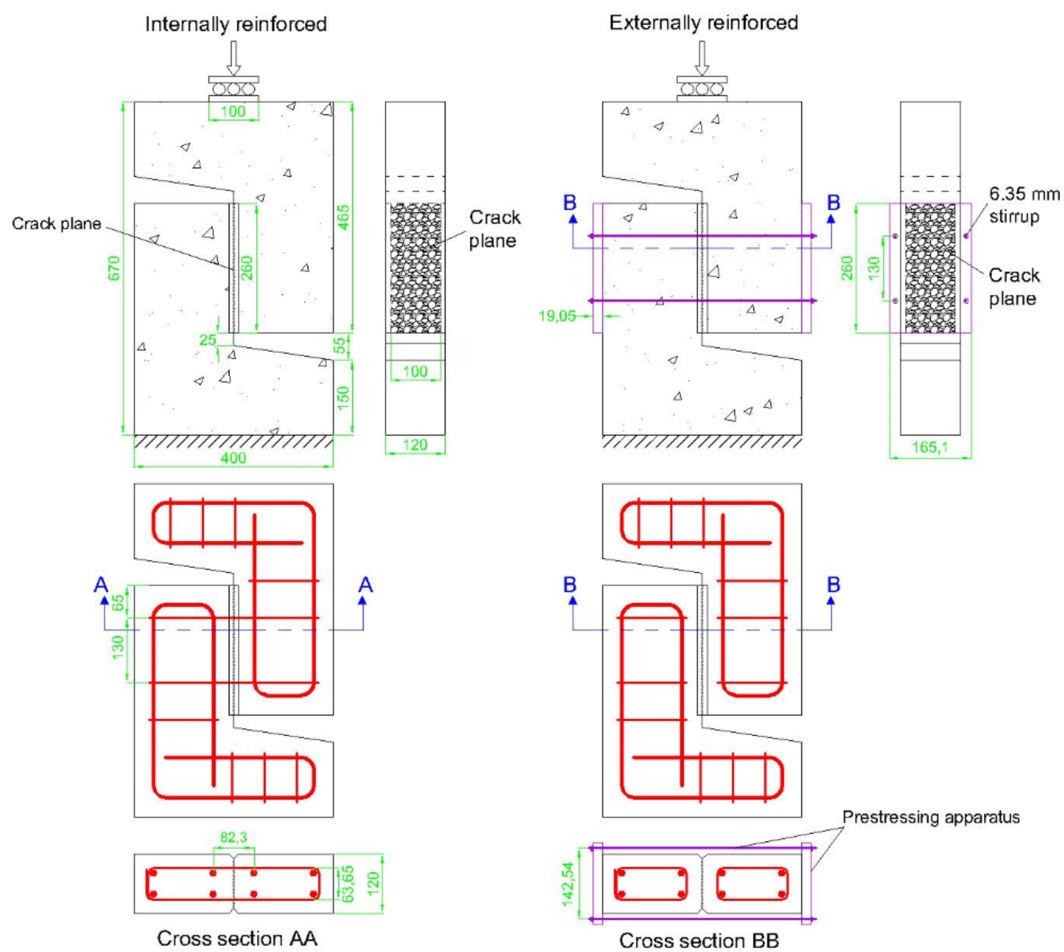

Figure 3.1: Layout of internally and externally reinforced push-off specimens (all dimensions in mm).

As seen from Table 3.1, the specimens are labeled with an identifying code. The first two digits correspond to the level of mechanical or chemical prestressing induced across the shear plane (e.g. 04 = 0.04% tensile strain in the stirrups), and the following letter indicates whether the stirrups were internal or external (I = Internal, E = External). The reinforcement ratio of 0.487% corresponds to two steel stirrups for a total of four 6.35 mm legs crossing the 260 x 100 mm shear plane perpendicularly (Figure 3.1). This relatively small amount of reinforcement was selected to ensure that the ASR expansion rate would be high enough for time constraints and for the highest expansion target (i.e. 0.12%) to be reachable. The rest of the reinforcing cage is meant to prevent any flexural cracking in the two L-shaped parts and limit movement to the shear plane.

In order to reduce dowel action from the steel reinforcement in the internally reinforced test specimens, the 6.35 mm steel bars were passed through circular PVC tubes with a length of 120 mm (Figure 3.2), disrupting their bond with the concrete. The tubes were positioned at the middle of the specimen, where the legs of the stirrups crossed the shear plane. This bond disruption distributed the bending and shearing of the bars over an increased length. In order to limit the influence of the tubes on the results, a small tube diameter was selected (12.7 mm). Yet, the hole diameter, 9.5 mm, was large enough to fit a 6.35 mm bar with an attached strain gauge and connected wires. To prevent movement of the tubes and prevent cement paste from entering during fabrication, their ends were taped to the steel bars, sealing the end holes. Thus, the total unbonded length of the internal stirrups was approximately 130 mm.

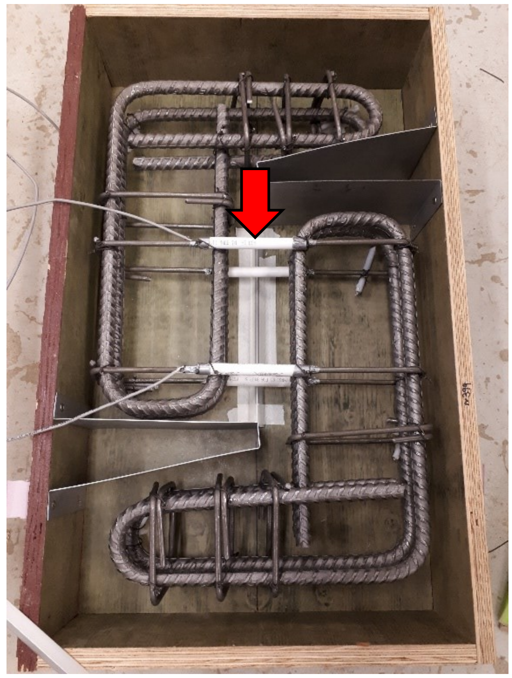

Figure 3.2: Reinforcement cage with PVC tubes installed on the legs of the stirrups

Although dowel action mitigation was the primary reason for adding the PVC tubes, they were also used to:

1. prevent a local reduction of ASR expansion in the close vicinity of the stirrups, and therefore, obtain a more uniform tensile strain distribution across the shear plane area;
2. reduce the curvature of the bars at the strain gauge locations, allowing the strain gauge to primarily measure the tensile strain of the stirrups induced by crack dilation and reduce the normal strains due to bending;
3. protect the strain gauges from the dowel forces (i.e., pressure) during the load test;
4. and increase the unbonded length of the stirrups, making it more similar to that of the externally reinforced push-off specimens.

3.2.2 Concrete mix details

The two concrete mixtures used in this program were basically the same, except for the use of two ingredients, sodium hydroxide (NaOH) and a lithium-based admixture, which were used to develop and control ASR development, respectively (Table 3.2). NaOH pellets were dissolved in the mix water of the reactive mixture to raise the total alkali content of the cement (in mass) and concrete to 1.25% Na_2O_{eq} and 5.25 kg/m^3, respectively. This accelerated ASR-induced development and generated the desired expansions in a reasonable amount of time. In the case of the control non-reactive mix, NaOH was replaced by a 30%-solid lithium nitrate ($LiNO_3$) solution, at a dosage corresponding to 125% of the "standard dosage" recommended by the manufacturer. For all specimens, a cement content of 420 kg/m^3 was selected in accordance with the requirements of ASTM C 1293-05. A general use Portland cement (equivalent with ASTM Type I) with an alkali content of 0.94% Na_2O_{eq} was used. Springhill greywacke, a highly reactive coarse aggregate (ASTM C 1260 accelerated mortar bar expansion of 0.463% at 14 days in a 1M NaOH solution, according to Grattan-Bellew et al. (2003)), was selected. Before its use, it was sieved in order to obtain particles of size varying between 4.75 and 19 mm, with equal proportions of particles of size between 4.75 to 9.5 mm, 9.5 to 12.5 mm, and 12.5 to 19 mm (i.e. ≈ 33% each). As seen from Figure 3.3, the Springhill aggregate displays an angular, flaky and elongated shape with a rough texture. A natural non-reactive sand with a fineness modulus of 2.8 was used in the concrete mixtures. An effective water-to-cement ratio of 0.44 was selected, which corresponds to a theoretical compressive strength of about 35.0 MPa according to Abrams' law.

Table 3.2: Concrete mix designs for the reactive and non-reactive specimens

Type of mixture	Cement (kg/m^3)	Fine aggregate (SSD) (kg/m^3)	Coarse aggregate (SSD) (kg/m^3)	Hydration water (kg/m^3)	Water-to-cement ratio	$LiNO_3$ added (L/m^3)	NaOH added (Kg/m^3)	Alkali content (Kg/m^3)
Reactive	420	746	1007	185	0.44	-	1.659	5.25
Non-reactive	420	746	1007	185	0.44	12.36	-	3.965

Figure 3.3: Coarse and fine aggregates used in the concrete mixtures

Companion concrete cylinders (100 by 200 mm) were cast with each push-off specimen. Cylinders were used to obtain either the compressive strength or the direct shear strength of the concrete using the same test setup as per De Souza et al. (2019). The non-reactive companion concrete cylinders were tested on the same day as the push-off specimens, but the reactive cylinders were tested when they reached their target expansion.

3.2.3 Steel properties

Tensile tests were conducted with the steel stirrups to determine their stress-strain relationship and later calculate the induced tensile stress from the measured strain. In this project, tensile stresses were caused by chemical/mechanical prestressing and by crack dilation during the tests. An idealized bi-linear curve was drawn to average the stress-strain curves produced from the tensile tests on the bars (Figure 3.4). It is defined by the bi-linear equation 3-1. The first part of the equation represents the elastic phase and the second represents the yielding phase. It can be noted that the elastic portion of the curve was defined by an elastic modulus of 200 000 MPa and that the yield strain was 0.280%, corresponding to a stress of 555 MPa.

$$\sigma\ (\text{MPa}) = \begin{cases} 200\,000\varepsilon_s & (\varepsilon_s < 0.28\%) \\ 1150(\varepsilon_s - 0.28\%) + 555 & (\varepsilon_s \geq 0.28\%) \end{cases} \tag{3-1}$$

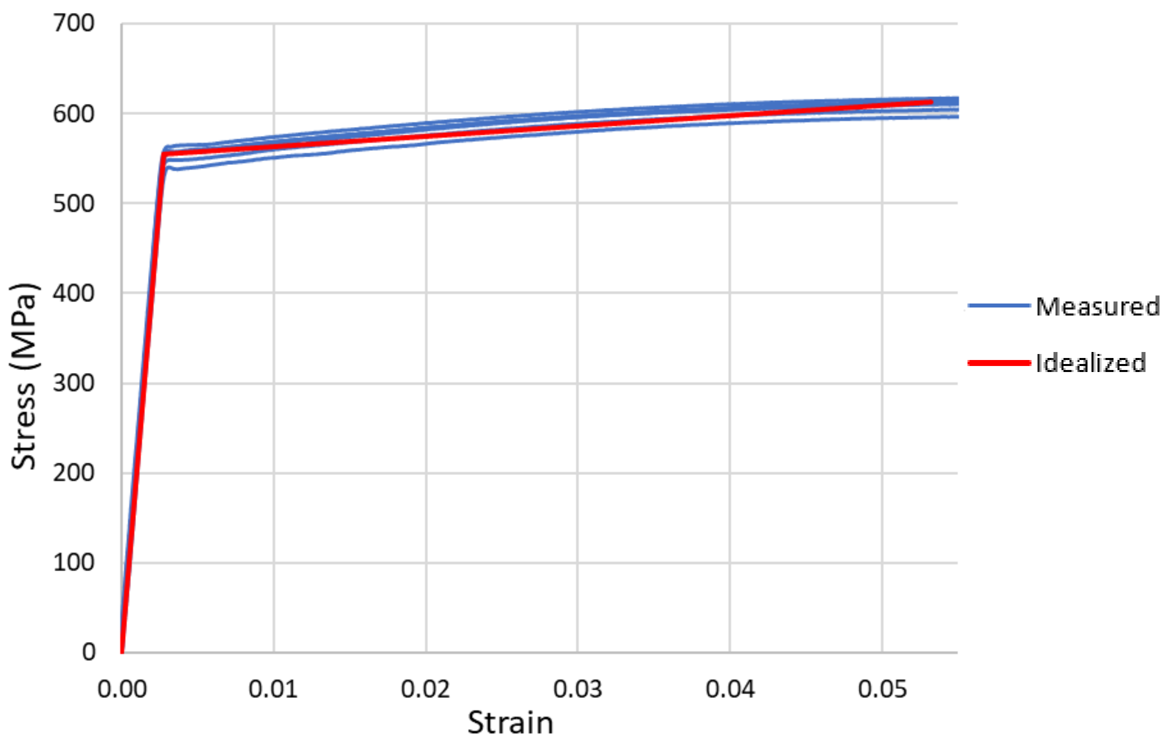

Figure 3.4: Idealized tensile stress-strain curve of the stirrups

From the idealized bi-linear curve, the induced tensile stresses in the stirrups were calculated using measured strain values, and from these values and the reinforcement ratio ρ, the resulting average concrete compressive stress over the shear plane was calculated (Table 3.3). The stresses presented in Table 3.3 are all below the maximum chemical prestressing values found in the literature for steel (Hansen, 2019; Hayes et al., 2018; Miyagawa, 2013; Swamy & Al-Asali, 1989; Wald et al., 2017) and concrete (IStructE, 1992), as per detailed under subsection 2.2.3.1. It was therefore assumed that even the highest level of expansion, i.e. 0.12%, could be reached.

Table 3.3: Chemical/mechanical prestressing stresses

Chemical/mechanical prestressing strain (%)	Prestressing stress (MPa)	
	Steel (tension)	Concrete (compression)
0.005*	10	0.049
0.04	80	0.39
0.07	140	0.68
0.12	240	1.2

*Mechanical prestressing strain induced in the stirrups of specimen 00E.

3.2.4 Fabrication, curing and conditioning of test specimens

The concrete batches were mixed using a pan mixer. The push-off specimens were manufactured one by one in horizontal wooden molds on their sides so that the shear plane was vertical. A vibrating table was used for the concrete consolidation of the specimens and their companion cylinders (Figure 3.5).

Figure 3.5: Concrete placement

After concrete placement, the push-off specimens and their companion cylinders were kept in their molds, covered, and moist cured for over two days. Then, the specimens were removed from their molds. The non-reactive concrete was moist cured at room temperature with a wet burlap under a plastic sheet for five more days, for a total curing period of 7 days. On the other hand, to accelerate the development of ASR, the reactive specimens were placed inside closed containers with high humidity (> 95%), inside an environmental chamber at 38 °C. A custom-made extruded polystyrene foam box was fabricated for the push-off specimens and used as the container (Figure 3.6). Spacers were placed at the bottom of the box to introduce a gap under the specimens. Sealed 19.05 L buckets with a grit guard insert at the bottom were used for the cylinders (Figure 3.7). To create the required RH environment in the buckets and the box, water was added at the bottom of the containers, below the specimens. With the high temperature inside the conditioning chamber, the water evaporated easily. Pieces of carpet were added to the interior faces of the buckets to absorb part of the excess condensing water and prevent excessive formation of water droplets inside the buckets and on the cylinders that could have led to significant leaching of the concrete and loss of alkalis (Figure 3.7).

Figure 3.6: Conditioning of reactive push-off specimens inside a box with high humidity (> 95%) and temperature (38 °C)

Figure 3.7: Conditioning of reactive cylinders inside 19L buckets with high humidity (> 95%) and temperature (38 °C)

3.2.5 Monitoring of ASR expansion

3.2.5.1 Push-off specimens

The ASR-induced expansion of the three push-off specimens that were placed inside the conditioning chamber was monitored with partially embedded stainless steel studs and a DEMEC digital strain gauge with an accuracy of about ±0.001 mm (Figure 3.8). Right after casting each specimen, while the concrete was still fresh, four 50.8 mm-long threaded bolts were inserted on the top surface, forming two pairs of studs. Each bolt had a small indentation at the center of their head to insert one of the two conical points of the DEMEC strain gauge. The studs were positioned such that the measured expansion corresponded to the central core of the push-off specimens in the direction perpendicular to the shear plane (Figure 3.9). Indeed, the studs were placed between the two stirrups and inserted deep enough to reach the interior of the steel cage formed with the stirrups. They were also placed close to the stirrups (i.e., 10 mm away from their center) and thus, the measured concrete expansion was restrained by the reinforcement. Therefore, the expansion was assumed to be equal to the tensile strain in the reinforcement. The distance between the studs in each pair, i.e., the gauge length, was 200 mm.

The measurements with the DEMEC strain gauge were taken on vertical concrete surfaces, and therefore, while holding the instrument, a certain pressure had to be applied to it in order for the conical points to remain in the indentations of the studs. Variation of this pressure led to some variability in the measurements. Another source of measurement error came from the instrument calibration phase using a metal bar of fixed length, since the application of a pressure on the tare button of the digital device would slightly change the readings. Thus, to increase the measurement accuracy, every measurement was taken ten times and the average expansion was used.

Strain gauges glued to the steel stirrups in their longitudinal direction were also used as a secondary measuring technique for comparison. The strain gauges were located at the middle of the bars, where they cross the shear plane, and connected to a portable strain indicator with wires (Figure 3.10). Expansion measurements with the studs and strain gauges were taken regularly over several months until the push-off specimens reached the desired expansion levels, as obtained from the average of the two stud pairs measurements.

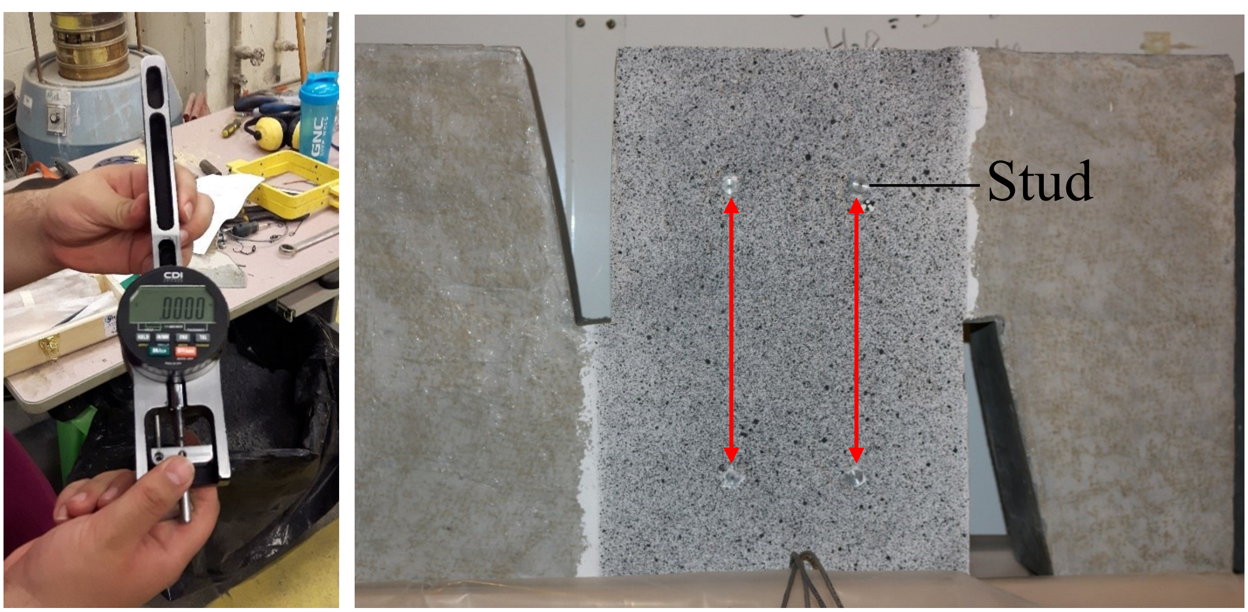

Figure 3.8: DEMEC digital strain gauge (left) and partially embedded studs for ASR expansion measurement (right)

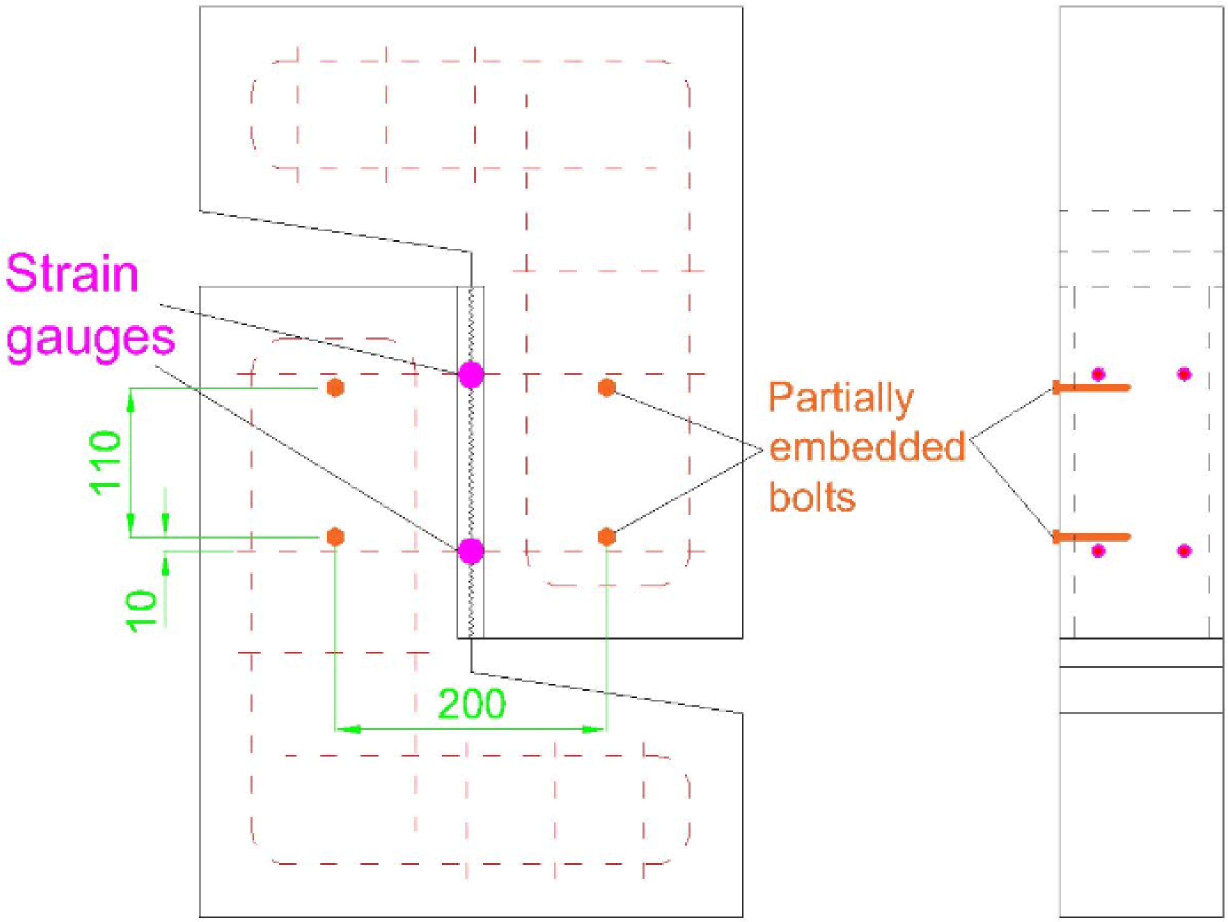

Figure 3.9: Location of studs and strain gauges for the measurement of ASR expansion

Figure 3.10: Strain gauge manual readings

3.2.5.2 Companion cylinders

The ASR-induced expansion of the reactive companion cylinders was measured in their axial direction, with a digital micrometer (Figure 3.11) and a pair of studs inserted at the center of the bottom and top circular surfaces. These studs consisted of small 10 mm-long screws. For the first three weeks of the conditioning period, expansion measurements were taken every four days, and later, the measurements were taken every two to four weeks. When the specimens reached the desired expansion percentage after a few months, they were removed from the conditioning chamber.

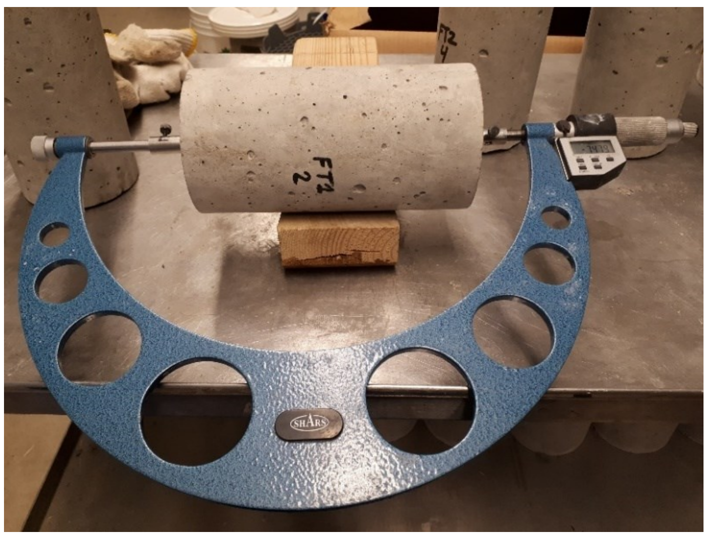

Figure 3.11: Cylinder axial expansion measurement with a concrete micrometer

3.2.5.3 Prestressing apparatus

The external prestressing apparatus consisted of two steel plates with a thickness of 19.05 mm placed on each side of the test specimens and connected by four 6.35 mm steel bars passing through them (Figure 3.12). The external bars crossed the shear plane perpendicularly, at the same height as those in the internally reinforced specimens. They were threaded at their ends so that nuts could be inserted at each end and tightened using a wrench, putting the bars under tension, pressing the plates against the specimen, and creating a normal compressive stress on the shear plane. The unrestrained length of the external stirrups was 438 mm.

Figure 3.12: External prestressing apparatus

3.2.6 Test setup, instrumentation and procedure

After reaching their target expansion, the reactive push-off specimens and the companion cylinders were removed from the conditioning chamber and cooled for one day before being tested. As mentioned before, the non-reactive push-off specimens and their companion cylinders were tested after 28 days.

3.2.6.1 Companion cylinders

<u>Standard compressive test</u>

Prior to testing the cylinders under compression, the loading faces of the specimens were ground flat to ensure better contact between the concrete surface and the loading platens of the testing frame. In the case of the reactive cylinders, the screws used for the expansion measurements were removed and a rapid set mortar mix was added in the remaining small hole. A day after, the end surfaces were ground, and the test was conducted. From the compressive test was retrieved the ultimate compressive strength of the concrete.

Direct shear test

Prior to testing the cylinders under pure shear, a notch with a depth of 25.4 mm and a width of 5 mm was made all around their circumference at the center of their height using a table saw. For the test, as seen from Figure 3.13, the specimens were positioned horizontally between two plates, and then loaded perpendicularly to their main axis with reversed supports such that a brittle shear failure occurred at the notch, splitting the specimen in two halves. From the direct shear test was retrieved the ultimate shear strength of the concrete.

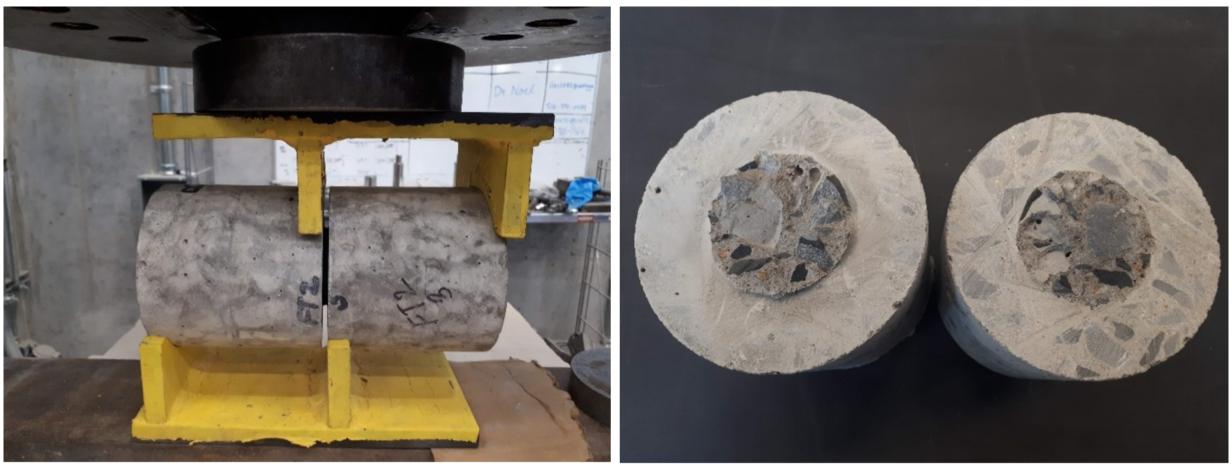

Figure 3.13: Direct shear test with concrete cylinders

3.2.6.2 Shear push-off specimens

All push-off specimens were pre-cracked and tested in a universal hydraulic testing machine, and all measurements were collected by a data acquisition system and processed by a computer. Just before being pre-cracked, the externally reinforced push-off specimens were mechanically prestressed with the apparatus and the procedure described under subsection 0. This was achieved while monitoring the strain in the external stirrups with the strain gauges glued onto them. For example, for specimen 12E, the nuts were tightened against the plates until all four strain gauge readings showed a strain of 0.12% +- 0.005%.

Pre-cracking phase

In order to pre-crack the push-off specimens, they were initially positioned horizontally in the testing machine as seen in Figure 3.14. Then, line loads were applied to opposite faces (i.e., front and rear) of the specimen at the location of the shear plane, along the two notches, to generate a splitting tensile force. Two triangular steel prisms (Figure 3.15) were used to transfer the loads to

6.35 mm diameter steel bars placed inside the notches on either side of the shear plane (i.e., front and rear). The two holes in the steel prisms enabled external stirrups to pass through.

The loads were gradually increased until a crack formed in the shear plane. With the test setup used, it was not possible to directly control the crack width. The crack width was measured using four cable transducers installed on the front and rear faces of the push-off specimens (Figure 3.14), and the stirrup strain was monitored using strain gauges. The location of all the strain gauges and linear cable transducers on the push-off specimens can be visualized on Figure 3.16.

Figure 3.14: Pre-cracking phase before testing: internally reinforced specimen (left) and externally reinforced (right)

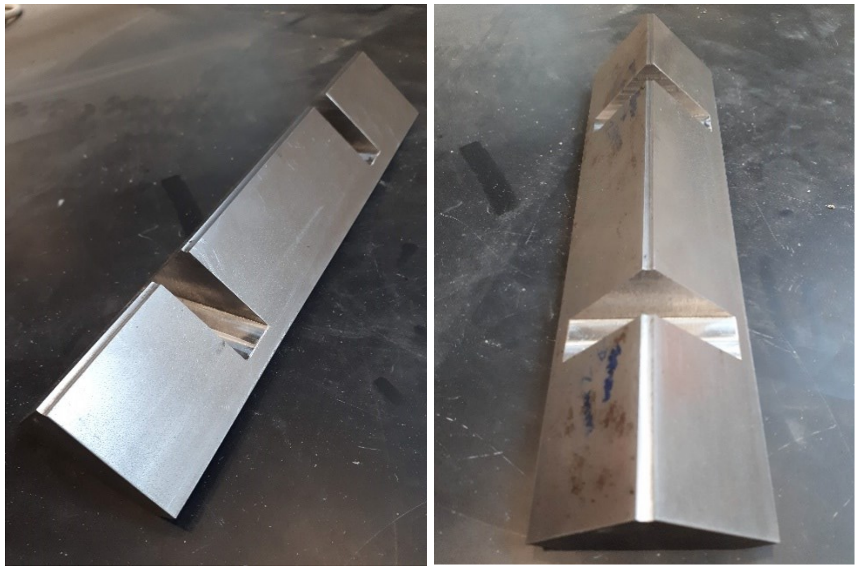

Figure 3.15: Triangular steel prisms used as knives to apply a linear load

Shear push-off test

After pre-cracking the specimens, the shear test was performed in the same testing machine. The test specimens were carefully rotated to an upward position as seen in Figure 3.17. The strain gauges and linear cable transducers remained connected to the data acquisition system to record any changes in the initial test readings (i.e., normal stress and crack width and slip).

During the shear push-off tests, the specimens were loaded concentrically. To ensure that the resultant force at the top of the specimen remained vertically oriented, it was transferred through three steel rollers. The cross head of the testing machine was lowered under displacement control at a constant speed of 1 mm/min, but the test was manually paused several times for capturing a series of photos as part of the second component of the research project (Chapter 4). The tests were paused at shear displacement (i.e., crack slip) increments of 0.1 mm for the first 2 mm, and then every 0.2 mm until a total crack slip of 4 mm was reached, marking the end of the loading test.

The applied load during the test was recorded with a load cell above the rollers. This measurement was divided by the area of the shear plane to obtain the shear stress (τ) across the crack. The normal compressive stress (σ) was found by summing together the tensile force in each stirrup based on the strain gauge readings (Equation 3-1), and dividing the total force by the shear plane area. For specimens 04I and 07I, a tensile strain of 0.04% and 0.07% was added to all strain gauge measurements to account for chemical prestressing. The crack width (w) was measured using four horizontal linear cable transducers, and slip (Δ) was measured using two vertical cable transducers (Figure 3.16).

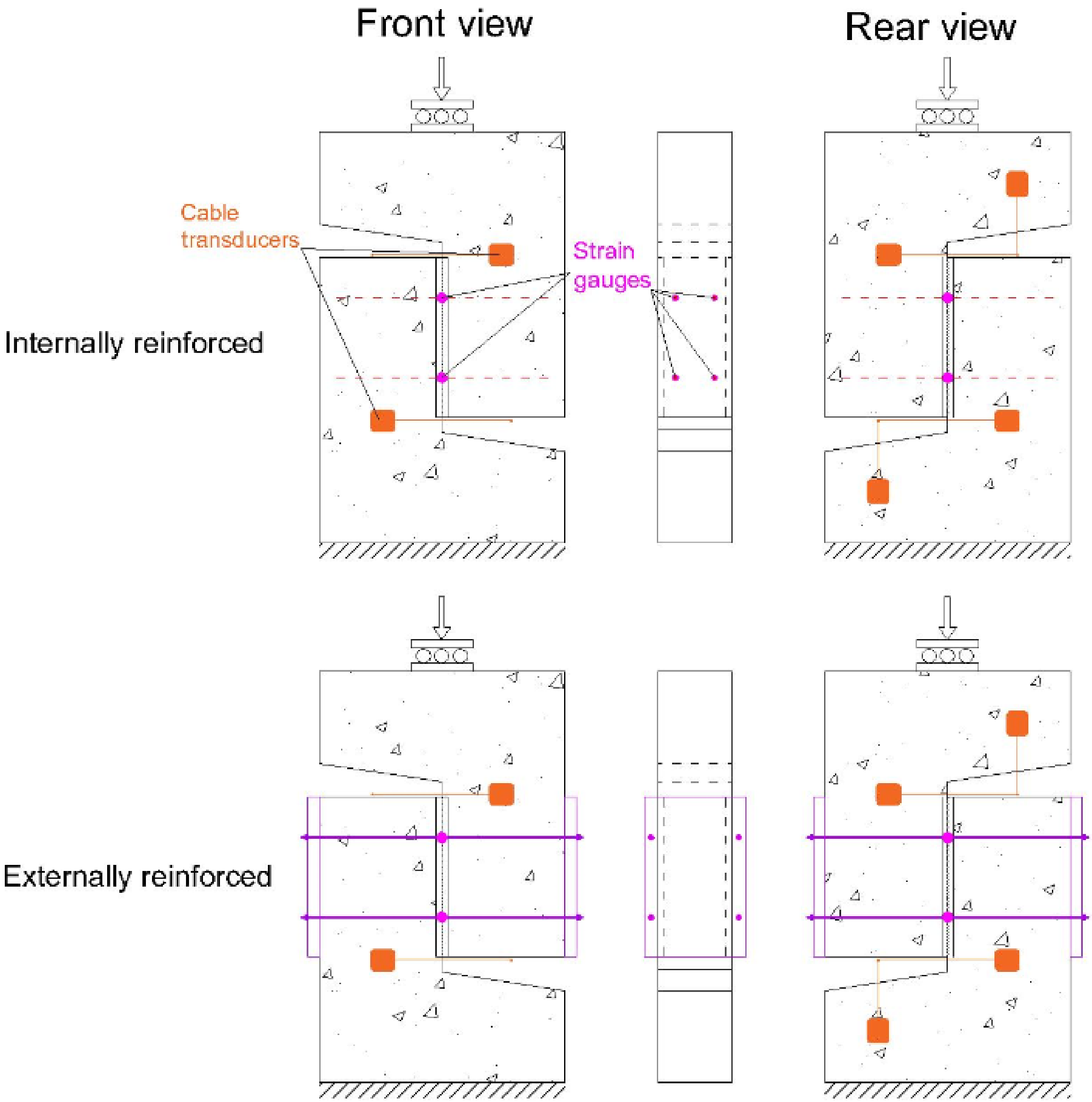

Figure 3.16: Location of linear cable transducers and strain gauges

Figure 3.17: Internally reinforced (top) and externally reinforced (bottom) push-off specimens in the hydraulic testing machine: front view (left) and rear view (right)

3.3 Results and discussion

3.3.1 ASR expansion measurements

3.3.1.1 Push-off specimens

Unfortunately, due to time constraints, the highest target expansion, i.e., 0.12%, could not be reached with specimen 12I. Thus, seven push-off specimens were tested instead of eight. The expansion measurements with the studs and the strain gauges can be seen in Figure 3.18 and Figure 3.19 respectively. Note that the strain gauge measurements represent averages of the different values read for a single specimen. Unfortunately, the small holes at the end surface of the studs of specimen 07I were not adequate, not allowing to position the pins of the DEMEC strain gauge precisely at the same location for every measurement. Thus, the expansion measurements for 07I were not reliable, and are not included in Figure 3.18. It should be noted that the specimen was removed from the environmental chamber after 47 weeks, compared to 30 weeks for 04I.

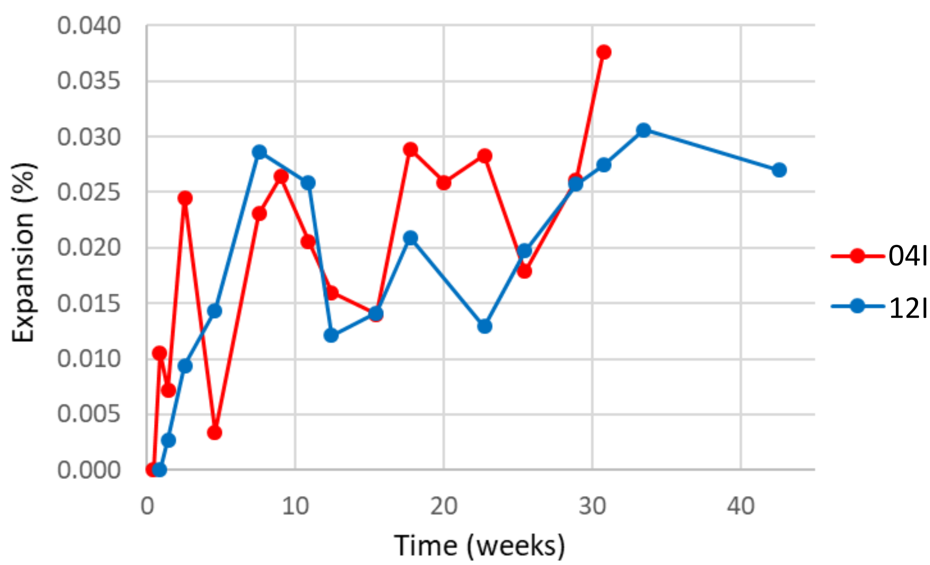

Figure 3.18: Push-off specimens expansion measurements: DEMEC strain gauge and studs

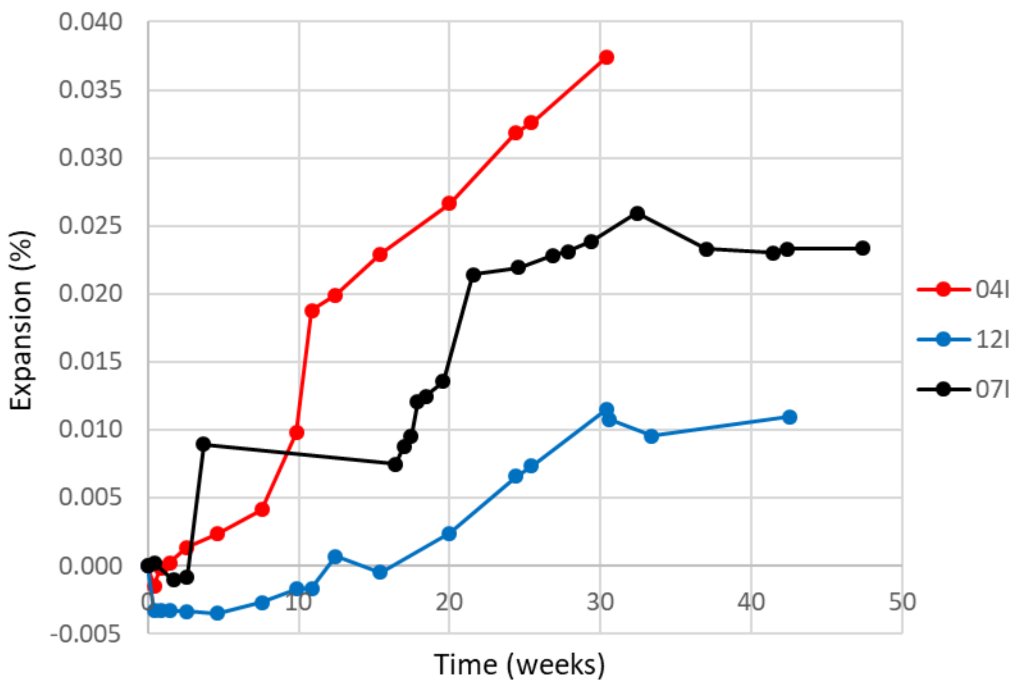

Figure 3.19: Internal reinforcement strain

Although the push-off specimens likely expanded normally, it can be seen from Figure 3.18 that the measurements made with the studs oscillated significantly. It is believed that these oscillations can be attributed to a lack of accuracy in the DEMEC strain gauge measurements, as discussed under subsection 3.2.5.1.

Although strain gauge readings were obtained for specimen 07I, past experience has suggested that long term strain measurements are not always reliable. Therefore, to estimate the expansion of specimen 07I, two cores were extracted after testing. The cores were cut in half and polished to investigate the level of damage of the concrete through a petrographic method (Figure 3.20) using a procedure called the *Damage Rating Inde*x (DRI), which was developed by Grattan-Bellew and his coworkers (Dunbar & Grattan-Bellew, 1995; Grattan-Bellew & Danay, 1992). Particular attention was paid to the direction of the cut so that the inspected surface had the same orientation as the expansion measurements discussed previously. An experienced petrographer performed the analysis and confirmed that the level of damage in the core samples was similar to that which would be expected for an expansion level of approximately 0.07%. Moreover, the petrographic analysis was repeated for the tested specimen 04I and found to be in agreement with the measured expansion values, thus validating the approach.

Figure 3.20: Coring of specimens 04I and 07I for petrographic analysis of ASR damage

3.3.1.2 Companion cylinders

Expansion measurements were taken until the companion cylinders reached the desired expansion levels and were removed from the conditioning chamber. Since the push-off specimen 12I did not reach its target expansion in time, no concrete cylinders were tested with an expansion of 0.12%, which is why half of the cylinders were removed from the chamber upon reaching an expansion of 0.04% and the others were removed at an expansion level of 0.07%. The expansion measurements are presented in Figure 3.21. The circle dots represent averages of the measurements made with all the companion cylinders still in the chamber at the time of the measurements, while the short horizontal lines represent the extremums. Although the samples were made with the same concrete mixture and put under the same environmental conditions, a significant variability in the expansion rates can be seen. Without denying the possibility that measurement errors were made with the concrete micrometer, it is known that the kinetics of the ASR chemical reaction can vary quite a lot. The companion cylinders which exhibited the fastest expansion were left in the chamber upon reaching the largest expansion target, i.e. 0.07%. Note that for the last four data points presented on Figure 3.21, some of the cylinders had been removed from the chamber because their target expansion level of 0.04% had been reached. For example, the last two data points were calculated solely from the measurements made from cylinders with 0.07% as their target expansion. This explains the small apparent increase in expansion rate towards the end of the monitoring period. Finally, it can also be noted that all the reactive companion cylinders reached their desired expansion before the push-off specimens mainly because their expansion was not confined by internal reinforcement.

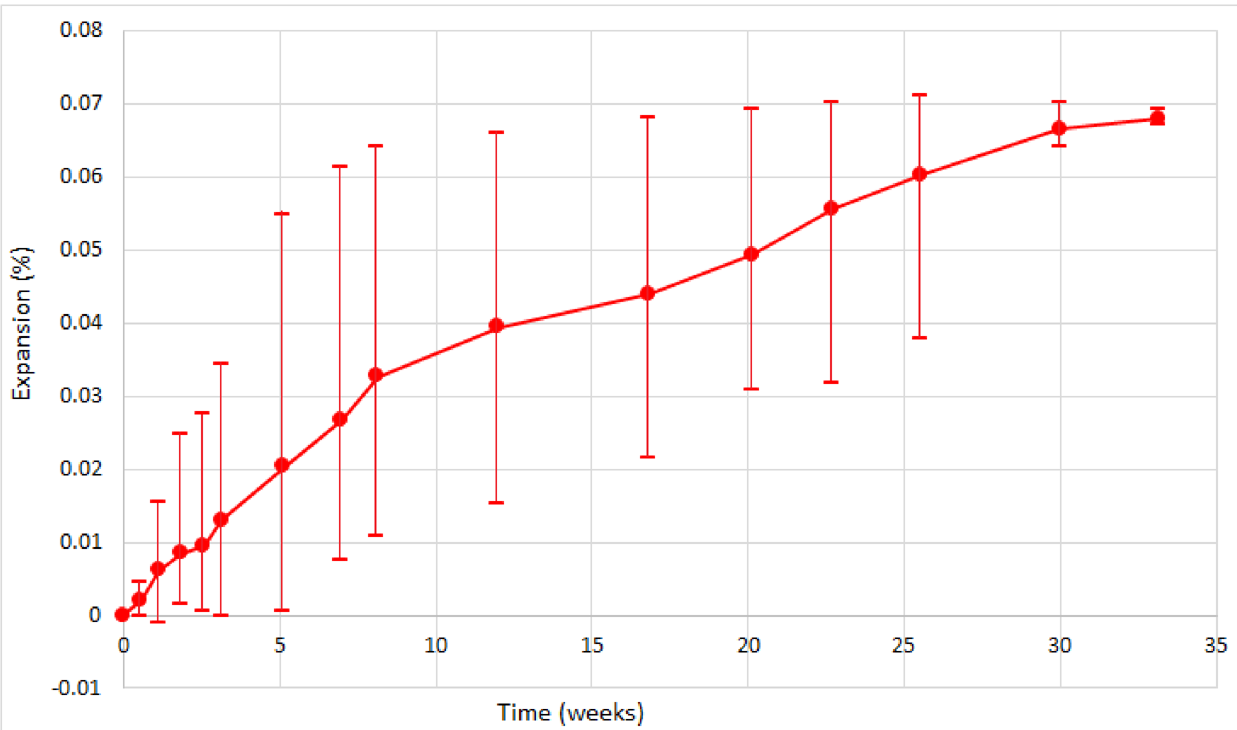

Figure 3.21: Cylinders expansion measurements

3.3.2 Companion cylinders loading test results

Five undamaged companion cylinders were tested in compression and seven were tested under direct shear. The 28-day compressive strength of the non-reactive concrete was 41.1 MPa. Among the reactive companion cylinders, nine were tested in compression at 28 days, and an average strength of 37.5 MPa was obtained. For both 0.04 and 0.07% expansion levels, two and three reactive cylinders were tested in compression and direct shear, respectively. Most of the cylinders tested under direct shear did not fail properly, since the shear crack did not propagate strictly in the reduced section (i.e., in the notch). The results from these tests were not considered. For the undamaged specimens, three specimens failed properly. For the reactive specimens, one cylinder failed properly for each expansion level. The average maximum stresses obtained from the compressive tests and direct shear tests of the companion cylinders are presented in Table 3.4.

Table 3.4: Companion cylinders average test results

Concrete type	Exp. (%)	f_c' (MPa)	Direct shear strength (MPa)
Non-reactive	0.00	42.2	4.58
Reactive	0.04	39.3	5.21
	0.07	36.7	4.16

The compressive strength of the reactive concrete was merely affected by expansions of 0.04% and 0.07%. With the absence of reinforcement (i.e., chemical prestressing), it was expected that ASR microcracks would reduce the direct shear strength of the concrete. Whereas a small reduction in shear strength of 9.2% was obtained for the companion cylinders with an expansion of 0.07%, as expected, an increase of 13.8% was obtained for the companion cylinders with an expansion of 0.04%, unexpectedly. However, since the number of successful direct shear tests was limited, these results were not conclusive. The paper by De Souza et al. (2019) may be referred to for more conclusive results obtained from the direct shear test of ASR-affected cylinder specimens. The authors obtained shear strength reductions ranging from 6 to 15% for low expansion levels (i.e. 0.05%), 12 to 30% for moderate expansion levels (0.12%), 18 to 33% for high expansions (i.e. 0.20%) and 0.22 to 0.34% for very high expansion levels (i.e. 0.30%).

3.3.3 Shear push-off tests

In this subsection, for all of the conducted push-off tests, the data obtained for the crack slip Δ vs. the crack width w, the normal stress σ vs. the crack width w, and the shear stress τ vs. the crack slip Δ is presented. The crack width and slip measurements represent averages of the measurements for the horizontal and vertical linear cable transducers respectively. The obtained crack opening paths (Δ vs. w) are first presented since they will help understand some of the observations made later with the obtained σ vs. w and τ vs. Δ relationships.

3.3.3.1 Crack opening paths

The obtained Δ vs. w curves of the seven push-off tests are presented in Figure 3.22. The pre-cracking phase resulted in different initial crack widths for each test specimen. Specimens 00I and 00E showed high initial crack widths (greater than 0.5 mm), which was expected since these specimens had negligible chemical/mechanical prestressing (i.e., normal stress acting on the shear plane prior to pre-cracking). The prestressed specimens 04E, 07E and 12E, on the other hand, showed the smallest initial crack widths (less than 0.25 mm). Surprisingly, the smallest of those initial crack widths was that of specimen 04E, which was the least prestressed. Similarly, 07I also showed a larger initial crack width than 04I despite having a larger prestressing force (although the crack started to partially close again once the shear test commenced). These discrepancies may be partially attributable to natural variability of the concrete and the lack of precise control of the crack width during the pre-cracking procedure. The results suggest that even small prestressing forces were sufficient to partially close cracks in the concrete, while modest increases in the prestressing force had little further effect on the initial crack widths.

The shapes of the Δ vs. w curves were as expected, showing an increase in crack width with shear displacement. The test specimen 07I showed a decrease in crack width of almost 0.2 mm at the very beginning of the test, which appeared unusual, but a closer look at the data confirmed that the measurements by the linear cable transducers were normal. In fact, a similar decrease in crack width was caught by the DIC measurements (Chapter 4). It is possible that the pre-cracking phase caused a slippage (and therefore a dilation) from the two crack faces which corresponded to a negative slip (and a positive crack width increment) at the beginning of the push-off test (i.e. an upward movement by the L-shaped part moving downwards while under load).

The shear cracks started dilating at different crack slips. For example, the crack of specimen 00E started opening at a crack slip as low as approximately 0.1 mm, while the cracks of the other test specimens began to widen at a crack slip varying between 0.3 and 0.6 mm.

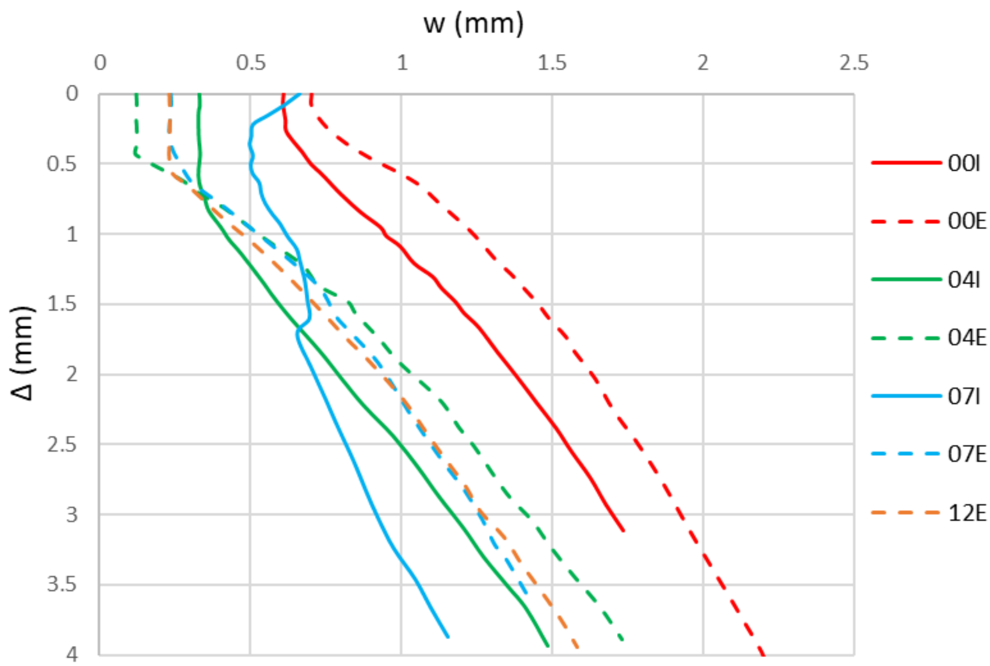

Figure 3.22: Crack slip vs. crack width

As seen from Figure 3.22, the crack opening paths were fairly similar for the different push-off specimens (i.e. roughly parallel trends). After the crack width started increasing, until the end of the test, the slope of the Δ vs. w curves either remained constant or increased very slightly. For each test specimen, the average slope of the crack opening path is presented in Table 3.5 (in bold). A larger value, corresponding to a steeper slope, indicates that shear slip occurred with relatively little crack dilation. Note that the two data points used for calculating the average slopes correspond to the initiation of crack opening, determined arbitrarily, and a crack slip of 3 mm.

The values in parentheses in Table 3.5 next to the slopes of specimens 04E, 07E and 12E represent their relative increase or decrease with respect to the slope of 00E. The slopes of the externally reinforced specimens were similar, suggesting that mechanical prestressing did not affect crack dilation behaviour. Slightly greater slopes were obtained for the specimens 07E and 012E, which were more prestressed, but 07E showed less crack dilation than 12E even though its prestressing level was lower. Even the least prestressed specimen, 00E, showed a similar increase in crack width as 12E, the most prestressed specimen. However, this may be partially attributed to the large crack width obtained from pre-cracking 00E.

The values in parentheses next to the slopes of specimens 04I and 07I represent their difference with respect to the slope of 00I. The slope of 07I was the steepest one obtained. This agrees with the original expectation that ASR microcracks in the reactive coarse aggregates would likely cause a reduction in crack roughness and thus, a smaller crack dilation during shear displacement. Chemical prestressing may have also contributed to reducing the crack dilation but, as discussed above, no significant effect was experienced due to mechanical prestressing. The crack opening path of 00I was only slightly shallower than 04I, suggesting that when the level of ASR expansion is still low, the crack roughness is not significantly affected, as expected. However, it is possible that the crack dilation of specimen 00I would have been higher if the initial crack width, i.e., 0.61 mm, was not so large.

The values in the last column of Table 3.5 represent the difference in average crack opening slope between the internally and externally reinforced specimens with equal prestressing (i.e., normal stress before pre-cracking). Since the unbonded length of the internal stirrups, i.e. 130 mm, was smaller than that of the external stirrups, i.e., 438 mm, it was expected that the crack opening paths of the internally reinforced specimens would be steeper. Indeed, a shorter unrestrained stirrup length increases its tensile stiffness (ratio of normal stress to crack width). The difference between the crack opening paths of 00I and 00E was small, was moderate for those of 04I and 04E, and was high for those of 07I and 07E. Thus, it seems that there was indeed a crack dilation reduction for the internally reinforced specimens due to their higher reinforcement tensile stiffness but considering the previously discussed effects of prestressing and ASR microcracks, the contribution of restraint stiffness was relatively small.

It may be concluded that, for an ASR expansion level of 0.07% (i.e., when the microcracks start reaching the cement paste), the reduction in crack roughness due to ASR microcracks was the parameter that increased the slope the most. Note that although this observation neglects the effect of initial crack width on the crack opening path, more investigations on this effect may be warranted.

Table 3.5: Average Δ vs.w curve slopes

Chemical/mechanical prestressing strain (%)	Average Δ vs. w curve slope (mm/mm)		
	Externally reinforced	Internally reinforced	Difference
0.00	**2.31**	**2.55**	+0.24
0.04	**1.98** (-0.33)	**2.81** (+0.26)	+0.83
0.07	**2.54** (+0.23)	**5.90** (+3.35)	+3.36
0.12	**2.36** (+0.05)	N.A	N.A

A visual observation and qualitative comparison of the roughness of the separated crack faces after the tests is presented in Figure 3.23. No clear signs of significant differences in terms of ASR damage features and crack roughness were noticed between the specimens. For all seven tested push-off specimens, regardless of ASR damage or prestressing level, it appeared that most coarse aggregate particles were split by the shear crack. (Note that the surfaces of the ASR-affected specimens are slightly discoloured making it difficult to see in Figure 3.23.) Similar observations were made with the crack faces of the companion cylinders tested under direct shear (Figure 3.24). This suggests that the tensile strength ratio between the aggregates and ITZ (proportional with f'_c) was not high enough to ensure a tortuous shear crack propagating around the coarse aggregates (which display an angular, flaky and elongated shape), even in sound concrete. While these qualitative results are somewhat unexpected, it is noted from the previous discussion that ASR damage seems to have contributed to some extent to a reduced crack roughness even though the effect was not visually obvious.

00E

00I

04E

04I

07E

07I

12E

Figure 3.23: Cracked shear planes of the push-off specimens

0.00%

0.04%

0.07%

Figure 3.24: Cracked faces of companion cylinders tested under direct shear

3.3.3.2 Normal stress vs. crack width relationships

Figure 3.25 presents σ vs. w curves for the shear push-off tests. Unfortunately, the normal stress data obtained for specimen 07I had to be omitted since the strain gauge readings were corrupted. Note that for the specimen 04I, a 0.4% strain was added to all strain gauge readings to account for ASR expansion.

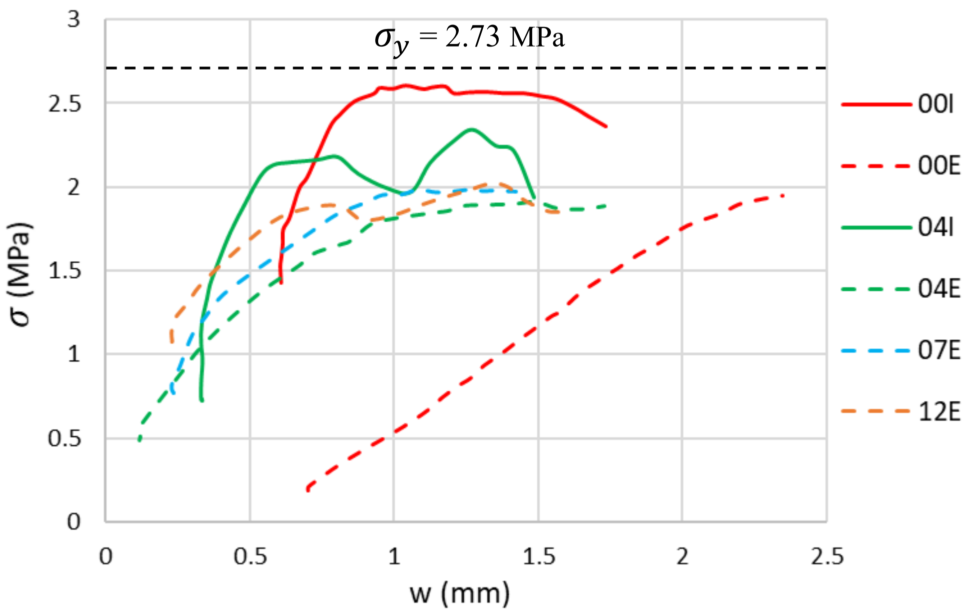

Figure 3.25: Normal stress vs. crack width

The normal stress values appear to have reached a plastic plateau where increases in crack width no longer resulted in a corresponding stress increase. However, the normal stresses never reached 2.73 MPa, which corresponds to the normal stress in the concrete if all four stirrup legs were yielding simultaneously. In fact, yield strains were only reached in the two internally reinforced specimens (due to the smaller unbonded length of the stirrups), and not by all stirrup legs (i.e., two out of four yielded simultaneously). However, as seen in Figure 3.25, in all the push-off tests the width of the shear crack exceeded the theoretical value at which the stirrups should have yielded (Table 3.6). Moreover, the data suggests that the strain gauge readings were in general lower than what they should have been according to the crack width based on theoretical calculations. For the externally reinforced specimens, the most plausible explanation for this observed response is that the external bars yielded in the threaded region at their ends (not captured by the strain gauges). For the internally reinforced specimens, possible explanations include gradual debonding of the undeformed bars, stirrup bending caused by dowel forces, pressure on the strain gauges caused by dowel forces, or strain gauge malfunctioning at high strain levels.

Table 3.6: Crack width at which the stirrups should yield

Chemical/mechanical prestressing strain (%)	Internally reinforced		Externally reinforced	
	Unrestrained stirrup length (mm)	Crack width at stirrups yield (mm)	Unrestrained stirrup length (mm)	Crack width at stirrups yield (mm)
0.00	130	0.364	438	1.23
0.04		0.312		1.05
0.07		0.273		0.920
0.12		N.A		0.701

As seen from the σ vs. w curves in Figure 3.25, since the internal reinforcement offered a higher restraint stiffness than the external reinforcement (i.e., higher steel strain increase for a given crack width enlargement), higher initial slopes were obtained for the internally reinforced specimens. In fact, very similar initial slopes were obtained within each series (i.e. internally or externally reinforced). This behaviour was expected, since the strain in the stirrups is proportional to the change in length (crack width) and inversely proportional to the unrestrained length.

The measured maximum normal stresses were higher for the internally reinforced specimens than the externally reinforced specimens, which is believed to be due to yielding of the external stirrups in the threaded end regions. The maximum normal stress was higher for specimen 00I than 04I. Although the reason for this is unclear, it is possible that during loading, the internal reinforcement debonded over a higher length for 04I or that the expansion was actually greater than 0.04% (the value which had to be added to the strain gauge measurements). It is also worth nothing that both the initial normal stress and crack width were higher for the specimen 00I. For each of the externally reinforced specimens, on the other hand, similar maximum normal stresses of approximately 2 MPa were obtained.

3.3.3.3 Shear stress vs. crack slip relationships

The shape of the τ vs. Δ curves were as expected, showing a high initial slope followed by a decline in the slope before reaching a plastic plateau (Figure 3.26). Most of the specimens showed a stable or gradually decreasing shear stress beyond displacements of approximately 0.5-1.0 mm. Two specimens (i.e., 00E and 07I) presented a gradual increase in shear stress beyond this point such that the maximum shear stress was reached at the end of the test, when the crack width and slip were at their highest.

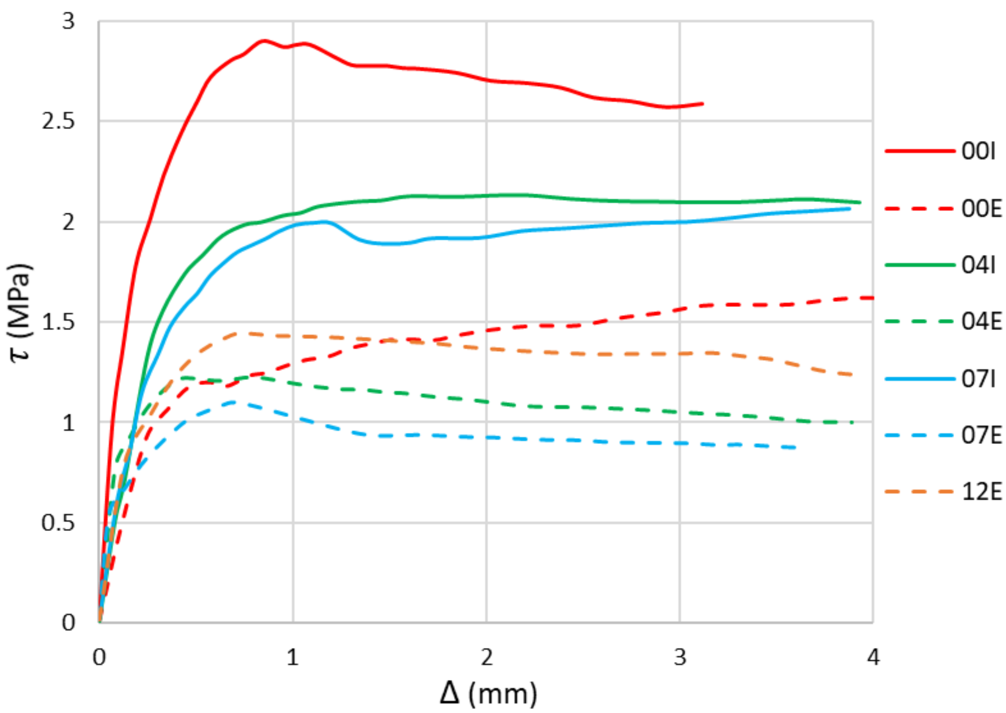

Figure 3.26: Shear stress vs. crack slip

Higher shear strengths were obtained with the internally reinforced push-off specimens compared to the externally reinforced specimens. This was expected to some extent since the reinforcement stiffness was greater for the internal bars (i.e., shorter unrestrained length), leading to increased normal stresses for a given crack width. Also, the difference could potentially be partially attributed to dowel action of the internal reinforcement, even though efforts were made to prevent it.

Comparing the τ vs. Δ curves of the internally reinforced specimens, the specimen 00I showed the highest shear stresses, followed by 04I and then by 07I. The reductions of the maximum shear strength were 26.6% and 28.6% for specimens 04I and 07I respectively. This suggests a decrease in the aggregate interlock shear transfer of reinforced concrete for increasing ASR expansion levels or, in other words, that the decrease in strength due to ASR microcracks governed over the increase in strength from chemical prestressing for the low confinement levels considered in this study. This observation suggests that the slope of the Δ-w curve (Figure 3.22) is a better indicator of aggregate interlock strength than the absolute crack width, although this trend could not be observed with the results from the externally reinforced specimens. More data would certainly help clarify this. It is also worth noting that the simplified aggregate interlock models from Gambarova & Karakoc (1983) and Li et al. (1989) use the ratio of crack slip to crack width in the shear stress equations which agrees with this point.

The decrease in shear strength for the ASR-affected specimens was more pronounced than expected. For an expansion level of 0.04%, for example, the ASR-induced cracks are still within the aggregates and have not reached the cement paste yet. Furthermore, the compressive and direct shear strengths of the reactive cylinders were merely affected by expansions of 0.04 and 0.07%, although the number of tests conducted was limited. Thus, it is likely that the results are at least partially attributable to natural variability in concrete shear strength. Further testing is therefore recommended to validate these findings.

Comparing the τ vs. Δ curves of the externally reinforced specimens, plastic plateaus ranging from about 1 to 1.5 MPa were obtained, but there was no clear trend between the shear strength and the level of prestressing. It is generally expected that an increase in the initial prestressing (i.e., normal stress) would enhance the aggregate interlock shear transfer, but this was not consistently observed. For example, even the specimen 00E, which had a negligible prestressing force, and which showed the largest crack width, showed relatively high shear stresses. These results suggest that for the relatively low levels of confinement and expansion considered in this study, the effect of chemical prestressing was negligible compared to the natural variability in the shear strength of the concrete, especially since the normal stress at the end of the test was approximately the same for each of the externally-reinforced specimens (Figure 3.25). It is important to note that increased levels of confinement and/or higher expansion levels may lead to different results.

Further observations may be made by comparing the tangent shear sliding stiffness, i.e., the initial slope of the curves (Table 3.7). First, a reduction in the initial slope was found for the externally reinforced specimens compared to the internally reinforced specimens because of their smaller reinforcement stiffness normal to the crack plane. Second, comparing the externally reinforced push-off specimens, since the clamping force from the mechanical prestressing had to be overcome to initiate crack movement, an increase in the prestressing was accompanied by an increase in the measured shear stiffness. Third and finally, comparing the internally reinforced specimens, although chemical prestressing caused a higher initial clamping force for the specimens 04I and

07I, their tangent shear stiffness was reduced by 44% compared to the sound specimen 00I. This shear stiffness reduction may be partially attributed to a reduced crack roughness due to ASR microcracks, which has reduced the required increase in crack width (and normal stress) to generate a given crack slip increment.

Finally, comparisons can be made with the onset of the inelastic plateau. For the specimens with internal reinforcement, which have shown smaller crack dilation with shear displacement, the plateau was reached at a crack slip ranging from 0.8 to 1.6 mm, whereas for the externally reinforced specimens, it was reached at a crack slip ranging from 0.4 to 0.7 mm. For the externally reinforced push-off specimens, it can be added that the plastic plateau was reached a bit earlier for specimens 00E and 04E, which have showed higher initial crack dilation with shear displacement.

The shear push-off test results are summarized in Table 3.7. Except for specimen 00E, all of the externally reinforced specimens reached their maximum shear strength at smaller crack slip and width values than the internally reinforced specimens.

Table 3.7: Maximum shear and normal stresses obtained in the push-off tests

Chemical/ Mechanical prestressing strain (%)	Internally reinforced					Externally reinforced				
	τ_{max} (MPa)	σ_{max} (MPa)	Δ at τ_{max} (mm)	w at τ_{max} (mm)	Shear stiffness* (MPa/mm)	τ_{max} (MPa)	σ_{max} (MPa)	Δ at τ_{max} (mm)	w at τ_{max} (mm)	Shear stiffness* (MPa/mm)
0.00	2.90	2.60	0.84	0.86	11.1	1.63	1.94	4.63	2.35	4.21
0.04	2.13	2.35	2.22	0.88	6.15	1.23	1.91	0.81	0.41	9.35
0.07	2.07	N.A	3.87	1.15	6.15	1.10	1.98	0.70	0.35	10.8
0.12	N.A	N.A	N.A	N.A	N.A	1.44	2.02	0.73	0.33	11.4

*The tangent shear stiffness was calculated based on what was visually assumed to be the linear elastic portion of the τ vs. Δ curves.

3.4 Analysis

In this section, the shear stress-slip relationships obtained in the push-off tests are compared with those predicted by the simplified aggregate interlock models from Walraven & Reinhardt (1981), Gambarova & Karakoc (1983), and Li et al. (1989), which were presented in subsection 2.1.5. The three shear stress equations are presented again in Table 3.8 for reference.

Table 3.8: Simplified aggregate interlock shear stress models

Walraven & Reinhardt (1981)	$\tau = -0.04f_c' + \{1.8w^{-0.80} + (0.292w^{-0.707} - 0.25) \cdot f_c'\}\Delta \qquad (\tau > 0)$
Gambarova & Karakoc (1983)	$\tau = \tau_0 \left(1 - \sqrt{\frac{2w}{D_{max}}}\right) \frac{c_1 r + c_2 r^4}{1 + c_2 r^4}$ $r = \Delta/w$ $c_1 = \frac{10}{f_c'}$ $c_2 = 2.44(1 - 16.33f_c')$
Li et al. (1989)	$\tau = 3.83 f_c'^{1/3} \frac{r}{1 + r^2}$ $r = \Delta/w$

For each push-off specimen, the obtained τ vs. Δ relationship was plotted together with three curves obtained from the above aggregate interlock models and the crack width and slip measurements (Figure 3.28). Note that all crack slip measurements used represent an average of the measurements from the two linear cable transducers oriented vertically. Since a small relative Z-axis rotation of the two crack faces (Figure 3.27) is possible and causes a crack width gradient over the height of the shear plane, it was taken into account for more accurate shear stress calculations with the three models. In order to do so, the rectangular shear plane of 260 mm by 100 mm was divided vertically, and 13 equal segments of 20 mm by 100 mm were considered. The crack widths of each segment were found by linear interpolation of the average crack widths at the top and at the bottom of the crack, and the shear stresses of the 13 segments were averaged to find the overall shear stresses.

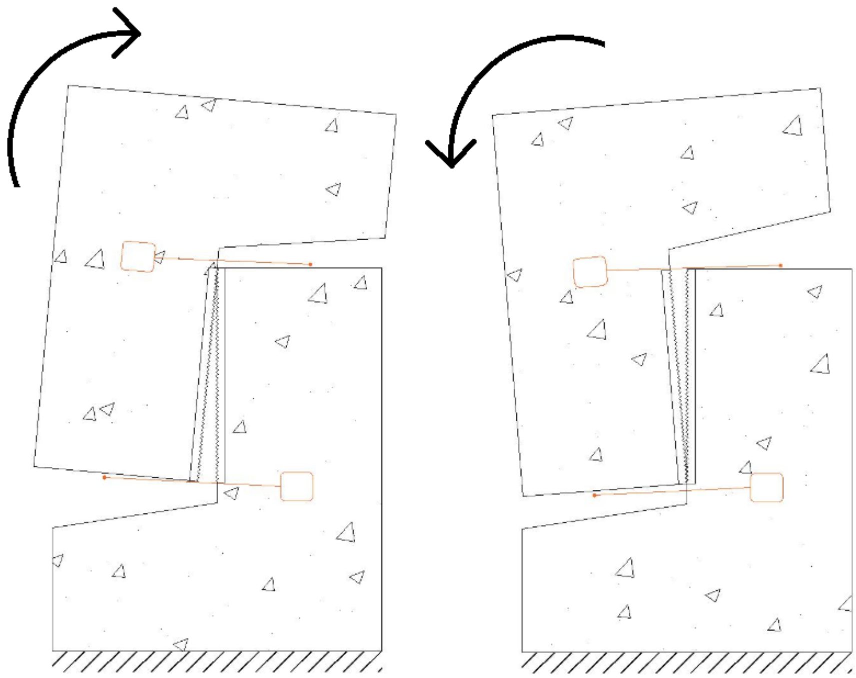

Figure 3.27: Z-axis rotation from the top part of the push-off specimen

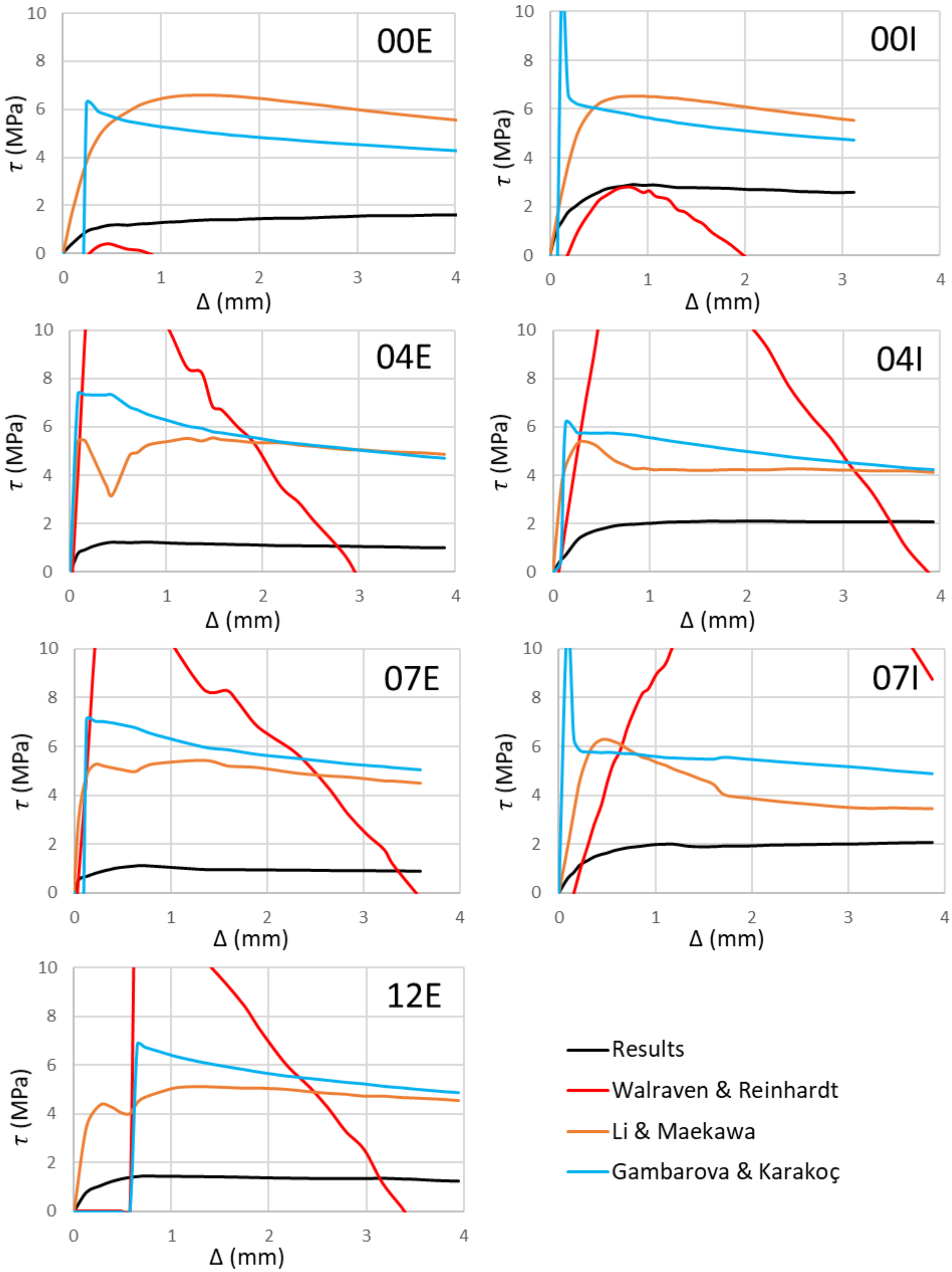

Figure 3.28: Shear-slip behaviour of push-off specimens compared with existing models

As seen from Figure 3.28, the three models produced stress-slip curves of different shapes and with large variations in values. The shape of the Li & Maekawa (1989) curves were the closest ones to those of the experimental results, but the calculated stress values were about two to five times greater than the data from the tests. In fact, with the exception of specimens 00I and 00E, which showed greater shear stresses than those predicted by the model developed by Walraven & Reinhardt (1981), the experimental shear stresses were consistently significantly smaller than those predicted with the three models from the literature. This was expected to some degree since the reinforcement restraint stiffnesses of the specimens tested in this project were relatively low. Indeed, this reduced the normal stress (and thus the shear stress) for given crack displacements, while none of the three simplified shear equations include the normal stress as a parameter. Typical reinforced concrete members are usually reinforced with embedded deformed bars (bonded over their entire length) at higher reinforcement ratios. For example, the simplified model of Walraven & Reinhardt (1981) was derived from the experimental results of heavily reinforced push-off specimens with external restraint bars presenting stiffnesses comparable to those of embedded deformed bars with reinforcement ratios ranging from 0.56% to 2.24%. For a crack width of 0.6 mm, they measured normal stresses ranging from 3.6 to 7.8 MPa. The simplified shear equation presented by Gambarova & Karakoc (1983) appropriately described some of these experimental results. In their shear tests conducted with constant crack openings of 0.1, 0.5 and 1.0 mm, Li et al. (1989) measured normal stresses reaching 4 to 5.8 MPa. All of the aforementioned normal stresses are largely above the maximum normal stresses obtained in this project, which ranged from 1.91 to 2.6 MPa. Considering this, the fact that the three models overpredicted the aggregate interlock shear strength of the push-off specimens tested in this project suggests that the equations may not be suited for lightly reinforced concrete. However, the difference in strength may also be partially related to the previous observation that, regardless of the specimen, most coarse aggregates were unexpectedly split by the shear crack resulting in a relatively smooth crack surface.

Table 3.9 presents the shear strength ratios between the experimental values and those predicted by the three models, for a crack slip of 1 mm, and for the maximum experimental shear stress. Due to their higher reinforcement restraint stiffness, higher shear stresses were obtained with the internally reinforced specimens, which is why their differences with the predicted shear stresses are smaller than the externally reinforced specimens. It can be seen that prestressing did not have a noticeable effect on the experimental to predicted shear strength ratios.

Table 3.9: Experimental to predicted shear strength ratios

Chemical/ mechanical prestressing strain (%)	Experimental to predicted shear strength ratios											
	External reinforcement						Internal reinforcement					
	At 1 mm crack slip			At peak shear stress			At 1 mm crack slip			At peak shear stress		
	W&R	L&M	G&K	W&R	L&M	G&K	W&R	L&M	G&K	W&R	L&M	G&K
0.00	N.A*	0.20	0.24	N.A*	0.31	0.39	1.09	0.44	0.51	1.04	0.44	0.50
0.04	0.12	0.22	0.19	0.11	0.23	0.19	0.14	0.44	0.37	0.23	0.50	0.44
0.07	0.09	0.20	0.17	0.09	0.21	0.16	0.22	0.37	0.36	0.24	0.60	0.42
0.12	0.12	0.28	0.23	0.09	0.31	0.21	N.A					

*The predicted shear stress value was negative and thus removed.

4. A METHOD TO CORRECT DIC MEASUREMENT ERRORS DUE TO CAMERA MOVEMENT BETWEEN PERIODIC STRUCTURAL INSPECTIONS

4.1 Overview

With the current need to supplement periodic visual inspections with quantitative measurement techniques, a method is proposed to correct 2D-DIC measurement errors associated with changes in camera positioning between multiple image captures. The correction method involves the use of four reference points in the plane of the inspected surface and in the field of view of the camera. The apparent deformations caused by camera movements are separated from the real deformations experienced by the structure by tracking the apparent movement of the reference points. The method can be applied for correcting both absolute and relative displacement measurements.

In this chapter, the different types of camera movement leading to apparent displacements and deformations will first be described. Second, the proposed measurement correction method will be explained. Third and finally, validation testing of the correction method for the 2D-DIC monitoring of ASR expansion and shear crack growth will be presented.

4.2 Types of camera movement and resulting apparent deformations

In this section, the possible types of camera movement are explained and their effect on the captured image is illustrated. Note that in the figures presented in this section, the square grid (image 1) represents a region of an undeformed inspected surface, i.e., what would appear on an image acquired by a perfectly positioned and oriented camera, and the shape consisting of dotted lines (image 2) illustrates how the same region would appear after camera movement.

4.2.1 In-plane translation

A camera shift parallel to the structure's planar surface will result in an apparent translation of the concrete surface of the same magnitude and in the opposite direction. In Figure 4.1, the inspected surface appears to have moved up and to the right as a result of the camera translation in the opposite direction. If a relative displacement such as a change in crack width is being measured, such movement will have a negligible effect on the measurement accuracy as long as the tracked facet points are found in both images. However, if an absolute displacement such as a structural member deflection is being measured, a camera shift in the measurement direction will induce an error. This error can be corrected by subtracting the apparent translation of a fixed reference point located in the plane of the inspected surface from the measurement.

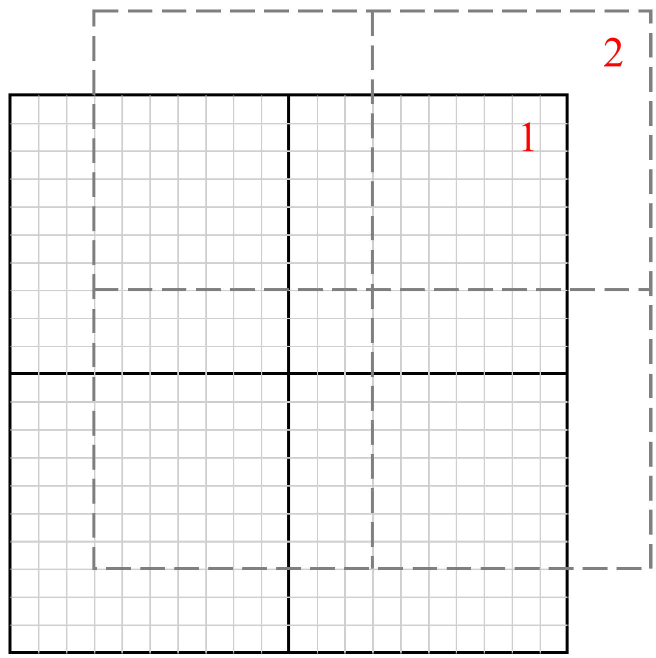

Figure 4.1: Camera shift

4.2.2 Out-of-plane translation

If the camera is moved towards or away from the structure's surface, an apparent expansion or contraction of the inspected surface in all directions will be perceived. In Figure 4.2, an expansion of the square surface, caused by a camera translation towards it, is represented. This type of error can be corrected if a reference length (or two reference points) in the plane of the inspected surface is captured in the photos. The reference length can either be the inspected element itself or an added object such as a ruler, as long as its dimension does not change between the pictures. Real deformation or displacement values can be found by multiplying the measurements by a scale correction factor determined from the reference of known length.

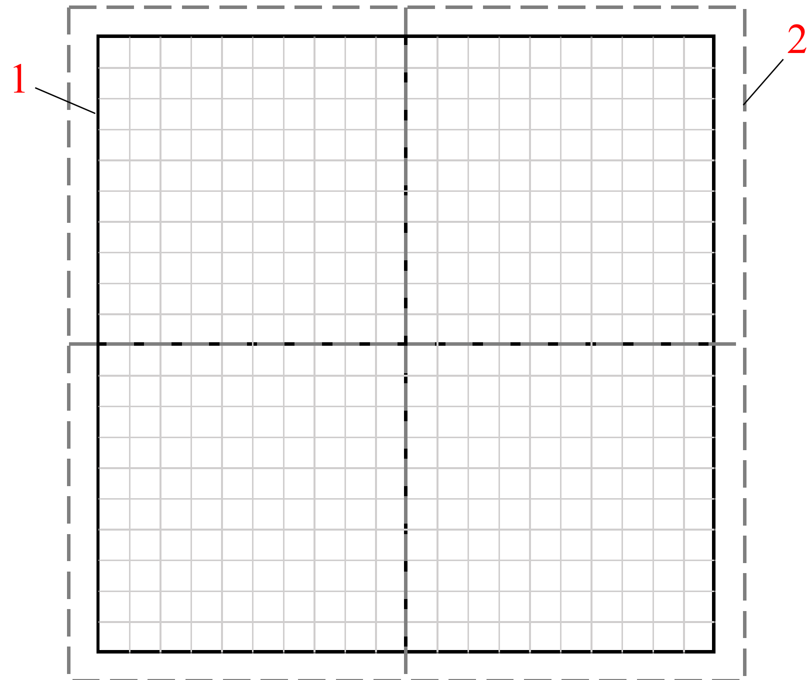

Figure 4.2: Out-of-plane camera translation

4.2.3 In-plane rotation

If the camera is rotated about an axis perpendicular to the structure's surface, the inspected surface will appear to rotate in the opposite sense. For example, if a camera is rotated clockwise, the structure will appear to have rotated counterclockwise (Figure 4.3). Similar to camera shift, in-plane camera rotation will not change the total relative distance between two facet points, but if the absolute position of a point must be defined, it will cause an error. This error can be calculated from the apparent change in orientation of a one-dimensional reference object captured in the photos (i.e. two reference points).

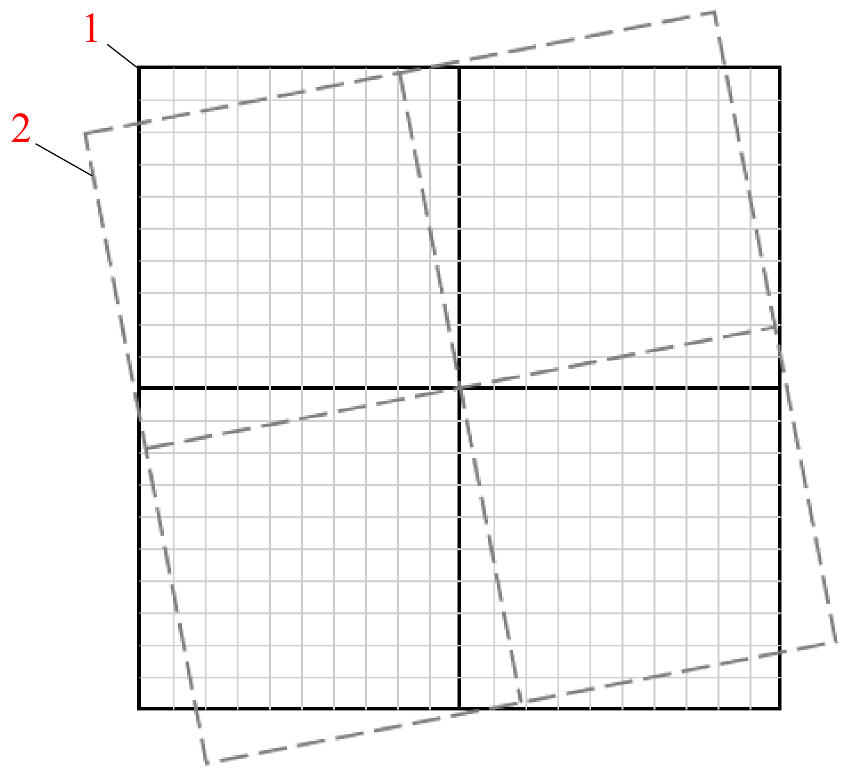

Figure 4.3: In-plane camera rotation

4.2.4 Out-of-plane rotation

Camera tilting (i.e., rotation about a horizontal axis parallel to the structure surface) will simultaneously cause an apparent linear horizontal strain gradient and contraction of the inspected surface in the vertical direction (Figure 4.4a). Similarly, camera panning (i.e., rotation about a vertical axis parallel to the structure surface) will simultaneously cause an apparent linear vertical strain gradient and contraction of the inspected surface in the horizontal direction (Figure 4.4b). Errors caused by these camera perspective changes individually can be corrected using a reference length in both the horizontal and vertical directions, in the plane of the inspected surface (i.e. three reference points). If camera panning or tilting are combined with camera in-plane rotation, it becomes impossible to decouple the contributions of the three types of rotation (i.e. about the three orthogonal axes) unless a fourth reference point is included in the plane of the structure's surface (Figure 4.5).

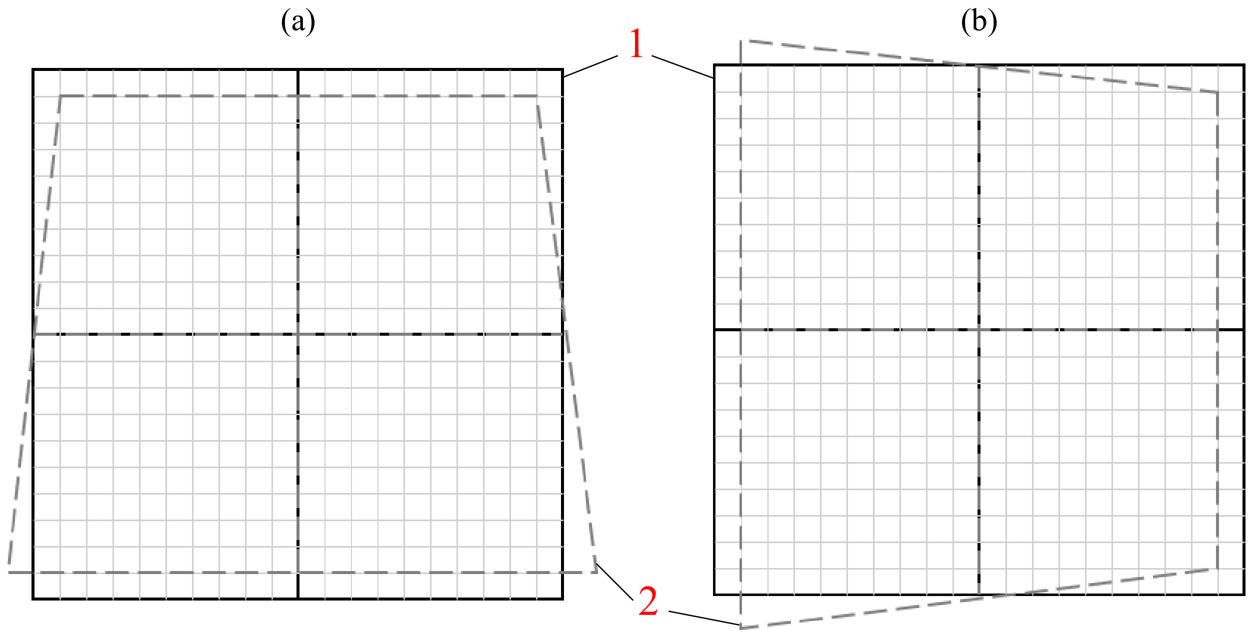

Figure 4.4: Camera tilting (a) and panning (b)

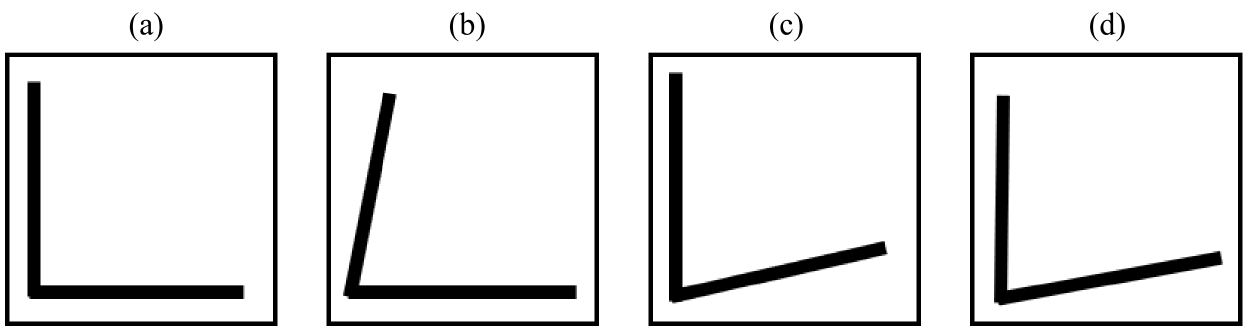

Figure 4.5: Combinations of orthogonal axes' rotations: no rotation (a), tilting about horizontal axis parallel to inspected surface (b), panning about vertical axis parallel to inspected surface (c), and combined tilting and in-plane rotation (d)

4.3 Proposed approach

This section presents a simple method to correct for 2D-DIC measurement errors associated with changes in camera positioning during multiple image captures. The method is applicable to any combination of the camera movements discussed in the previous section. It includes the use of four reference points located in the plane of the inspected surface and in the field of view of the camera. The relative horizontal and vertical distances between these points must be known. The apparent displacements of the reference points on each acquired image, as measured with the DIC technique, are used as inputs in an equation which allows to determine the real undistorted coordinates of any points of interest on the inspected structure. Using the corrected 2D coordinates of these points, their real displacement between inspections can be determined.

If an absolute displacement (e.g. permanent deflection or settlement) is measured, it is required that a fixed reference point in the plane of the inspected surface (possibly one of the four reference points of known relative distances) be captured in the photos and that its coordinates be corrected with the equation, so that its residual 2D displacement due to camera shift be subtracted from the measurements. In some applications (e.g. measurement of bridge mid-span deflection), such fixed reference points may be very difficult to have, if not impossible. If this is the case, a possible solution is to limit camera shift in the measurement direction, by mounting it on a fixed support for example.

Different ways of creating four reference points in the plane of an inspected structure's surface exist, some more practical, and some more sophisticated. For example, the reference points could be created out of natural features from the structure's surface or by inserting survey markers on the surface, although structural deformations could potentially change the relative distance between these points. The reference points could also be made on a planar object, placed on the structure's surface for each inspection capture, although measurement errors associated with out-of-plane movement (translation or rotation) and in-plane rotation of the object could occur. A more sophisticated approach would be to use an equipment capable of acquiring digital photographs while projecting four laser reference points on the structure's surface.

The equation used to correct the measured coordinates of points of interest depends on the horizontal and vertical distances between the four reference points. Positioning the reference points in a rectangle allows to obtain a simple equation. To demonstrate this, consider the two square grids with vertices A, B, C, and D in Figure 4.6, which become distorted in different ways. Vertex A represents the origin from which all coordinates are measured. The square on the left becomes distorted by an apparent displacement of the vertex C from coordinates C_0 (x_{C0}, y_{C0}) to C_1 ($x_{C0} + \Delta x_C$, $y_{C0} + \Delta y_C$). Assuming that all straight lines of the grid remain straight after distortion, it can be seen that the point E is displaced by ($\Delta x_C/2$, $\Delta y_C/2$) and that the center point F is displaced by ($\Delta x_C/4$,$\Delta y_C/4$). In a more general sense, the apparent displacement of any point can be calculated using Equations 4-1 and 4-2:

$$\Delta x = \Delta x_c \frac{x_0 y_0}{x_{C0} y_{C0}} \tag{4-1}$$

$$\Delta y = \Delta y_c \frac{x_0 y_0}{x_{C0} y_{C0}} \tag{4-2}$$

Where Δx and Δy are the apparent displacements of the point of interest, Δx_C and Δy_C are the apparent displacements of vertex C, x_0 and y_0 are the original coordinates of the point of interest, and x_{C0} and y_{C0} are the original coordinates of vertex C.

Now, for the square on the right, vertex B is also displaced from coordinates B_0 (x_{B0},y_{B0}) to B_1 ($x_{B0} - \Delta x_B$,$y_{B0} + \Delta y_B$). The cumulative apparent displacement of the center point F becomes the sum, or superposition, of the displacements associated with both vertices B and C ($\Delta x_C/4 - \Delta x_B/4$,$\Delta y_C/4 + \Delta y_B/4$). More generally, if four reference points in the plane of the inspected surface and positioned in a rectangle (i.e., A, B, C and D) are captured in the photos, the apparent horizontal and vertical displacements of any point on the surface can be calculated from Equations 4-3 and 4-4, respectively:

$$x_1 = x_0 + \frac{1}{x_{C0} y_{C0}} [\Delta x_B (x_{C0} - x_0) y_0 + \Delta x_c x_0 y_0 + \Delta x_D x_0 (y_{C0} - y_0)] \tag{4-3}$$

$$y_1 = y_0 + \frac{1}{x_{C0} y_{C0}} [\Delta y_B (x_{C0} - x_0) y_0 + \Delta y_c x_0 y_0 + \Delta y_D x_0 (y_{C0} - y_0)] \tag{4-4}$$

Where x_1 and y_1 are the post-distortion coordinates of the point of interest, Δx_B, Δx_C, Δx_D, Δy_B, Δy_C, and Δy_D are the apparent displacements of vertices B, C, and D, respectively, and all other terms are as previously defined.

A DIC analysis of photographs taken during different structural inspections will allow to obtain the apparent coordinates of the reference points and points of interest in each image. The real coordinates of vertices B, C, and D are known from their measured relative horizontal and vertical distances from vertex A. By inputting all of these coordinates in Equations 4-3 and 4-4, the undistorted coordinates of the point of interest x_0 and y_0 can be isolated, and subsequently, they can be used for calculating real displacements or strains.

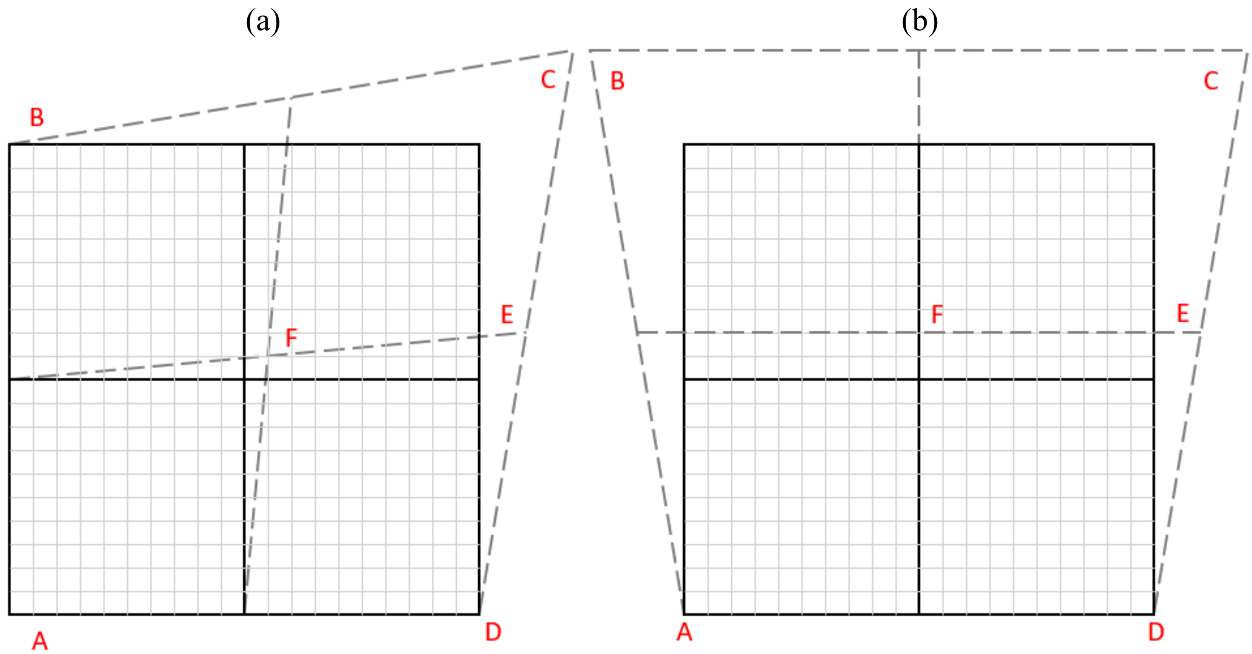

Figure 4.6: Distortion of point C (a) and points B and C (b)

4.4 Experimental validation

Equations 3.3 and 3.4 were used to correct the 2D-DIC measurement errors due to camera movement in two applications: the long-term monitoring of ASR expansion and the measurement of shear crack kinematics using the push-off specimens presented in Chapter 3. These are relative displacement measurements (i.e. strains and crack widths). The goal of this analysis was to find whether the residual error after correcting the measurements would be acceptable or not. The assumed tolerable absolute error for ASR expansion measurements was ± 0.01% since this is considered acceptable from a practical point of view. Since the gauge length used in this project was 200 mm, this error corresponds to a relative displacement measurement error of ± 0.02 mm. In the case of shear crack measurements, a tolerable error of ±0.1 mm was selected.

In this section, the methodology used to validate the correction method will be described. The technique used to obtain four reference points positioned in a rectangle and in the field of view of the camera was simple, and a handheld digital camera with normal quality was used for acquiring the images affected by camera movement. Thus, an inspection team could easily repeat the same procedure for the assessment of a real structure. Since the DIC measurements were made with the reinforced concrete specimens and load tests presented in the previous chapter, the details that were already given were intentionally omitted.

4.4.1 Image acquisition

4.4.1.1 Inspected concrete surfaces

After hardening of the concrete push-off specimens, their front face was painted with a speckle pattern (Figure 4.7). The use of a speckle pattern enabled the creation of trackable subsets (also called facet points) for DIC analysis of ASR expansion and shear crack kinematics.

Figure 4.7: Shear push-off specimen with painted speckle pattern

4.4.1.2 Rectangular aluminum template

For the experimental validation of the correction method, a rectangular aluminum template with a thickness of 3 mm was fabricated (Figure 4.8). During image acquisition, the template was placed on the inspected concrete surface using reusable adhesive putty (Figure 4.9). The speckle pattern painted on the front surface of the template enabled the creation and tracking of four subsets (reference points) during post-processing of the photos with a DIC software. As seen from Figure 4.9, the dimensions of the template's rectangular hole were large enough to view the region of interest for ASR expansion measurements and the entire shear crack during the load tests.

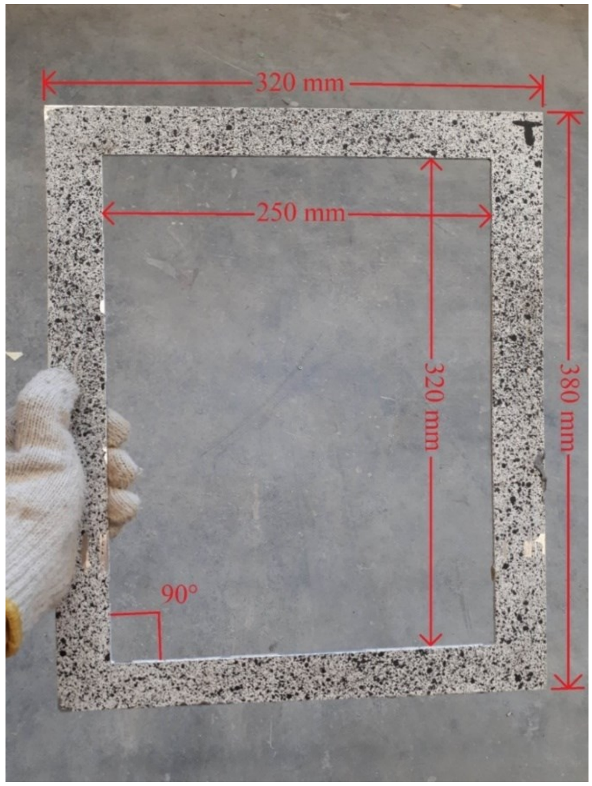

Figure 4.8: Rectangular aluminum template

(a)

(b)

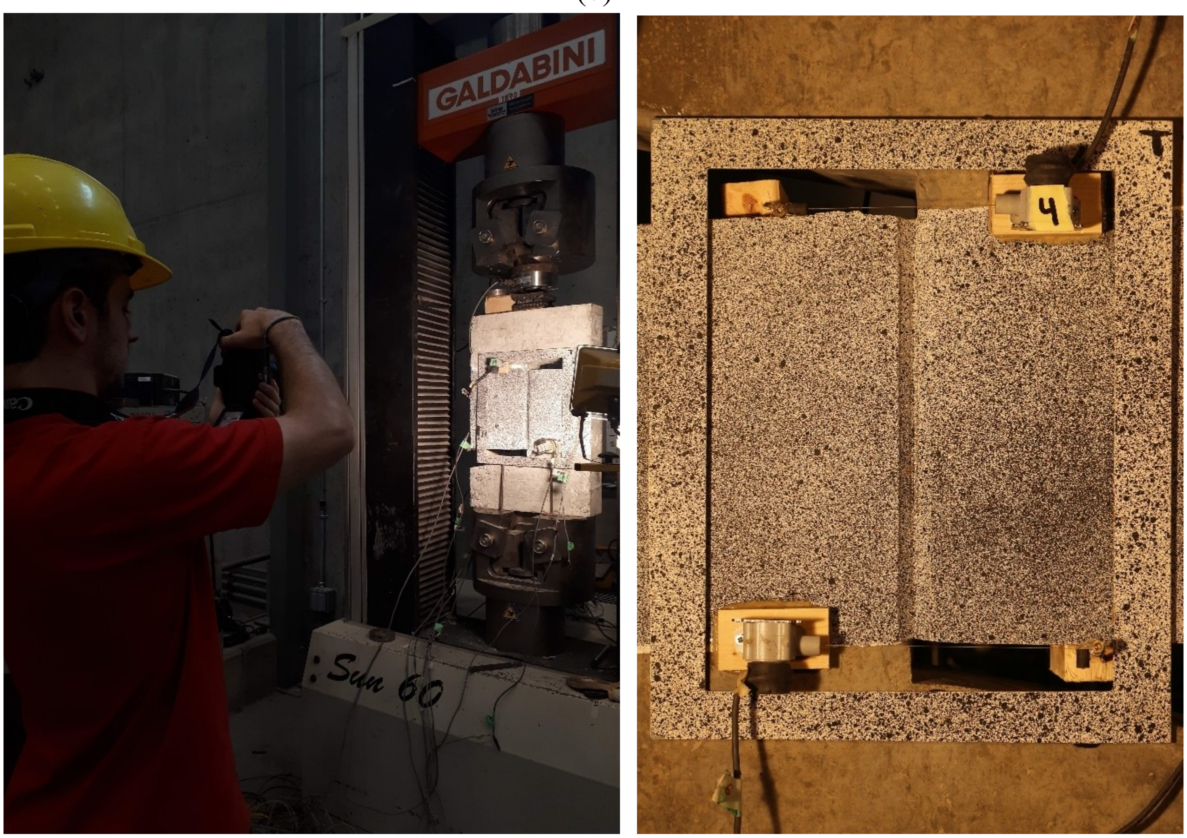

Figure 4.9: Installation of the rectangular template on the push-off specimens for ASR expansion monitoring (a) and shear crack measurements (b)

Since the inspected concrete surface deformed between the photos due to ASR expansion or shear crack growth, the use of a fixed-size reference object represented a more practical approach than using inspected surface features or concrete survey markers. Indeed, the horizontal and vertical distances between the reference points only had to be measured once. However, to avoid additional measurement errors, precautions were taken to install the template parallel to the concrete surface, so that it would appear rectangular (i.e., undistorted) if photographed by a camera positioned and oriented perfectly.

4.4.1.3 Digital camera

For both applications, a Canon T5i digital camera with a photo resolution of 17.9 Megapixel (5184 x 3456) was used to acquire images for the validation of the correction method. For each picture, the camera was positioned by hand, while taking reasonable precautions to center the middle of the shear crack in the photo and to orient the optical axis of the camera perpendicular to the inspected concrete surface. The digital device was equipped with a regular adjustable lens with a focal length of 18 to 55 mm. The lens' focal length was adjusted to 55 mm for maximum zoom. This allowed to position the camera further away from the inspected surface, and therefore, to reduce the magnitude of errors caused by camera movement. However, to obtain an optimal resolution, the camera was positioned close enough for its field of view to be only slightly larger than the template (Figure 4.9). Thus, the front element of the camera was located approximately 1250 mm from the inspected concrete surface, and the scale factor ranged from 10.4 to 11.2 pixels per mm. At this distance, small changes in camera positioning can have relatively large effects on the resulting photos. The effect of lens radial distortion could not be quantified, although considering the lens' focal length and camera distance from the inspected surface, it is possible that the induced errors were non-negligible, especially for ASR expansion measurements requiring high precision. Distortion errors induced by camera jitter, camera temperature, and other similar effects causing rigid body translation, were believed to be negligible (since relative displacements were measured). Artificial lights were used to provide consistent illumination for each photo. All images were acquired under laboratory conditions and thus, environmental conditions were consistent.

4.4.1.4 Monitoring of ASR expansion

The DIC technique was used to monitor the ASR expansion of the reactive push-off specimens 04I and 12I. The photos were taken inside the conditioning chamber (Figure 4.9a) every two to three weeks. The camera was mounted on a tripod and, for each picture, the camera and tripod were dismantled and reassembled. The template also had to be placed for each photo. Thus, measurement errors associated with template movement between the image captures also had to be considered. Similar to camera shift (subsection 4.2.1), since a relative displacement between surface points was measured, if the template were to be accidentally moved horizontally or vertically in the plane of the inspected surface, it would have had a negligible effect on the measurements. However, an out-of-plane movement or an in-plane rotation of the template about any axis would have induced an error in the measurements. Thus, reasonable precautions were taken to set up both the camera and the template in the right position each time. Finally, it can be noted that no surface staining, discoloration, and changes in moisture content were noticed during the expansion period.

4.4.1.5 Shear crack measurements

For the entire duration of the shear push-off tests, the template was adhered to the front face of the specimens and did not move. The downward movement of the cross head of the testing machine was paused at several shear displacement increments, to take pictures of the shear crack with two cameras: the hand-held Canon T5i digital camera previously described, and a Canon T6i digital camera with a photo resolution of 24.0 Megapixel (6000 x 4000), mounted on a tripod and equipped with a long lens having a fixed focal length of 180 mm (Figure 4.10). Great precautions were taken to position the camera mounted on a tripod with its optical axis perpendicular to the inspected concrete surface and aiming towards the mid-height of the shear crack because this camera remained stationary for the entire duration of the test and was employed to acquire the reference images. A remote control was used to take the pictures to ensure minimum movement from this camera. Its field of view was similar to the hand-held camera, but since a lens with a longer focal length was used, the distance between the front element of the lens and the inspected concrete surface was approximately 4300 mm. This testing arrangement created a scale factor ranging from 10.8 to 11.8 pixels per mm. After each shear displacement increment, the test was paused and photographs were taken using both the hand-held and tripod-mounted cameras. In the case of the hand-held camera, ten pictures were taken at each load level and the one with the best apparent orientation, based on visual inspection, was used in the subsequent DIC analysis.

Figure 4.10: Reference camera mounted on a tripod and equipped with a long lens

4.4.2 Post-processing of images

The DIC software GOM Correlate 2019 was used to process the pictures taken for measuring ASR expansion and shear crack slip and width. This software was selected both for its ease of use and intuitive interface, and also because it is free to use for 2D analyses and therefore readily accessible to all potential users. After importing the images in the software, the scale factor in pixels per mm was defined from the known vertical dimension of the rectangular hole in the template. The next manipulations to obtain the 2D-DIC measurements were different for the images acquired with the camera moved between the captures compared to those captured with the stationary camera. Indeed, the DIC measurements produced from the pictures taken with the moved camera had to be corrected with the proposed correction method.

4.4.2.1 Images acquired with the moved camera

First, subsets with dimensions of 19 x 19 pixels were created at the four corners of the template (points A, B, C, and D in Figure 4.11 and Figure 4.12). To ensure that these four subsets formed a rectangle in the reality (but not necessarily in the image), they were created in specific locations previously measured with a ruler. Second, a 2D coordinate system with its origin at point A and with the same orientation as the images was created. Third, four more subsets were created on the concrete surface; two on each side of the shear crack, forming two pairs (i.e., 1 with 2, and 3 with 4, in Figure 4.11 and Figure 4.12). The locations of these subsets depended on the application. For ASR expansion, the subsets were created right next to the studs, between the internal steel reinforcement, so that the gauge length would be similar to that of the DEMEC strain gauge presented in Chapter 3, i.e., 200 mm. For shear crack slips and widths, the subsets were created right next to the vertical notch, about 10 mm away from the crack. One pair of subsets was at the bottom of the shear plane and the other one was at the top. The created subsets were tracked by the software in all of the images and, except for point A (i.e., the origin), the X and Y coordinates of the subsets were then exported to an Excel spreadsheet. These distorted coordinates and the known undistorted coordinates of points B, C, and D were used as inputs in Equations 4-3 and 4-4 to calculate, with the Microsoft Excel Solver add-in program, the undistorted coordinates x_0 and y_0 of the four subsets on the concrete surface. From the corrected subset coordinates of each image and those of the first one, the ASR expansion or the crack width and slip could finally be calculated for the two pairs of subsets. The ASR expansion measurements made with the two pairs of subsets were averaged together, but the top and bottom crack width and slip measurements from the push-off tests were kept separate.

Figure 4.11: ASR expansion measurement with the correction method on GOM Correlate 2019

(a) (b)

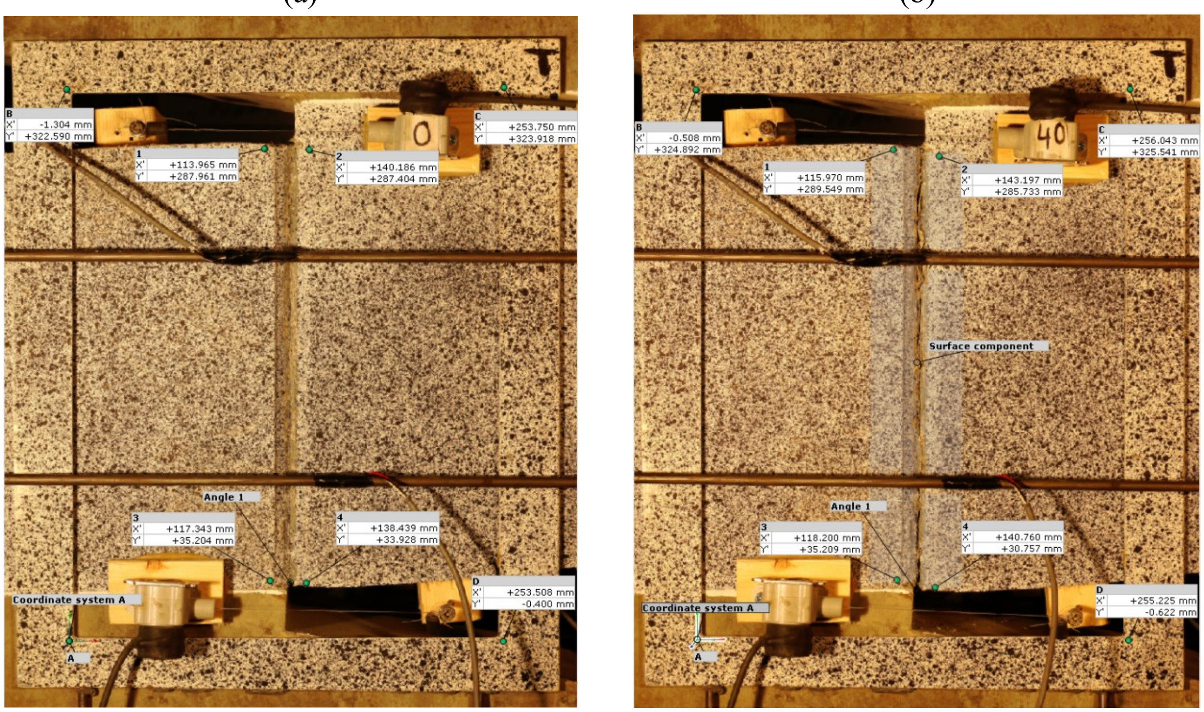

Figure 4.12: Measurement of crack width and slip using GOM Correlate 2019 and the correction method: first (a) and last (b) pictures of push-off test

4.4.2.2 Images acquired with the stationary camera

The methodology followed on the GOM Correlate software to process the images acquired with the fixed camera was simpler, since the subset coordinates used for calculating the crack slip and width measurements did not need to be corrected for camera movement. Thus, subsets were not created on the template, but only on the concrete surface, forming the pairs of subsets at the top and bottom of the shear crack. The X and Y coordinates of these subsets were directly used to calculate the crack width and slip, respectively, in all images. These 2D-DIC measurements were used as a reference when assessing the accuracy of the corrected DIC measurements made from the images acquired with the hand-held camera.

4.4.2.3 Shear crack angle relative to the template

Although reasonable precautions were taken to align the longer sides of the template with the orientation of the shear crack, a small angle could be measured in the GOM software. (Note: this is only relevant since the crack width and slip values were assumed to coincide with the x and y components of the total displacement, respectively.) However, this angle always remained below one degree for the different push-off specimens. Since it had little effect on the crack width and slip measurements, it was not accounted for. Besides, for the purpose of this research, which was to find the accuracy of DIC measurements corrected with the proposed correction method, such angle had a negligible influence on the results. Indeed, the corrected measurements were evaluated on the basis of the measurements made from the images acquired with the stationary camera with a long lens, which were not corrected for the angle of the crack relative to the template either. Note that, if necessary, this angle could have been calculated and accounted for in the analysis by using the corrected coordinates of additional subsets created at the ends of the crack.

4.5 Results and discussion

In this section, for the two applications tested, the original 2D-DIC measurement errors and the residual errors obtained with the proposed correction method will be presented and discussed.

4.5.1 ASR expansion measurements

Measurements of the final ASR expansion in specimens 04I and 12I are presented in Table 4.1. They include the measurements made with the partially embedded studs presented in Chapter 3, i.e., the reference measurements, the original (uncorrected) 2D-DIC measurements, and the corrected measurements using the proposed method. Errors were calculated as the difference in expansion measurements between the DIC analysis and the conventional stud measurements. The absolute errors of the original and corrected expansion measurements, and the corresponding error reduction, are also presented. All the strain percentages presented in Table 4.1 are associated with a dimension in parentheses representing the corresponding length change for the gauge length of 200 mm. Even though precautions were taken to position the template and the camera properly, the absolute errors of the original DIC measurements were above 5% (10 mm). The correction method improved the readings, but did not reduce the measurement errors below the tolerable strain error of ± 0.01%. This suggests that the procedure used did not adequately compensate for the errors induced by the camera movements between photographs.

Table 4.1: 2D-DIC final expansion measurement errors

ID	Reference expansion (studs)	DIC measured expansion	Original error	Corrected expansion	Residual error	Error reduction
04I	0.040% (0.080 mm)	-5.170% (-10.34 mm)	-5.210% (-10.42 mm)	0.073% (0.146 mm)	+0.033% (+0.066 mm)	5.176% (10.35 mm)
12I	0.027% (0.054 mm)	-5.090% (-10.18 mm)	-5.117% (-10.23 mm)	-0.091% (-0.182 mm)	-0.118% (-0.236 mm)	4.999% (9.998 mm)

It should be noted that for both specimens, since only the first and last pictures taken during the expansion period were compared on GOM Correlate 2019, the number of measurements is limited. Also, the reference expansion measurements produced with the studs present their own uncertainty. (Note that a stationary reference camera with a longer focal length could not be used in this case due to space constraints inside the environmental chamber.) Thus, it is difficult to judge on the accuracy of the measurements obtained with the proposed correction method. If more DIC measurements were made and corrected, the results would be more conclusive, and it would be easier to evaluate the achievable residual error.

Nevertheless, even the smallest residual error obtained, i.e., 0.033%, was more than three times the tolerable expansion measurement error. Thus, it can be concluded, taking into account the characteristics of the conducted experiments (i.e., gauge length of 200 mm, the template movement between the pictures, the spatial resolution, the lens focal length, etc.), that the combination of the 2D-DIC technique with the correction method could not produce the required measurement accuracy for ASR expansion monitoring which is characterized by very small displacements (less than 0.08 mm for a gauge length of 200 mm).

Increasing the gauge length would likely have a negligible effect on the corrected length change measurement error, and therefore, the residual ASR expansion measurement error would be reduced. For example, if a larger planar concrete surface was photographed, and subsets were created one meter away from each other, a length change measurement error of ±0.05 mm would correspond to a strain measurement error of ±0.005%, i.e., half of the tolerable error for ASR expansion measurement. This may present an opportunity for future research.

4.5.2 Crack width and slip measurements

The 2D-DIC measurements for shear crack slip and width from the seven push-off tests were plotted against the shear displacement increment number (Figure 4.13). Curves were made for the top and the bottom of the shear crack, separately. The measurements include those made from the hand-held camera pictures (i.e., the original measurements), the corrected measurements, and those made with the stationary camera (i.e., the reference measurements). Although the reference measurements may present their own unknown error (e.g. very small off-axis camera positioning), these were negligible compared to the errors in the measurements made with the images acquired with the hand-held camera. Thus, they are not considered in the analysis of the results.

Even though precautions were taken to place the hand-held camera properly, as seen from the original and reference measurements, large errors were obtained. The curves formed with the corrected measurements and the reference measurements are very similar, suggesting that the correction method significantly improved the measurements from all the tests.

00E

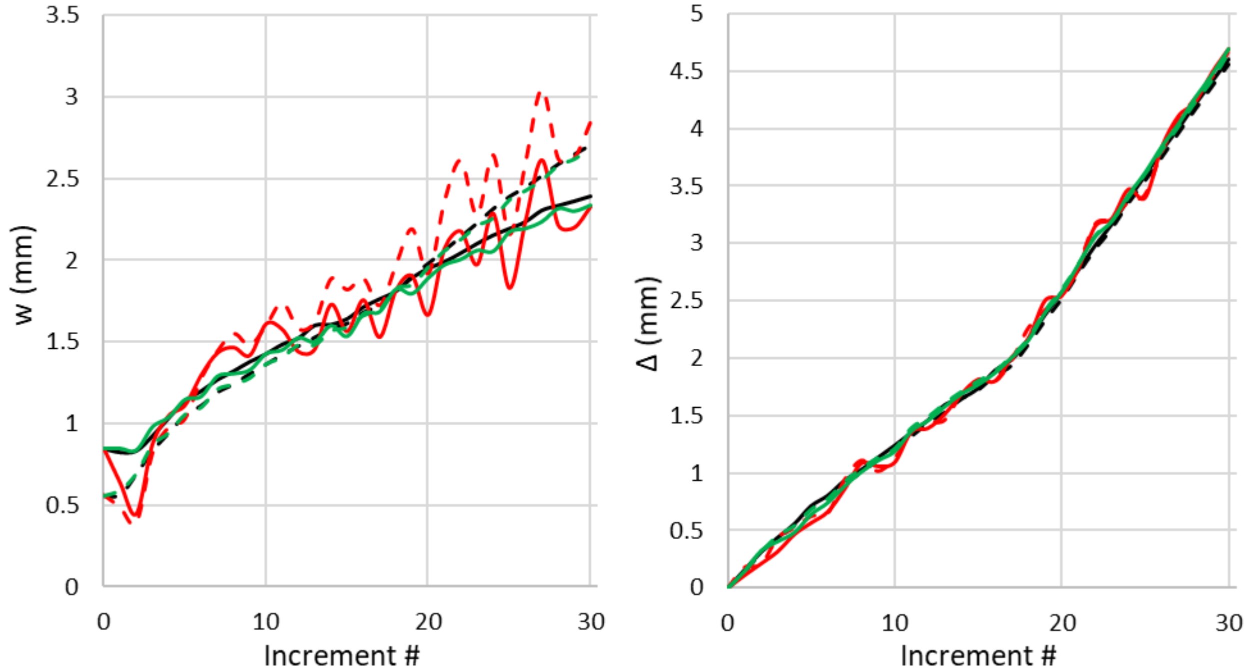
w (mm)
Increment #
Δ (mm)
Increment #

00I

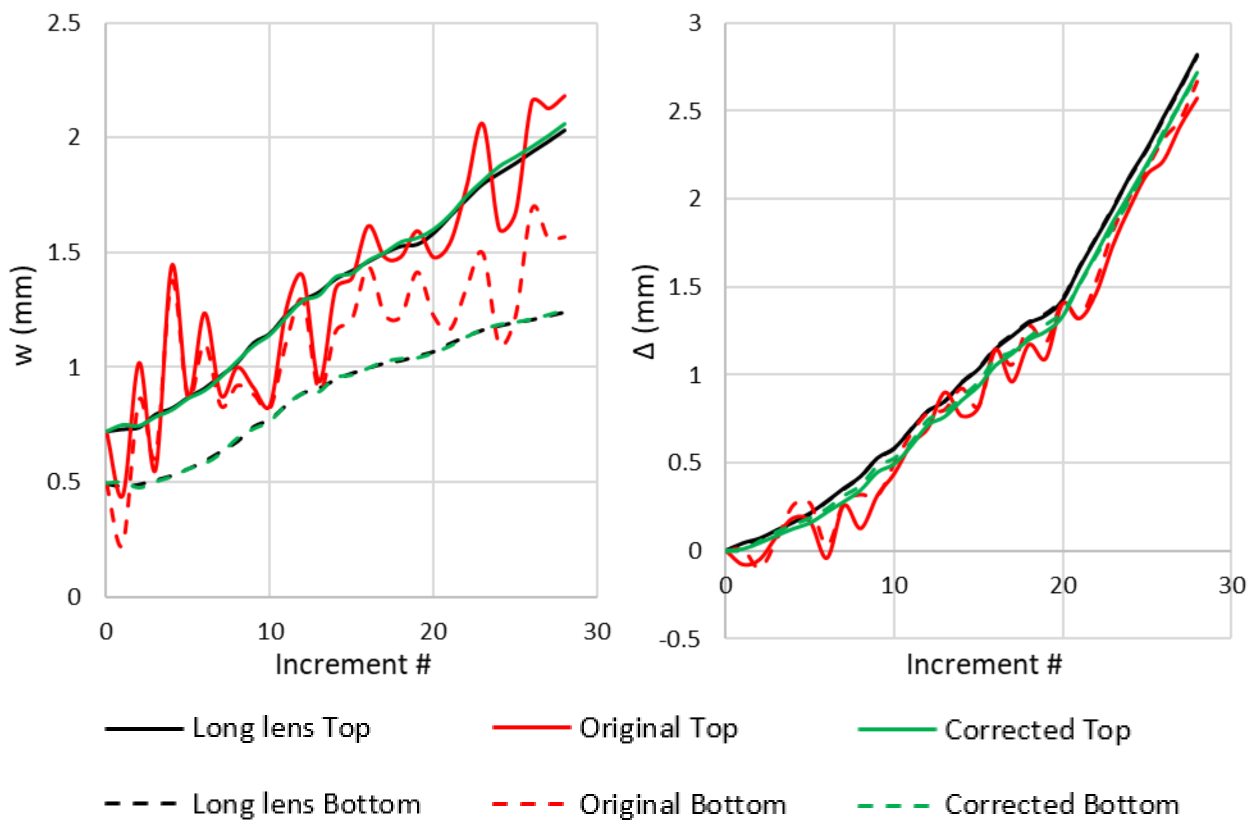
w (mm)
Increment #
Δ (mm)
Increment #
Long lens Top
Original Top
Corrected Top
Long lens Bottom
Original Bottom
Corrected Bottom

04E

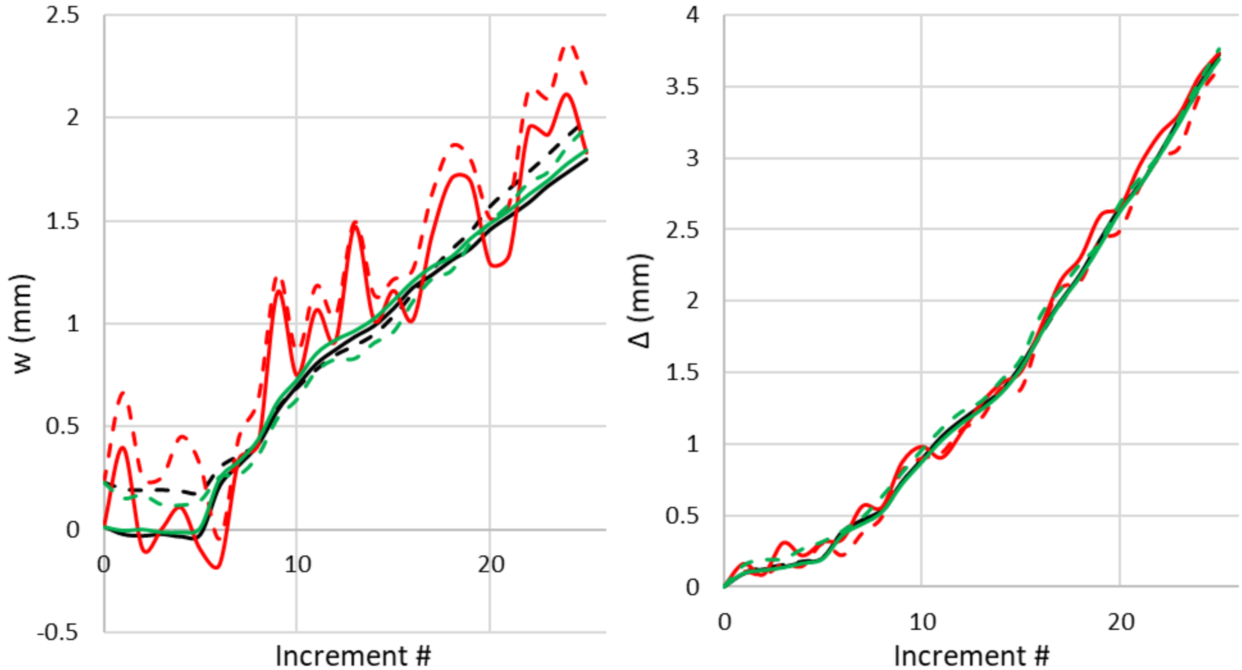
w (mm)
Increment #
Δ (mm)
Increment #

04I

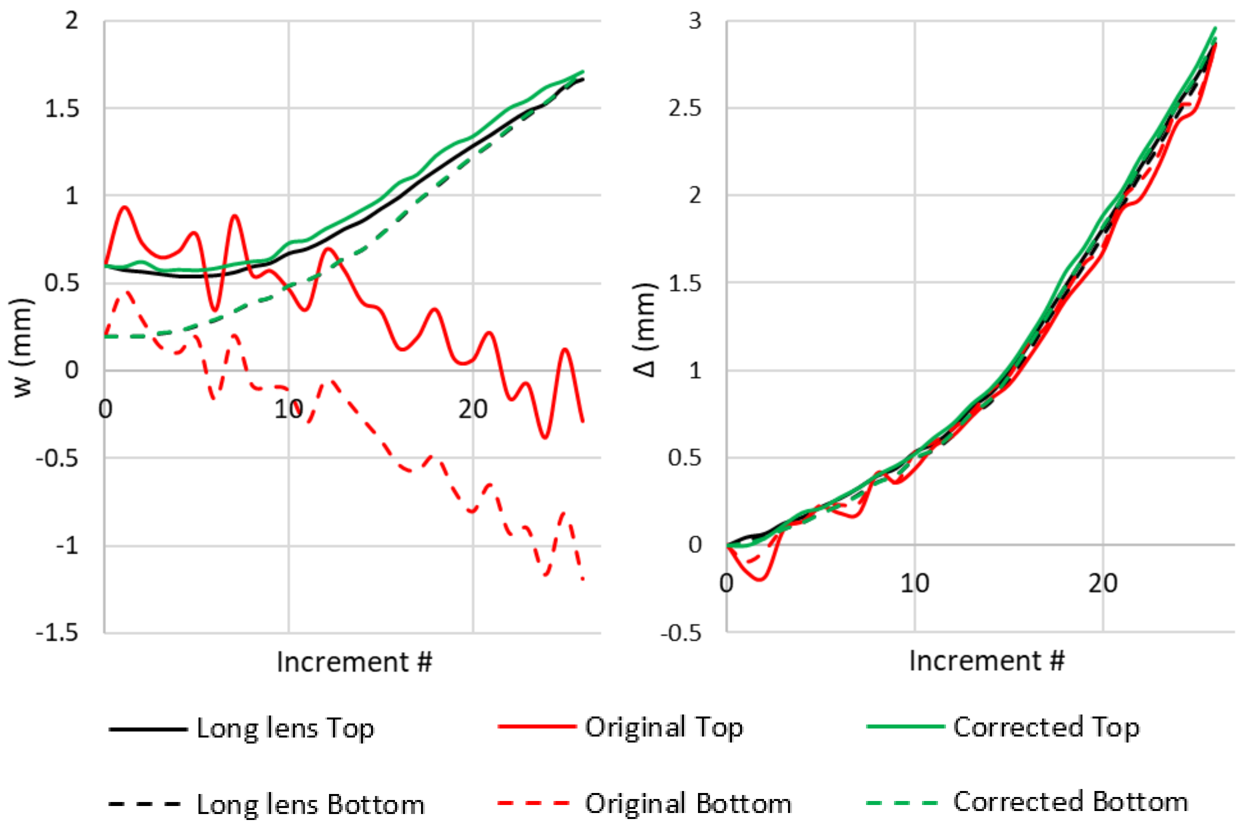
w (mm)
Increment #
Δ (mm)
Increment #
Long lens Top
Original Top
Corrected Top
Long lens Bottom
Original Bottom
Corrected Bottom

07E

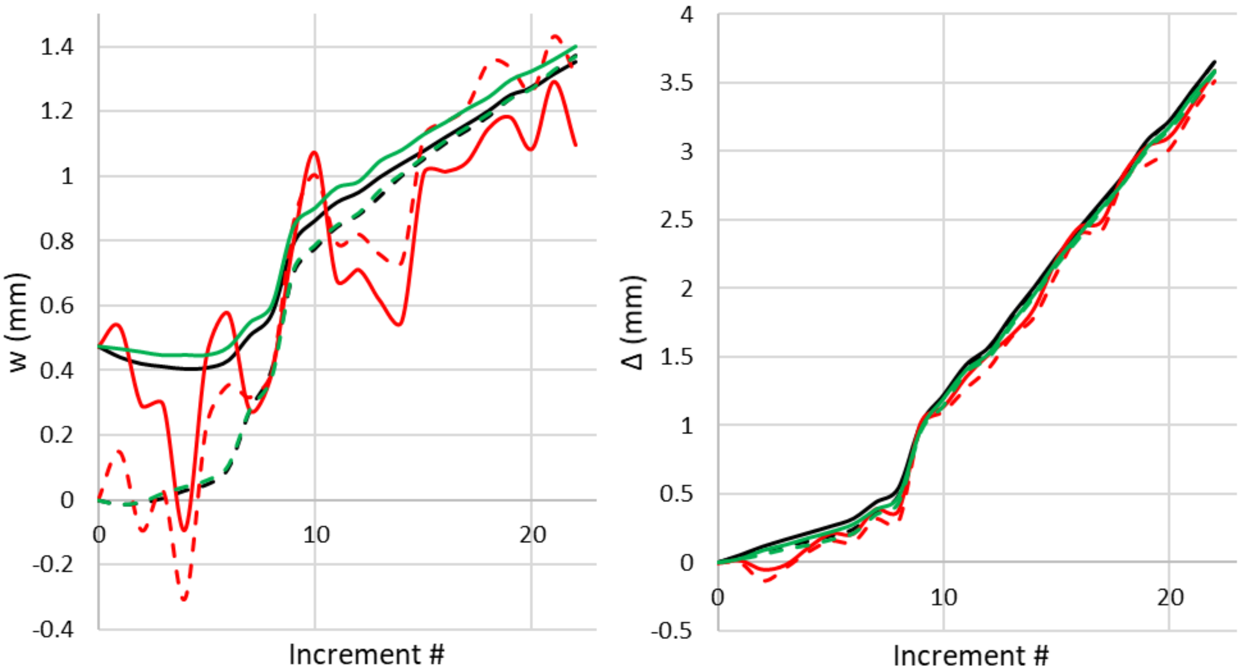

w (mm)
Increment #
Δ (mm)
Increment #

07I

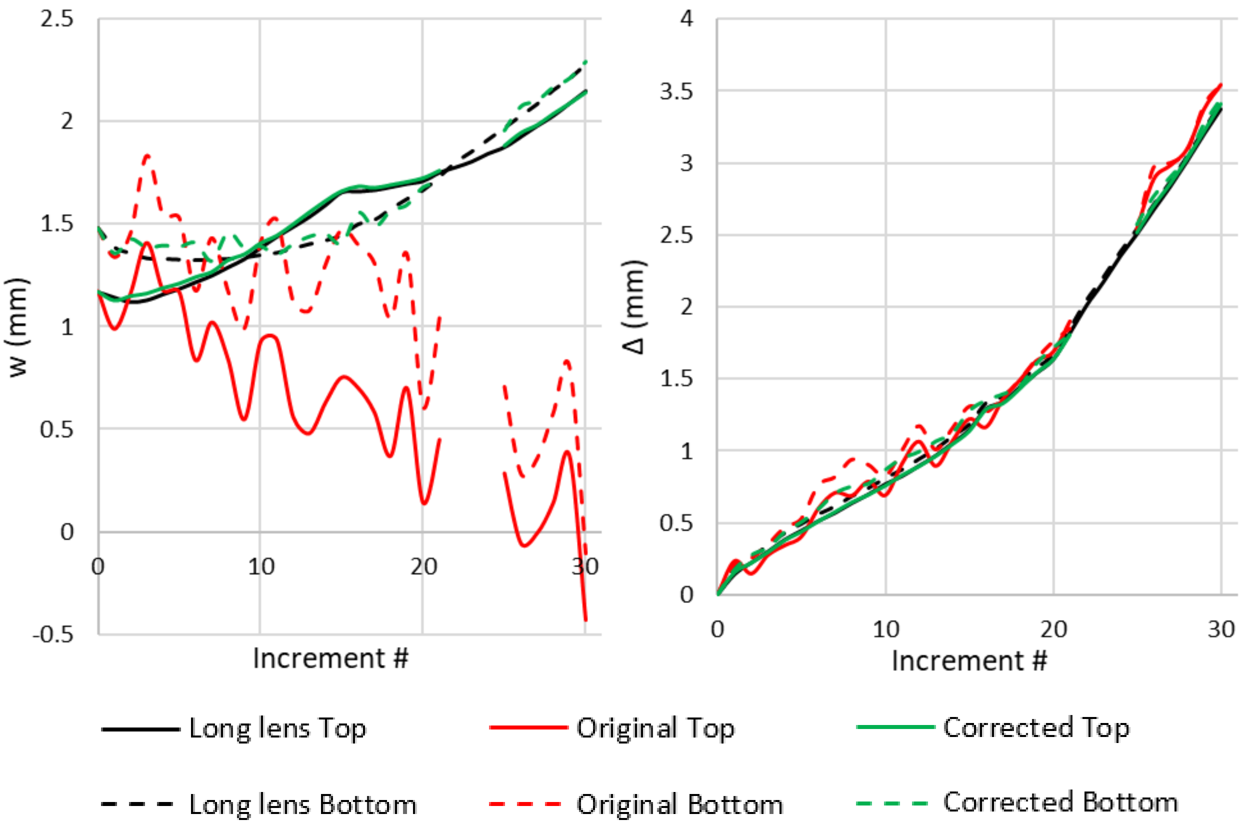

w (mm)
Increment #
Δ (mm)
Increment #
Long lens Top
Original Top
Corrected Top
Long lens Bottom
Original Bottom
Corrected Bottom

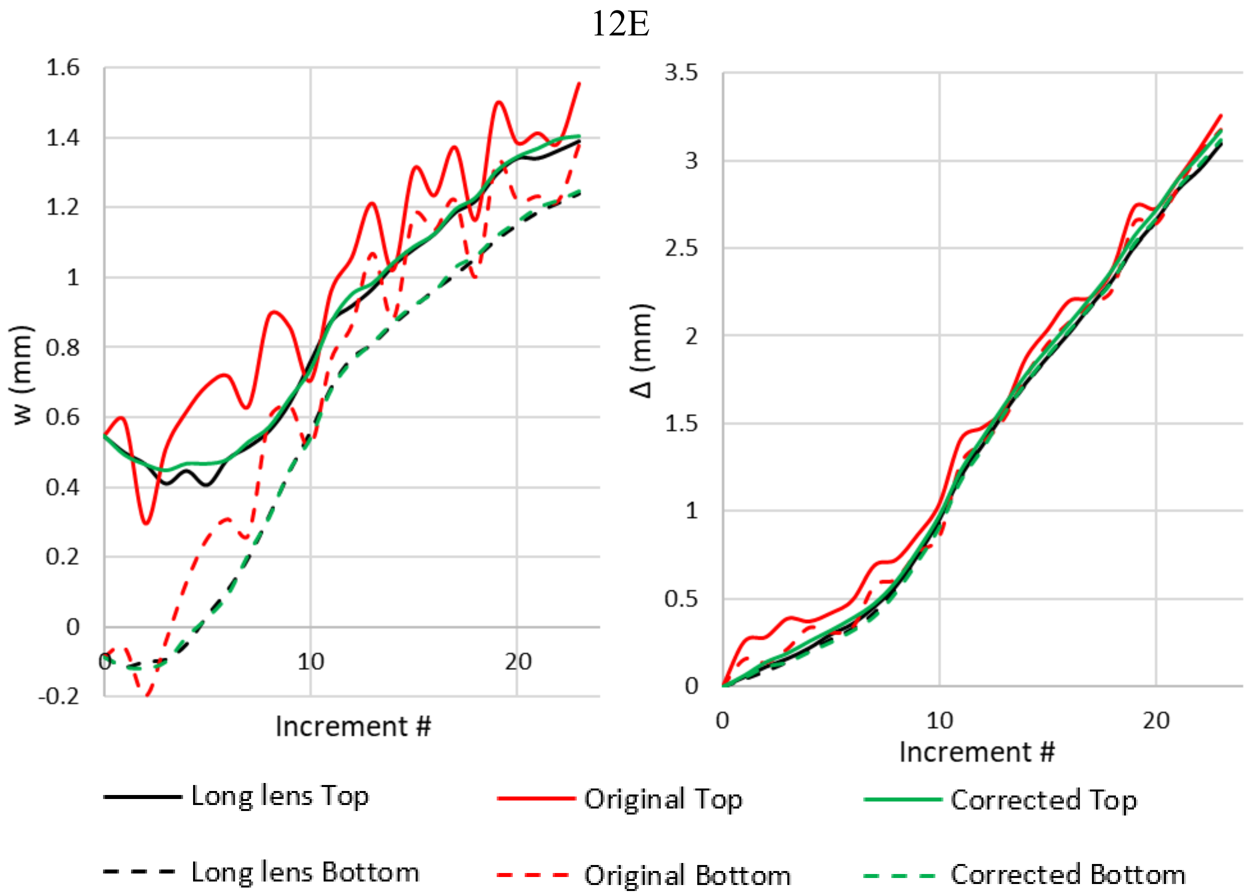

Figure 4.13: Crack width (left) and slip (right) 2D-DIC measurements

For each push-off specimen, the average absolute errors of the original and corrected crack slip and width measurements are presented in Table 4.2. Note that the top and bottom measurement errors were averaged together. The original-to-corrected measurement error ratios (i.e., error reduction ratios) are also presented.

Table 4.2: Average absolute error for the original and corrected 2D-DIC shear crack measurements

ID	Average absolute measurement error (μm)					
	w			Δ		
	Original	Corrected	Reduction ratio	Original	Corrected	Reduction ratio
00E	157	29.4	5.35	76.2	43.2	1.77
00I	216	10.0	21.7	138	72.8	1.89
04E	240	45.7	5.25	137	46.2	2.97
04I	926	30.9	30.0	66.3	30.7	2.16
07E	149	26.2	5.67	103	44.3	2.32
07I	790	26.9	29.3	89.6	24.0	3.74
12E	138	11.6	11.8	101	29.5	3.43
Average	351	25.8	15.6	102	41.5	2.61

For all the test specimens, the average residual crack width and slip measurement errors satisfied the selected tolerance limit of ±0.1 mm. Furthermore, only 0.82% of all the crack width residual measurement errors and 3.85% of all the crack slip residual measurement errors exceeded this limit (Figure 4.14 and Figure 4.15). These results suggest that combining the proposed correction method with the DIC technique allowed to overcome the challenges associated with camera positioning and that, under laboratory conditions, the required measurement accuracy for monitoring concrete cracks is achievable using a hand-held camera. Additional outdoor testing would be necessary to validate the approach for real structural inspections. Also, it is worthwhile to recall that during the push-off tests, the template remained fixed. Of course, it is impossible that the surface of the template was perfectly coplanar with the inspected surface, but the measurement errors associated were negligible, as the residual errors suggest. In reality, if a similar template were to be used in structural inspections, it would probably be placed by hand before each photograph, inducing additional measurement errors associated to template out-of-plane movement and in-plane rotation between inspection photographs. Nevertheless, other ways of obtaining the four reference points in the plane of the inspected surface exist, and they do not present such an issue.

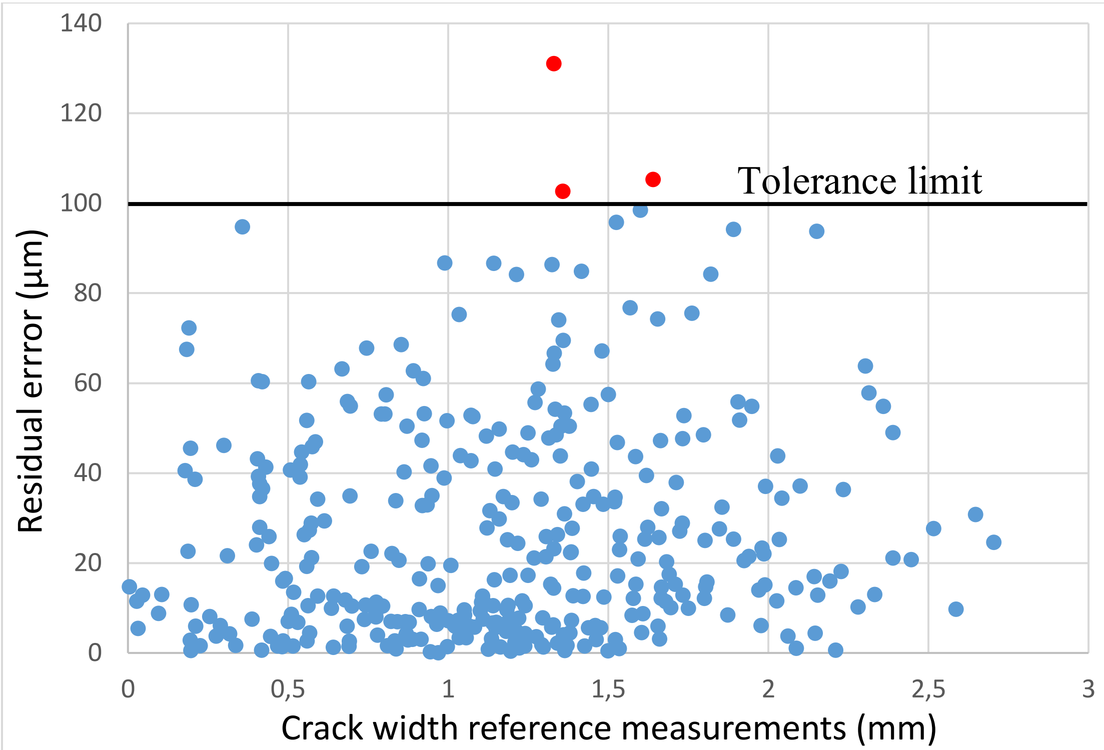

Figure 4.14: Crack width residual measurement errors

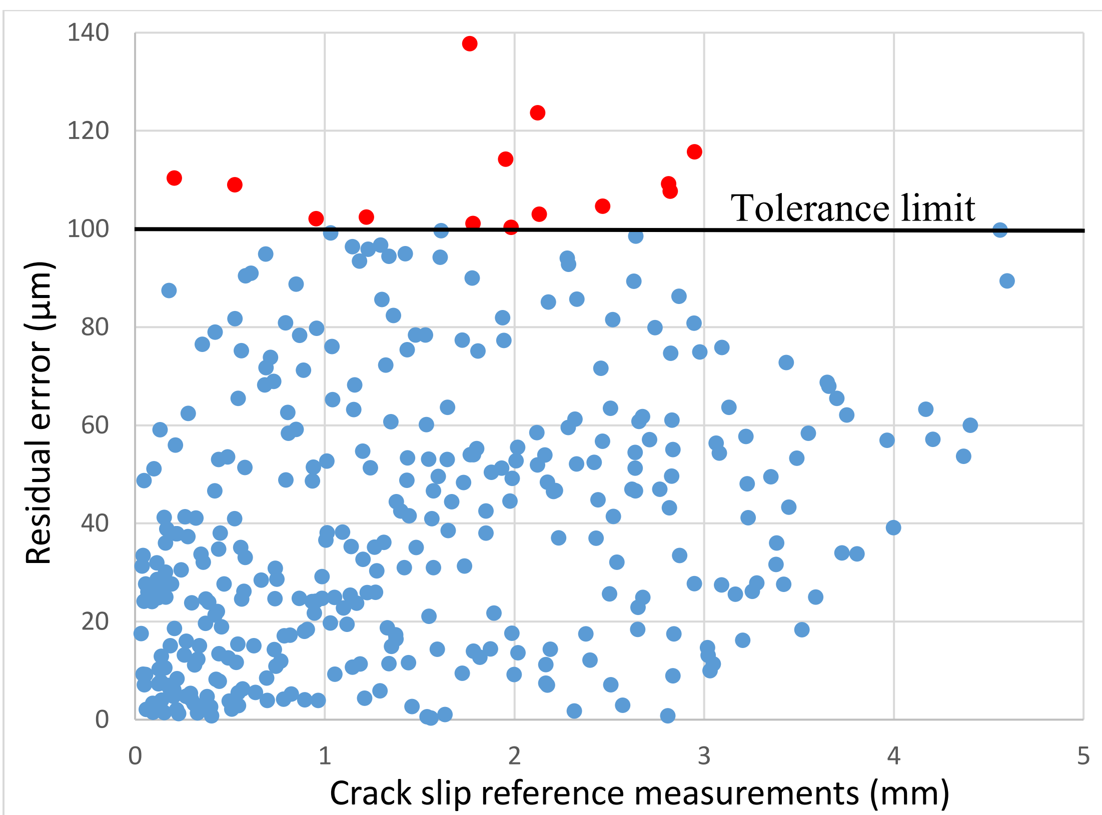

Figure 4.15: Crack slip residual measurement errors

Finally, it is unclear why, except for specimens 04I and 07I, the average residual errors were smaller for the crack width than the crack slip. Since the subsets used for these measurements were located at the top and bottom of the images and not towards their sides, it is possible that lens distortion affected their vertical displacements more significantly, but it is not believed that this effect alone could explain this difference (although it could not be quantified).

4.5.3 Sources of error in the original and corrected measurements

As seen from Table 4.1 Table 4.2, the original absolute measurement errors were greater for ASR expansions than crack widths, and were greater for crack widths than crack slips. These differences can mainly be attributed to the relative distance between the pair of subsets used for the measurements: the more distance between two subsets, the greater will be the uncorrected absolute measurement errors associated with camera positioning. For example, as seen from Figure 4.12, the horizontal distances between the subsets in each pair used for crack width and slip measurements were greater than the vertical distances, resulting in larger crack width absolute errors caused by camera movement. Obviously, the largest original errors were in general accompanied by a larger correction, which partially explains the differences between the error reductions. Although the differences between the original and corrected absolute measurement errors varied greatly (from 10.34 mm for the ASR final expansion of 04I to 0.0331 mm for the crack slip of 00E), they were in general large enough to suggest that, among the sources of original DIC measurement errors, improper camera positioning was the most important one. However, if a longer lens focal length was used, the errors due to camera panning, tilting and out-of-plane movement between photographs would be reduced significantly.

Since the residual errors obtained for the corrected ASR expansion measurements, i.e., 66 and 236 μm, were significantly higher than the average errors obtained for the corrected crack measurements, i.e., 25.8 and 41.5 μm, it is reasonable to assume that the movement of the template between the photographs had a considerably negative effect on the measurements. Indeed, this source of error was arguably the only significant one not shared by the two applications. Errors due to reference object movement could easily be quantified, simply by photographing a fixed surface with a stationary camera several times, making sure to remove and install the template between each of them.

Other sources of error in the experiments conducted, which contributed to the residual measurement errors but could not be quantified, include but are not limited to:

1. operator errors when manually measuring the relative distances between the reference points with a ruler;
2. operator errors when creating the reference subset points and defining the scale factor in the software;
3. errors due to lens radial distortion, which were more important for the reference points since those were created near the edges of the images;
4. and errors related to subpixel accuracy, which were relatively small, considering the spatial resolutions used in the two applications.

5. CONCLUSIONS AND RECOMMENDATIONS

5.1 Effect of ASR expansion on aggregate interlock

Seven pre-cracked reinforced concrete push-off specimens were tested to study the effect of low to moderate ASR expansion levels (i.e., 0.04, 0.07 and 0.12%) on the aggregate interlock shear behaviour. The simultaneous effects of chemical prestressing and ASR microcracks on the aggregate interlock were decoupled by testing specimens with internal reinforcement and others prestressed with external reinforcement. Although prestressing reduced the crack width obtained from the pre-cracking phase, it did not affect the crack dilation behaviour during loading nor the maximum shear strength. The steepest crack opening path was obtained for the internally reinforced push-off specimen with an expansion of 0.07%, suggesting that ASR microcracks in damaged coarse aggregates reduced the crack roughness. However, during a visible inspection of the separated crack faces following the tests, it was observed that all specimens presented a majority of coarse aggregates split by the shear crack without clear signs of significant differences. This suggests that the tensile strength ratio between the aggregates and ITZ was not high enough to ensure a tortuous shear crack propagating around the coarse aggregates, even in sound concrete. Nevertheless, aggregate interlock shear strength reductions of 26.6 and 28.6% were observed for internally reinforced specimens with expansions of 0.04 and 0.07%, respectively, and their shear stiffness was reduced by 44%. These results suggest that ASR microcracks did in fact reduce the roughness of shear cracks. However, these shear strength reductions were more pronounced than expected, especially for the expansion level of 0.04%, which should normally be characterised by ASR-induced microcracks in the aggregates which are still too small to have reached the cement paste. Thus, it is likely that the results were at least partially attributable to natural variability in concrete shear strength. Yet, it may still be concluded that the decrease in aggregate interlock strength due to ASR microcracks governed over the increase in strength from chemical prestressing for the low confinement levels considered in this study. Note that an expansion of 0.12% could not be reached in a reasonable amount of time so its effect on aggregate interlock could not be measured.

Further testing is recommended for larger expansion levels and to validate the above findings. Also, it would be interesting to conduct similar experiments using a concrete mix design resulting in a higher tensile strength ratio between the aggregates and ITZ, such that clear differences in crack roughness could be obtained between the damaged and sound specimens. Moreover, the reinforcement restraint stiffness was smaller for the externally reinforced specimens than the internally reinforced specimens, which significantly reduced their shear strength. If a similar test program were to be conducted in the future, it would be better to have the same reinforcement restraint stiffness for the two types of specimens to allow an easier comparison of the results. Moreover, the external and internal reinforcement restraint stiffnesses were in fact both relatively low, which may partially explain why the simplified aggregate interlock models from Walraven & Reinhardt (1981), Gambarova & Karakoc (1983), and Li et al. (1989) all overpredicted the shear stresses. This may suggest that the simplified models are not well-suited for lightly reinforced concrete, but further testing is recommended to validate this. It would also be interesting to conduct similar experiments using higher reinforcement restraint stiffnesses which are more representative of regular reinforced concrete members. Reinforcement ratios could also be varied to study the effect of different levels of confinement, although increasing it too much may extend the ASR expansion period significantly.

5.2 A method to correct 2D-DIC measurement error due to camera movement

A method was proposed to correct 2D-DIC measurement errors associated with changes in camera positioning between multiple image captures. It involves tracking the apparent displacements of four reference points with known real vertical and horizontal relative distances and located in the plane of the inspected surface. The method is applicable to absolute and relative displacement measurements. In this project, it was applied for monitoring ASR expansion and shear crack kinematics in concrete push-off specimens by fixing a rectangular template on their front face. A non-expensive standard quality camera equipped with a focal length adjusted to 55 mm was used to acquire the images. For each photograph, reasonable precautions were taken to hand-position the camera approximately 1.25 m away from the inspected surface and with its optical axis oriented perpendicular to the inspected surface. The uncorrected 2D-DIC measurement errors due to camera movement were significant and highly dependent on the relative distance between the two subsets used for a measurement. The proposed correction method significantly improved the measurements from the experiments. However, for ASR expansion monitoring, the absolute strain measurement errors could not be reduced below a selected tolerance limit of ±0.01% when a gauge length of 200 mm was used. This was partially attributed to improper positioning of a reference rectangular template fixed on the inspected surface before each photograph. On the other hand, 99 and 96% of the residual measurement errors were within the selected tolerance limit of ±0.1 mm for the corrected crack width and slip measurements, respectively. Note that the average corrected measurement errors for crack width and slip were ±25.8 and ±41.5 μm, respectively. It was therefore concluded that applying the proposed correction method to the long-term DIC monitoring of shear cracks can overcome errors associated with camera movement between photographs. Nevertheless, additional outdoor testing is recommended to validate the proposed approach for real structural inspections.

To obtain four reference points in the field of view of the camera, the use of a planar reference object such as the template used in this project is very practical, since it can easily be carried to all inspected critical locations of a structure by an inspector. The errors associated with movement of a reference object between inspection captures can be mitigated by equipping the camera a long focal length. Also, the magnitude of errors associated with this source of error could easily be quantified by photographing a fixed surface with a stationary camera several times, making sure to remove and install the reference object (e.g. a template) before each of them. If the errors are too significant for a given measurement application, other ways of creating the four reference points exist. For example, four survey markers can be installed on the surface of a structure. Preferably, these markers should remain fixed during the inspection period, although some applications may not require such measurement precision. Also, the use of an equipment capable of acquiring digital photographs while projecting four laser reference points on the structure's surface is another potential technique that remains to be tried. This would allow completely remote inspections.

For ASR expansion monitoring with the DIC technique and the proposed approach, it is recommended that a large gauge length be used since the residual absolute strain measurement errors are inversely proportional to it. For example, if a gauge length of 1 m is used, a residual absolute relative displacement measurement error of 50 μm, which was achievable as per demonstrated in this project, will correspond to a strain error of 0.005%, i.e., less than the tolerable error used in this project for ASR expansion measurement.

6. REFERENCES

Abe, M., Kikuta, S., Masuda, Y., & Tomozawa, F. (1989). Experimental study on mechanical behaviour of reinforced concrete members affected by alkali-aggregate reaction. *Alkali-Aggreagte Reaction 8th International Conference*, 691–696.

Abolhasannejad, V., Huang, X., & Namazi, N. (2018). Developing an Optical Image-Based Method for Bridge Deformation Measurement Considering Camera Motion. *Sensors*, *18*(9), 18. https://doi.org/10.3390/s18092754

Acciaioli, A., Lionello, G., & Baleani, M. (2018). Experimentally achievable accuracy using a digital image correlation technique in measuring small-magnitude (< 0.1%) homogeneous strain fields. *Materials*, *11*(5), 1–14. https://doi.org/10.3390/ma11050751

Ahmed, T., Burley, E., & Rigden, S. (1998). The static and fatigue strength of reinforced concrete beams affected by alkali-silica reaction. *ACI Materials Journal*, *95*(4), 376–387. https://doi.org/10.14359/380

Ahmed, T. M. A., Burley, E., & Rigden, S. R. (1999). The effect of alkali±silica reaction on the fatigue behaviour of plain concrete tested in compression, indirect tension and flexure. *Magazine of Concrete Research*, *51*(6), 375–390.

Ali, M. A., & White, R. N. (1999). Enhanced contact model for shear friction of normal and high-strength concrete. *ACI Structural Journal*, *96*(3), 348–360.

Allard, A., Bilodeau, S., Pissot, F., Fournier, B., Bastien, J., & Bissonnette, B. (2018). *Expansive behavior of thick concrete slabs affected by alkali-silica reaction (ASR)*. https://doi.org/10.1016/j.conbuildmat.2018.03.159

ASCE-ACI Committee 445 on Shear and Torsion. (1998). Recent Approaches to Shear Design of Structural Concrete. *Journal of Structural Engineering*, *124*(12), 1375–1417. https://doi.org/10.1061/(ASCE)0733-9445(1998)124:12(1375)

Atkins. (2017). *Improved Asset Management using Digital Image Correlation - YouTube*. https://www.youtube.com/watch?v=JJoKjwLgdHY

Bach, F., Thorsen, T. S., & Nielsen, M. P. (1993). Load-carrying capacity of structural members subjected to alkali-silica reactions. *Construction and Building Materials*, *7*(2), 109–115.

Barbosa, R. A., & Hansen, K. K. (2014). The influence of alkali-silica reaction and crack orientation on the mechanical properties of concrete. *Proceedings of the*

10th Fib International PhD Symposium in Civil Engineering, 111–116.

Barbosa, R. A., Hansen, S. G., Hoang, L. C., & Hansen, K. K. (2018). *Residual shear strength of a severely ASR-damaged flat slab bridge*. https://doi.org/10.1016/j.engstruct.2018.01.056

Barr, B., & Hasso, E. B. D. (1986). Development of a compact cylindrical shear test specimen. *Journal of Materials Science Letters*, *5*(12), 1305–1308. https://doi.org/10.1007/BF01729401

Barranger, Y., Doumalin, P., Dupré, J. C., & Germaneau, A. (2010). Digital image correlation accuracy: Influence of kind of speckle and recording setup. *14th International Conference on Experimental Mechanics*, *6*. https://doi.org/10.1051/epjconf/20100631002

Bazant, Z. P., & Gambarova, P. (1980). ROUGH CRACKS IN REINFORCED CONCRETE. *ASCE J Struct Div*, *106*(4), 819–842.

Bentz, E. C., Vecchio, F. J., & Collins, M. P. (2006). Simplified modified compression field theory for calculating shear strength of reinforced concrete elements. *ACI Structural Journal*, *103*(4), 614–624.

Berra, M., Faggiani, G., Mangialardi, T., & Paolini ERSE SpA, A. (2010). Influence of stress restraint on the expansive behaviour of concrete affected by alkali-silica reaction. *Cement and Concrete Research*, *40*, 1403–1409. https://doi.org/10.1016/j.cemconres.2010.05.002

Bilodeau, S., Allard, A., Bastien, J., Pissot, F., Fournier, B., Mitchell, D., & Bissonnette, B. (2016). Performance Evaluation of Thick Concrete Slabs Affected by Alkali-Silica Reaction (ASR) - Part II: Structural Aspects. *15th International Conference on Alkali-Aggregate Reaction in Concrete*.

Boenig, A., Fúnez, L. M., Memberg, L., Roche, J., Tinkey, B., Klingner, R. E., & Fowler, T. J. (2009). Structural assessment of bridges with premature concrete deterioration due to expansive reactions. *ACI Structural Journal*, *106*(2), 196–204. https://doi.org/10.14359/56358

Calvi, P. M. (2014). *A Theory for the Shear Behaviour of Cracks Providing a Basis for the Assessment of Cracked Reinforced Concrete Structures*. 367.

Campana, S., Ruiz, M. F., Anastasi, A., & Muttoni, A. (2013). Analysis of shear-transfer actions on one-way RC members based on measured cracking pattern and failure kinematics. *Magazine of Concrete Research*, *65*(6), 386–404. https://doi.org/10.1680/macr.12.00142

Cavagnis, F., Fernández Ruiz, M., & Muttoni, A. (2018a). An analysis of the shear-transfer actions in reinforced concrete members without transverse reinforcement based on refined experimental measurements. *Structural Concrete*, *19*(1), 49–64. https://doi.org/10.1002/suco.201700145

Cavagnis, F., Fernández Ruiz, M., & Muttoni, A. (2018b). A mechanical model for failures in shear of members without transverse reinforcement based on development of a critical shear crack. *Engineering Structures*, *157*, 300–315. https://doi.org/10.1016/j.engstruct.2017.12.004

Chana, P., & Thompson, D. (1992). Laboratory testing and assessment of structural members affected by alkali silica reaction. *9th ICAAR*.

Chen, Y., Wei, J., Huang, H., Jin, W., & Yu, Q. (2018). Application of 3D-DIC to characterize the effect of aggregate size and volume on non-uniform shrinkage strain distribution in concrete. *Cement and Concrete Composites*, *86*, 178–189. https://doi.org/10.1016/j.cemconcomp.2017.11.005

Clark, L., & Ng, K. (1989). The Effect of Alkali-Silica Reaction on the Punching Shear Strength of Reinforced Concrete Slabs. *8th International Conference on AAR in Concrete*.

Correlated Solutions. (n.d.). *Application Note AN -1701 Speckle Pattern Fundamentals*. http://www.correlatedsolutions.com/support/index.php?/Knowledgebase/Article/GetAttachment/80/14750

Cusson, D. ;, & Isgor, B. (2004). *Durability of concrete structures: prevention, evaluation, inspection, repair and prediction*. http://irc.nrc-cnrc.gc.ca/ircpubs

De Souza, D. J., Sanchez, L. F. M., & De Grazia, M. T. (2019). Evaluation of a direct shear test setup to quantify AAR-induced expansion and damage in concrete. *Construction and Building Materials*, *229*, 116806. https://doi.org/10.1016/j.conbuildmat.2019.116806

Den Uijl, J. A., & Kaptijn, N. (2002). Structural consequences of ASR: An example on shear capacity. *Heron*, *47*(2), 125–139.

Deng, Q., Yi, W. J., & Tang, F. J. (2017). Effect of coarse aggregate size on shear behavior of beams without shear reinforcement. *ACI Structural Journal*, *114*(5), 1131–1142. https://doi.org/10.14359/51689720

Deschenes, D., Bayrak, O., & Folliard, K. (2009). Shear capacity of large-scale bridge bent specimens subject to alkali-silica reaction and delayed ettringite formation. In ASCE (Ed.), *Structures Congress 2009* (pp. 1049–1057).

https://doi.org/10.1061/41031(341)116

Dunbar, P. A., & Grattan-Bellew, P. E. (1995). Results of damage rating evaluation of condition of concrete from a number of structures affected by ASR. *CANMET/ACI International Workshop on Alkali–Aggregate Reactions in Concrete*, 257–266.

Dutton, M. G., Hoult, N. A., Take, W. A., & Air Force Office of Scientific, R. (2011). Towards a digital image correlation based strain sensor. *8th International Workshop on Structural Health Monitoring 2011: Condition-Based Maintenance and Intelligent Structures*, *2*, 2195–2202. https://doi.org/10.1111/jop.12119

Dutton, M., Take, W. A., & Hoult, N. A. (2014). Curvature monitoring of beams using digital image correlation. *Journal of Bridge Engineering*, *19*(3). https://doi.org/10.1061/(ASCE)BE.1943-5592.0000538

Dworakowski, Z., Kohut, P., Gallina, A., Holak, K., & Uhl, T. (2016). Vision-based algorithms for damage detection and localization in structural health monitoring. *Structural Control and Health Monitoring*, *23*(1), 35–50. https://doi.org/10.1002/stc.1755

Dzaye, E. D., Tsangouri, E., Spiessens, K., De Schutter, G., & Aggelis, D. G. (2019). Digital image correlation (DIC) on fresh cement mortar to quantify settlement and shrinkage. *Archives of Civil and Mechanical Engineering*, *19*(1), 205–214. https://doi.org/10.1016/j.acme.2018.10.003

Echegaray-Oviedo, J., & Navarro-Gregori, J. E. C. and P. S. (2013). Upgrading the Push-Off Test To Study the Mechanisms of Shear. *8th International Conference on Fracture Mechanics of Concrete and Concrete Structures*, *8*, 1012–1021. www.icitech.upv.es

Fédération Internationale du Béton (fib). (2010). *Shear and punching shear in RC and FRC elements*. International Federation for Structural Concrete (fib).

Fédération Internationale du Béton (fib). (2013). *fib Model Code for Concrete Structures 2010*. Ernst & Sohn.

Fenwick, R. C., & Paulay, T. (1968). Mechanism of Shear resistance of Concrete Beams. *Journal of the Structural Division, ASCE*, *94*(No. ST10), 2235–2350.

Fernández Ruiz, M., Muttoni, A., & Sagaseta, J. (2015). Shear strength of concrete members without transverse reinforcement: A mechanical approach to consistently account for size and strain effects. *Engineering Structures*, *99*, 360–372. https://doi.org/10.1016/j.engstruct.2015.05.007

Fujii, M., Kobayashi, K., Kojima, T., & Maehara, H. (1986). The Static and Dynamic Behavior of Reinforced Concrete Beams With Cracking Due to Alkali-Silica Reaction. *7th International Conference on Alkali-Aggregate Reaction*.

Gamache, R., & Santini-Bell, E. (2009). Non-intrusive Digital Optical Means to Develop Bridge Performance Information. *Non-Destructive Testing in Civil Engineering*, *June 2014*, 1–6. https://core.ac.uk/download/files/145/21747026.pdf

Gambarova, P. G., & Karakoc, C. (1983). New Approach To the Analysis of the Confinement Role in Regularly Cracked Concrete Elements. In *Transactions of the International Conference on Structural Mechanics in Reactor Technology*.

Gautam, B. P., Panesar, D. K., Sheikh, S. A., & Vecchio, F. J. (2017). Effect of Multiaxial Stresses on Alkali-Silica Reaction Damage of Concrete. *ACI Materials Journal*, *114*(4), 595–605. https://doi.org/10.14359/51689617

Ghannoum, W. M. (1998). *SIZE EFFECT ON SHEAR STRENGTH OF REINFORCED CONCRETE BEAMS*.

Giaccio, G., Zerbino, R., Ponce, J. M., & Batic, O. R. (2008). Mechanical behavior of concretes damaged by alkali-silica reaction. *Cement and Concrete Research*, *38*(7), 993–1004. https://doi.org/10.1016/j.cemconres.2008.02.009

Giorla, A., Dunant, C. F., Guidoum, A., & Scrivener, K. L. (2012). Experimental and numerical study of Alkali-Silica Reaction under multi-axial load. *14th International Conference on Alkali Aggregate Reaction*, *May*. https://doi.org/10.13140/2.1.4159.9360

Gorga, R. V. (2018). *Engineering-Based FE Approach to Appraise Slender Structures Affected by Alkali-Aggregate Reaction (AAR)*. https://ruor.uottawa.ca/bitstream/10393/38179/1/Vilela_Gorga_Rodrigo_2018_Thesis.pdf

Gowripalan, N., & Cao, J. (2018). Effect of Alkali Silica Reaction on Bond Strength and Load Capacity of Effect of Alkali Silica Reaction on Bond Strength and Load Capacity of Reinforced Concrete Structures. *5th International Fib Congress*, *October*, 3088–3099.

Grattan-Bellew, P. E., Cybanski, G., Fournier, B., & Mitchell, L. (2003). Proposed Universal Accelerated Test for Alkali-Aggregate Reaction The Concrete Microbar Test. *Cement, Concrete, and Aggregates*, *25*(2), 29–34.

www.astm.org

Grattan-Bellew, P. E., & Danay, A. (1992). Comparison of laboratory and field evaluation of AAR in large dams. *Proc. of the International Conference on Concrete AAR in Hydroelectric Plants and Dams*.

Hansen, S. G., & Hoang, L. C. (2019). *Influence of Alkali-Silica Reaction on the Shear Capacity of Reinforced Concrete Slabs Without Shear Reinforced*. https://portal.findresearcher.sdu.dk/en/publications/influence-of-alkali-silica-reaction-on-the-shear-capacity-of-rein

Hayes, N. W., Gui, Q., Abd-Elssamd, A., Pape, Y. Le, Giorla, A. B., Pape, S. Le, Giannini, E. R., & Ma, Z. J. (2018). Monitoring alkali-silica reaction significance in nuclear concrete structural members. *Journal of Advanced Concrete Technology*, *16*(4), 179–189. https://doi.org/10.3151/jact.16.179

Helfrick, M. N., Niezrecki, C., Avitabile, P., & Schmidt, T. (2011). 3D digital image correlation methods for full-field vibration measurement. *Mechanical Systems and Signal Processing*, *25*(3), 917–927. https://doi.org/10.1016/j.ymssp.2010.08.013

Hofbeck, J. A., Ibrahim, I. O., & Mattock, A. H. (1969). Shear Transfer in Reinforced Concrete. *ACI Journal, Proceedings*, *66*(2), 119–128. https://doi.org/10.14359/7349

Hoult, N. A., Andy Take, W., Lee, C., & Dutton, M. (2013). Experimental accuracy of two dimensional strain measurements using Digital Image Correlation. *Engineering Structures*, *46*, 718–726. https://doi.org/10.1016/j.engstruct.2012.08.018

Hoult, N. A., Dutton, M., Hoag, A., & Take, W. A. (2016). Measuring crack movement in reinforced concrete using digital image correlation: Overview and application to shear slip measurements. *Proceedings of the IEEE*, *104*(8), 1561–1574. https://doi.org/10.1109/JPROC.2016.2535157

Hsu, T. C., Mau, S. T., & Chen, B. (1987). Theory of Shear Transfer Strength in Reinforced Concrete. *ACI Structural Journal*, *84*(2), 149–160. https://doi.org/10.14359/2834

Huber, P., Huber, T., & Kollegger, J. (2016). Investigation of the shear behavior of RC beams on the basis of measured crack kinematics. *Engineering Structures*, *113*, 41–58. https://doi.org/10.1016/j.engstruct.2016.01.025

Inoue, S., Fujiii, M., Kobayashi, K., & Nakano, K. (1989). Structural behaviours of reinforced concrete beams affected by alkali-silica reaction. *8th International*

Conference on AAR in Concrete, 727–732.

IStructE. (1992). *Structural effects of alkali-silica reaction*.

J. Vecchio, F., & P. Collins, M. (1986). The Modified Compression-Field Theory for Reinforced Concrete Elements Subjected to Shear. *ACI Journal Proceedings*, *83*(2), 219–231. https://doi.org/10.14359/10416

Jin, X., Tong, J., Tian, Y., & Jin, N. (2018). Time-varying relative displacement field on the surface of concrete cover caused by reinforcement corrosion based on DIC measurement. *Construction and Building Materials*, *159*, 695–703. https://doi.org/10.1016/j.conbuildmat.2017.10.119

Journal de Montréal. (2016). *Effondrement du viaduc de la Concorde: le récit des premiers journalistes arrivés sur place*. https://www.journaldemontreal.com/2016/09/30/effondrement-du-viaduc-de-la-concorde-le-recit-des-premiers-journalistes-arrives-sur-place

Jurcut, A. (2015). *MODELLING OF ALKALI-AGGREGATE REACTION*.

Kawabata, Y., Seignol, J. F., Martin, R. P., & Toutlemonde, F. (2017). Macroscopic chemo-mechanical modeling of alkali-silica reaction of concrete under stresses. *Construction and Building Materials*, *137*, 234–245. https://doi.org/10.1016/j.conbuildmat.2017.01.090

Kobayashi, K., Inoue, S., Yamasaki, T., & Nakano, K.-I. (1988). *Alkali aggregate reaction in prestressed concrete beams*.

Kohut, P., Holak, K., Martowicz, A., & Uhl, T. (2017). Experimental assessment of rectification algorithm in vision-based deflection measurement system. *Nondestructive Testing and Evaluation*, *32*(2), 200–226. https://doi.org/10.1080/10589759.2016.1159306

Kohut, P., Holak, K., Uhl, T., Mączak, J., & Szulim, P. (2014). *Application of vision based damage detection for real civil engineering structure*. https://doi.org/10.4028/www.scientific.net/KEM.588.22

Kuchma, D. A., Wei, S., Sanders, D. H., Belarbi, A., & Novak, L. C. (2019). Development of the one-way shear design provisions of ACI 318-19 for reinforced concrete. *ACI Structural Journal*, *116*(4), 285–295. https://doi.org/10.14359/51716739

Lagier, F., Jourdain, X., De Sa, C., Benboudjema, F., & Colliat, J. B. (2011). Numerical strategies for prediction of drying cracks in heterogeneous materials: Comparison upon experimental results. *Engineering Structures*, *33*(3), 920–931. https://doi.org/10.1016/j.engstruct.2010.12.013

Lecompte, D., Smits, A., Bossuyt, S., Sol, H., Vantomme, J., Van Hemelrijck, D., & Habraken, A. M. (2006). Quality assessment of speckle patterns for digital image correlation. *Optics and Lasers in Engineering*, *44*(11), 1132–1145. https://doi.org/10.1016/j.optlaseng.2005.10.004

Lee, C., Take, W. A., & Hoult, N. A. (2012). Optimum Accuracy of Two-Dimensional Strain Measurements Using Digital Image Correlation. *Journal of Computing in Civil Engineering © ASCE*, *26*(6), 795–803. https://doi.org/10.1061/(asce)cp.1943-5487.0000182

Lee, J. J., & Shinozuka, M. (2006). A vision-based system for remote sensing of bridge displacement. *NDT and E International*, *39*(5), 425–431. https://doi.org/10.1016/j.ndteint.2005.12.003

Lee, J., & Lopez, M. M. (2014). An Experimental Study on Fracture Energy of Plain Concrete. *International Journal of Concrete Structures and Materials*, *8*(2), 129–139. https://doi.org/10.1007/s40069-014-0068-1

Li, B., Maekawa, K., & Okamura, H. (1989). Contact density model for stress transfer across cracks in concrete. *Journal of the Faculty of Eng., the University of Tokyo (B)*, *Vol. XL*(1), 9–52.

Luo, G., Chutatape, O., & Fang, H. (2001). Experimental study on nonuniformity of line jitter in CCD images. *Applied Optics*, *40*(26), 4716. https://doi.org/10.1364/ao.40.004716

Mahal, M., Blanksvärd, T., Täljsten, B., & Sas, G. (2015). *Using digital image correlation to evaluate fatigue behavior of strengthened reinforced concrete beams*. https://doi.org/10.1016/j.engstruct.2015.10.017

Martin, R. P., Bazin, C., & Toutlemonde, F. (2012). *Alkali aggregate reaction and delayed ettringite formation : common features and differences*. *September*.

Maruyama, I., & Sasano, H. (2014). Strain and crack distribution in concrete during drying. *Materials and Structures/Materiaux et Constructions*, *47*(3), 517–532. https://doi.org/10.1617/s11527-013-0076-7

Mattock, A. H., & Hawkins, N. M. (1972). Shear Transfer in Reinforced Concrete—Recent Research. *Prestressed Concrete Institute*, *17*(2), 55–75.

Mauroux, T., Benboudjema, F., Turcry, P., Aït-Mokhtar, A., & Deves, O. (2012). Study of cracking due to drying in coating mortars by digital image correlation. *Cement and Concrete Research*, *42*(7), 1014–1023.

https://doi.org/10.1016/j.cemconres.2012.04.002

Mitchell, D., Asce, M., Marchand, J., Croteau, P., & Cook, W. D. (2011). *Concorde Overpass Collapse: Structural Aspects*. https://doi.org/10.1061/(ASCE)CF.1943-5509.0000183

Miyagawa, T. (2013). Fracture of reinforcing steels in concrete damaged by ASR. *Construction and Building Materials*, *39*, 105–112. https://doi.org/10.1016/j.conbuildmat.2012.05.015

Multon, S., & Toutlemonde, F. (2006). Effect of applied stresses on alkali-silica reaction-induced expansions. *Cement and Concrete Research*, *36*, 912–920. https://doi.org/10.1016/j.cemconres.2005.11.012

Murray, C., Hoag, A., Hoult, N. A., & Take, W. A. (2014). Field monitoring of a bridge using digital image correlation. *Proceedings of the Institution of Civil Engineers - Bridge Engineering*, *168*(1), 3–12. https://doi.org/10.1680/bren.13.00024

Muttoni, A., & Fernández Ruiz, M. (2008). Shear strength of members without transverse reinforcement as function of critical shear crack width. *ACI Structural Journal*, *105*(2), 163–172.

Niezrecki, C., Baqersad, J., & Sabato, A. (2018). Digital Image Correlation Techniques for Non-Destructive Evaluation and Structural Health Monitoring. In *Handbook of Advanced Non-Destructive Evaluation* (Issue June, p. 46). Springer. https://doi.org/10.1007/978-3-319-30050-4

Noël, M., Sanchez, L., & Tawil, D. (2017). Structural implications of internal swelling reactions in concrete: review and research needs. *Magazine of Concrete Research*, *70*(20), 1052–1063. https://doi.org/10.1680/jmacr.17.00383

Nonis, C., Niezrecki, C., Yu, T.-Y., Ahmed, S., Su, C.-F., & Schmidt, T. (2013). *Structural health monitoring of bridges using digital image correlation* (T. Kundu (ed.); p. 869507). https://doi.org/10.1117/12.2009647

Pan, B., Qian, K., Xie, H., & Asundi, A. (2009). Two-dimensional digital image correlation for in-plane displacement and strain measurement: a review. *Meas. Sci. Technol*, *20*, 17. https://doi.org/10.1088/0957-0233/20/6/062001

Pan, B., Tian, L., & Song, X. (2016). Real-time, non-contact and targetless measurement of vertical deflection of bridges using off-axis digital image correlation. *NDT and E International*, *79*, 73–80. https://doi.org/10.1016/j.ndteint.2015.12.006

Pan, B., Xie, H., Wang, Z., Qian, K., & Wang, Z. (2008). Study on subset size selection in digital image correlation for speckle patterns. *Optics Express*, *16*(10), 7037. https://doi.org/10.1364/oe.16.007037

Pan, B., Yu, L., Wu, D., & Tang, L. (2013). Systematic errors in two-dimensional digital image correlation due to lens distortion. *Optics and Lasers in Engineering*, *51*(2), 140–147. https://doi.org/10.1016/j.optlaseng.2012.08.012

Paulay, T., & Loeber, P. J. (1974). Shear transfer by aggregate interlock. *ACI-Special Publication*, *42*(SP-42), 1–16.

Phares, B. M., Washer, G. A., Rolander, D. D., Graybeal, B. A., & Moore, M. (2004). Routine Highway Bridge Inspection Condition Documentation Accuracy and Reliability. *Journal of Bridge Engineering*, *9*(4), 403–413. https://doi.org/10.1061/(ASCE)1084-0702(2004)9:4(403)

Reagan, D., Sabato, A., & Niezrecki, C. (2018). Feasibility of using digital image correlation for unmanned aerial vehicle structural health monitoring of bridges. *Structural Health Monitoring*, *17*(5), 1056–1072. https://doi.org/10.1177/1475921717735326

Reinhardt, H.-W., & Walraven, J. C. (1982). Cracks in Concrete Subject to shear. *Journal of the Structural Division*, *108*(ST1), 225–244.

Sabato, A., Beale, C. H., & Niezrecki, C. (2017). *A novel optical investigation technique for railroad track inspection and assessment* (H. F. Wu, A. L. Gyekenyesi, P. J. Shull, & T.-Y. Yu (eds.); p. 101692C). https://doi.org/10.1117/12.2257831

Sanchez, L. F.M., Fournier, B., Jolin, M., & Bastien, J. (2015). Evaluation of the Stiffness Damage Test (SDT) as a tool for assessing damage in concrete due to alkali-silica reaction (ASR): Input parameters and variability of the test responses. *Construction and Building Materials*, *77*, 20–32. https://doi.org/10.1016/j.conbuildmat.2014.11.071

Sanchez, L. F.M., Fournier, B., Jolin, M., & Duchesne, J. (2015). Reliable quantification of AAR damage through assessment of the Damage Rating Index (DRI). *Cement and Concrete Research*, *67*, 74–92. https://doi.org/10.1016/j.cemconres.2014.08.002

Sanchez, L. F.M., Fournier, B., Jolin, M., Mitchell, D., & Bastien, J. (2017). Overall assessment of Alkali-Aggregate Reaction (AAR) in concretes presenting different strengths and incorporating a wide range of reactive aggregate types and natures. *Cement and Concrete Research*, *93*, 17–31.

https://doi.org/10.1016/j.cemconres.2016.12.001

Sanchez, L., Fournier, B., Bastien, J., & Mitchell, D. (2016). *Assessment of Structures Subject to Concrete Degradation*.

Sanchez, Leandro F.M. (2014). *Contribution to the assessment of damage in aging concrete infrastructures affected by alkali-aggregate reaction*. 341.

Santini-Bell, E., Brogan, P. A., Lefebvre, P. J., Peddle, J., Brenner, B., & Sanyei, M. (n.d.). *Digital Image Correlation Application to Structural Health Monitoring*. Retrieved December 15, 2019, from https://pdfs.semanticscholar.org/6f68/accacf7ff1f50ed7e23ae5aa0e69642a3bf1.pdf

Scrivener, K. L., Crumbie, A. K., & Laugesen, P. (2004). The interfacial transition zone (ITZ) between cement paste and aggregate in concrete. *Interface Science*, *12*(4), 411–421. https://doi.org/10.1023/B:INTS.0000042339.92990.4c

Shah, S. G., & Kishen, J. M. C. (2011). Fracture Properties of Concrete-Concrete Interfaces Using Digital Image Correlation. *Experimental Mechanics*, *51*(3), 303–313. https://doi.org/10.1007/s11340-010-9358-y

Sherwood, E. G. (2008). *One-Way Shear Behaviour of Large, Lightly-Reinforced Concrete Beams and Slabs*.

Sherwood, E. G., Bentz, E. C., & Collins, M. P. (2007). Effect of aggregate size on beam-shear strength of thick slabs. *ACI Structural Journal*, *104*(2), 180–190. https://doi.org/10.14359/18530

Smaoui, N. (2003). *Contribution à l'évaluation du comportement structural des ouvrages d'art affectés de réaction alcalis-silice (ras)*.

Soetens, T., & Matthys, S. (2017). Shear-stress transfer across a crack in steel fibre-reinforced concrete. *Cement and Concrete Composites*, *82*, 1–13. https://doi.org/10.1016/j.cemconcomp.2017.05.010

Sutton, M. A., Orteu, J.-J., & Schreier, H. W. (2009). *Image Correlation for Shape, Motion and Deformation Measurements*. https://doi.org/10.1007/978-0-387-78747-3

Sutton, M., Wolters, W., Peters, W., Ranson, W., & McNeill, S. (1983). Determination of displacements using an improved digital correlation method. *Image and Vision Computing*, *1*(3), 133–139. https://doi.org/10.1016/0262-8856(83)90064-1

Swamy, R. N. (1990). Alkali-silica reaction and concrete structures. *Structural*

Engineering Review, *2*, 89–103.

Swamy, R. N. (1995). Effects of alkali-aggregate reactivity on material stability and structural integrity. *CANMET/ACI International Workshop on Alkali-Aggregate Reactions in Concrete*, 293–310.

Swamy, R. N., & Al-Asali, M. M. (1989). Effect of alkali-silica reaction on the structural behavior of reinforced concrete beams. *ACI Structural Journal*, *86*(4), 451–459. https://doi.org/10.14359/2961

Taylor, H. (1970). Investigation of forces carried across cracks in reinforcedconcrete beams by interlock of aggregates. *Cement and Concrete Research*, 22.

Teramoto, A., Watanabe, M., Murakami, R., & Ohkubo, T. (2018). Visualization of internal crack growth due to alkali-silica reaction using digital image correlation. *Construction and Building Materials*, *190*(11), 851–860. https://doi.org/10.1016/j.conbuildmat.2018.09.168

Thomas, M. D. A., Folliard, K. J., Fournier, B., Rivard, P., & Drimalas, T. (2013). *Methods for Evaluating and Treating ASR-Affected Structures: Results of Field Application and Demonstration Projects Volume I: Summary of Findings and Recommendations Final Report*.

Thomas, M. D. A., Fournier, B., Folliard, K. J., & Resendez, Y. . (2011). *ALKALI-SILICA REACTIVITY FIELD IDENTIFICATION HANDBOOK*.

Transport Canada. (2013). *Part E - Bridge Inspection*. https://www.tc.gc.ca/eng/railsafety/guideline-732.htm

Uhl, T., Kohut, P., Holak, K., & Krupiński, K. (2011). Vision based condition assessment of structures. *J. Phys.: Conf. Ser*, *305*, 1–10. https://doi.org/10.1088/1742-6596/305/1/012043

US Departement of Transportation. (2012). Alkali-Aggregate Reactivity (Aar) Workshops for Engineers and Practitioners. In *Reference Manual*. https://doi.org/10.1093/jnci/djs534

Wald, D. M., Allford, M. T., Bayrak, O., & Hrynyk, T. D. (2017). Development and multiaxial distribution of expansions in reinforced concrete elements affected by alkali–silica reaction. *Structural Concrete*, *18*(6), 914–928. https://doi.org/10.1002/suco.201600220

Walraven, J. C. (n.d.). Fundamental Analysis of Aggregate Interlock. *Journal of the Structural Division*, *107*(ST11), 2245–2271.

Walraven, J. C. (1980). *Aggregate Interlock: A theoretical and experimental analysis*. Delft University.

Walraven, J. C., & Reinhardt, H. W. (1981). Theory and Experiments on the Mechanical Behaviour of Cracks in Plain and Reinforced Concrete Subjected to Shear Loading. *Heron*, *26*(1A), 1–68.

Wang, J. J., Gowripalan, N., Li, J., & Nguyen, V. V. (2017). Close-range photogrammetry for accurate deformation distribution measurement. In *Mechanics of Structures and Materials: Advancements and Challenges - Proceedings of the 24th Australasian Conference on the Mechanics of Structures and Materials, ACMSM24 2016* (pp. 793–799).

Wight, J. k. (2016). Shear Friction, Horizontal Shear Trasnfer, and Composite Concrete Beams. In *Reinforced Concrete Mechanics and Design* (7th ed., pp. 852–872). Pearson Education.

Xiao, J., Xie, H., & Yang, Z. (2012). Shear transfer across a crack in recycled aggregate concrete. *Cement and Concrete Research*, *42*(5), 700–709. https://doi.org/10.1016/j.cemconres.2012.02.006

Yoneyama, Satoru, & Ueda, H. (2011). *Bridge Deflection Measurement Using Digital Image Correlation with Camera Movement Correction*. https://doi.org/10.2320/matertrans.I-M2011843

Yoneyama, Saturu, Kikuta, H., Kitagawa, A., & Kitamura, K. (2006). Lens distortion correction for digital image correlation by measuring rigid body displacement. *Optical Engineering*, *45*(2). https://doi.org/10.1117/1.2168411

Zarate Garnica, G. (2018). *Analysis of shear transfer mechanisms in concrete members without shear reinforcement based on kinematic measurements*. https://repository.tudelft.nl/islandora/object/uuid%3A9b40b743-73b3-4698-9e9b-c6ac05f5f99c

Zhang, D. S., Luo, M., & Arola, D. D. (2006). Displacement/strain measurements using an optical microscope and digital image correlation. *Optical Engineering*, *45*(3). https://doi.org/10.1117/1.2182108

Zhao, P., Zsaki, A. M., & Nokken, M. R. (2018). Using digital image correlation to evaluate plastic shrinkage cracking in cement-based materials. *Construction and Building Materials*, *182*, 108–117. https://doi.org/10.1016/j.conbuildmat.2018.05.239